Atmos. Chem. Phys. Discuss., 14, 14725–14832, 2014
www.atmos-chem-phys-discuss.net/14/14725/2014/
doi:10.5194/acpd-14-14725-2014

Atmospheric Chemistry and Physics Discussions

Detailed source term estimation of the atmospheric release for the Fukushima Daiichi Nuclear Power Station accident by coupling simulations of atmospheric dispersion model with improved deposition scheme and oceanic dispersion model

G. Katata[1], M. Chino[1], T. Kobayashi[1], H. Terada[1], M. Ota[1], H. Nagai[1], M. Kajino[2], R. Draxler[3], M. C. Hort[4], A. Malo[5], T. Torii[6], and Y. Sanada[7]

[1]Japan Atomic Energy Agency (JAEA), Tokai, Naka, Ibaraki, 319-1195, Japan
[2]Meteorological Research Institute, Japan Meteorological Agency (JMA), Tsukuba, Ibaraki, 305-0052, Japan
[3]Air Resources Laboratory, National Oceanic and Atmospheric Administration (NOAA), University Research Court College Park, Maryland, 20740, USA

[4]Met Office, Exeter, Devon, EX1 3PB, UK
[5]Canadian Meteorological Centre (CMC), Dorval, Quebec, H9P 1J3, Canada
[6]JAEA, Chiyoda, Tokyo, 100-8577, Japan
[7]JAEA, Fukushima, Fukushima, 960-1296, Japan

Received: 25 April 2014 – Accepted: 16 May 2014 – Published: 5 June 2014

Correspondence to: G. Katata (katata.genki@jaea.go.jp)

Published by Copernicus Publications on behalf of the European Geosciences Union.

Discussion Paper | Discussion Paper | Discussion Paper | Discussion Paper |

Abstract

Temporal variations in the amount of radionuclides released into the atmosphere during the Fukushima Dai-ichi Nuclear Power Station (FNPS1) accident and their atmospheric and marine dispersion are essential to evaluate the environmental impacts and resultant radiological doses to the public. In this paper, we estimate a detailed time trend of atmospheric releases during the accident by combining environmental monitoring data with atmospheric model simulations from WSPEEDI-II (Worldwide version of System for Prediction of Environmental Emergency Dose Information), and simulations from the oceanic dispersion model SEA-GEARN-FDM, both developed by the authors. A sophisticated deposition scheme, which deals with dry and fogwater depositions, cloud condensation nuclei (CCN) activation and subsequent wet scavenging due to mixed-phase cloud microphysics (in-cloud scavenging) for radioactive iodine gas (I_2 and CH_3I) and other particles (CsI, Cs, and Te), was incorporated into WSPEEDI-II to improve the surface deposition calculations. The fallout to the ocean surface calculated by WSPEEDI-II was used as input data for the SEA-GEARN-FDM calculations. Reverse and inverse source-term estimation methods based on coupling the simulations from both models was adopted using air dose rates and concentrations, and sea surface concentrations. The results revealed that the major releases of radionuclides due to FNPS1 accident occurred in the following periods during March 2011: the afternoon of 12 March due to the wet venting and hydrogen explosion at Unit 1, the morning of 13 March after the venting event at Unit 3, midnight of 14 March when the SRV (Safely Relief Valve) at Unit 2 was opened three times, the morning and night of 15 March, and the morning of 16 March. According to the simulation results, the highest radioactive contamination areas around FNPS1 were created from 15 to 16 March by complicated interactions among rainfall, plume movements, and the temporal variation of release rates associated with reactor pressure changes in Units 2 and 3. The modified WSPEEDI-II simulation using the new source term reproduced local and regional patterns of cumulative surface deposition of total ^{131}I and ^{137}Cs and air dose

rate obtained by airborne surveys. The new source term was also tested using three atmospheric dispersion models (MLDP0, HYSPLIT, and NAME) for regional and global calculations and showed good agreement between calculated and observed air concentration and surface deposition of ^{137}Cs in East Japan. Moreover, HYSPLIT model using the new source term also reproduced the plume arrivals at several countries abroad showing a good correlation with measured air concentration data. A large part of deposition pattern of total ^{131}I and ^{137}Cs in East Japan was explained by in-cloud particulate scavenging. However, for the regional scale contaminated areas, there were large uncertainties due to the overestimation of rainfall amounts and the underestimation of fogwater and drizzle depositions. The computations showed that approximately 27 % of ^{137}Cs discharged from FNPS1 deposited to the land in East Japan, mostly in forest areas.

1 Introduction

A significant amount of radioactive material was accidentally emitted into the atmosphere from the Fukushima Daiichi Nuclear Power Station (hereafter referred to as FNPS1) due to catastrophic earthquake and tsunami on 11 March 2011. This caused radiological contamination not only around FNPS1 but over a wide region of Japan (NRA, 2012a). To assess the magnitude of the accident and radiological doses, an accurate estimation of the source term of radionuclides discharged into the atmosphere is required.

After the accident, the source term of total ^{131}I, which includes all the chemical forms of ^{131}I (hereinafter ^{131}I) and ^{137}Cs was estimated by authors from the Japan Atomic Energy Agency (JAEA) using a reverse estimation method (UNSCEAR, 2014). This method calculates the release rates of radionuclides ($Bq\,h^{-1}$) by coupling the atmospheric dispersion simulation made with a unit release rate ($1\,Bq\,h^{-1}$) with environmental monitoring data. The ratio of the monitoring data to the dispersion calculation provides an estimate of the source term. Chino et al. (2011) carried out the first es-

timation of the source term of ^{131}I and ^{137}Cs from 12 March to 4 April 2011. Katata et al. (2012a) estimated detailed source term for 15 March 2011 when the highest radiological polluted area was created. Katata et al. (2012b) revised the source term of Chino et al. (2011) for the early phases (12 to 14 March 2011) of the accident. Terada et al. (2012) slightly refined the source term of Chino et al. (2011) after 16 March and extended it to 1 May 2011 (hereinafter referred as the JAEA source term). They also showed the regional and local atmospheric dispersion patterns of the radionuclides for March 2011.

The JAEA source term has been validated using atmospheric dispersion simulation results compared with the environmental data which were not used for the source term estimation (e.g., daily fallout and surface deposition) and by comparison with other source terms created using different approaches and datasets. Terada et al. (2012) showed that WSPEEDI-II could reproduce most of observed daily fallout in Eastern Japan from 20 to 31 March within a factor 10 using the JAEA source term. Later on, Morino et al. (2013) carried out atmospheric dispersion simulations using several source terms and found that when the JAEA source term was used, the surface deposition pattern of ^{137}Cs in Eastern Japan was reproduced with higher accuracy than any of the other source terms. Draxler et al. (2014) showed that five different atmospheric dispersion and meteorological models overall reproduced regional patterns in observed ^{137}Cs deposition and air concentration of ^{131}I and ^{137}Cs when using the JAEA source term. Meanwhile, Hirao et al. (2013) also estimated the source term using an inverse estimation method (UNSCEAR, 2014) by coupling their atmospheric dispersion model with the data of air concentration and daily fallout in Eastern Japan. Their result agreed with the JAEA source term for many of the large emission events despite using different sets of monitoring data, further supporting the reliability of the JAEA source term. Saunier et al. (2013) and Winiarek et al. (2014) also estimated the source term for the major releases of 14 and 15 March 2011 by inverse modeling techniques using the data of air dose rate, daily fallout, and the airborne survey of ^{137}Cs surface deposition

in Eastern Japan. Their results were comparable to the JAEA source term for those periods.

While the JAEA source term has been supported by the many studies summarized above, three major improvements are required to determine a more precise source term. First, the estimation of the major releases of 15 March 2011, which seems to have created the largest polluted areas to the northwest of the plant, is still uncertain in terms of prediction accuracy for the ^{137}Cs deposition pattern. Using the JAEA source term, Katata et al. (2012a) found that the formation process of high dose areas in the Fukushima Prefecture can be explained by wet deposition of the high-concentration plume released in the morning and afternoon on 15 March. However, the later studies of WSPEEDI-II (Terada et al., 2012) and other dispersion simulations (Draxler et al., 2014) reported the underestimation and overestimation of the surface deposition of ^{137}Cs in the areas in Tochigi and Gunma Prefectures, and in the north part of Fukushima Prefecture and Miyagi Prefecture, respectively. However, the modeling study of Morino et al. (2013) calculated a surface deposition amount that nearly corresponded to the observational data. This discrepancy can be caused by the uncertainty of source term estimation, but also the uncertainties in the deposition schemes of the atmospheric dispersion models. Constant values for the dry deposition velocities and a simple exponential function of precipitation intensity for the wet scavenging coefficients are widely used in the deposition schemes of atmospheric dispersion models, including WSPEEDI-II (Table 1).

From their sensitivity studies, Morino et al. (2013) showed the prediction accuracy of the surface deposition pattern of ^{137}Cs in Eastern Japan strongly depended on the wet scavenging coefficient. Wet scavenging of aerosols may be separated to two distinct processes: the nucleation (in-cloud) scavenging and aerosol–hydrometeor coagulation (below-cloud) scavenging (e.g., Tost et al., 2006). In the initial phase of hydrometeor formation, aerosols are scavenged due to the cloud condensation nuclei (CCN) activation forming cloud droplets. The latter process, the aerosol–hydrometeor coagulation scavenging, is drastically different between liquid precipitation and frozen precipitation

primarily due to difference in collection efficiency of aerosols (e.g., Miller, 1990). For gases, the wet scavenging process is the result of the dissolution or deposition to hydrometeors in both in-cloud and below-cloud regimes. Dry deposition is also important particularly for the reverse estimation method using dust sampling data, because the atmospheric concentration near the surface is affected by removal through dry deposition. Both deposition processes strongly depend on physicochemical characteristics of the radionuclides (gas or particle, hygroscopic or non-hygroscopic, and the existing size range for particles) in the atmosphere. Furthermore, the potential impact of fogwater (or low cloud) deposition of radionuclides in the mountain areas of Tochigi and Gunma Prefectures are suggested for certain days of the FNPS1 accident when easterly winds prevailed (Terada et al., 2012; Kaneyasu et al., 2012). Fogwater deposition is completely missing in any of the current atmospheric dispersion models. To improve the accuracy of the JAEA source term, it is necessary to modify WSPEEDI-II by including more sophisticated deposition processes.

Second, the JAEA source term was computed using environmental monitoring data collected over the land areas of Eastern Japan, but when plumes flowed directly toward Pacific Ocean, the release rates were simply interpolated between the estimated values during on-shore flow. The first results of the source term estimation using both atmospheric and oceanic dispersion models by Kobayashi et al. (2013) revealed that the JAEA source term underestimated the seawater surface concentration of ^{134}Cs in Pacific Ocean. However, their atmospheric dispersion simulation using a modified source term overestimated deposition amounts over the land because their correction was applied for both off-shore and on-shore flow cases. The overestimation of the deposition amount over the land areas of Japan has also been reported by Morino et al. (2013) when using the source term estimated by global simulations with the air concentration data sampled at the Comprehensive Nuclear-Test-Ban Treaty Organization (CTBTO) stations (Stohl et al., 2012). The surface deposition of ^{137}Cs was also clearly overestimated in regional calculations. Thus, only the release rates of the plumes which directly flowed toward the ocean should be re-computed using the coupled simulation of the

atmospheric and oceanic dispersion models. For other cases the source term can be estimated using only the environmental data collected over the land.

Finally, in the JAEA source term, the release rates in the early phase of the accident have been estimated primarily using the air dose rate data far away from the FNPS1 due to lack of routine operating equipment (e.g., stack monitors, radiation and meteorological stations) within 20 km from the station (Katata et al., 2012a, b). Three years after the accident, additional environmental monitoring data from 12 to 31 March 2011 have become available including the air dose rates measured within 20 km from FNPS1 (Fukushima Prefecture, 2012), a detailed ^{131}I deposition map around the station (Torii et al., 2013), and dust sampling (US DOE, 2011; NRA, 2012b). This enables us to make a more detailed estimation of the atmospheric releases during the accident using the reverse estimation method by combining the modified WSPEEDI-II results with these additional monitoring data.

Thus, the present study aims to determine the detailed source term of ^{131}I and ^{137}Cs during the FNPS1 accident using WSPEEDI-II (Sects. 2.1) with a modified deposition scheme (Appendix A) combining the above new data and an offline coupling of the atmospheric and oceanic dispersion models (Sects. 2.2 and 2.3). The observational data and simulation conditions are described in Sect. 2.4. The estimation result of the source term and reconstructed atmospheric dispersion process are presented in Sect. 3.1. The estimated source term is as tested by comparing the simulation results using modified WSPEEDI-II with airborne monitoring data of air dose rate and surface deposition of ^{131}I and ^{137}Cs in Eastern Japan (Sect. 3.2.1). Moreover, the source term is independently evaluated based on the simulations of different atmospheric dispersion models by demonstrating model-observation comparisons in atmospheric concentration and surface deposition over regional and global scales (Sect. 3.2.2). Finally, the difference between the new source term and those from prior studies and the role of deposition processes during the FNPS1 accident are discussed based on the simulation results (Sects. 4.1 and 4.2, respectively).

2 Material and methods

2.1 Models

The emergency response system's atmospheric dispersion model (WSPEEDI-II) and an oceanic dispersion model (SEA-GEARN-FDM) are used to estimate the source term. WSPEEDI-II combines two models: a non-hydrostatic atmospheric dynamic model (MM5, Grell et al., 1994) and a Lagrangian particle dispersion model (GEARN, Terada and Chino, 2008). MM5 predicts three-dimensional fields of wind, precipitation, diffusion coefficients, etc. based upon the atmospheric dynamic equations at an appropriate spatial and temporal resolution, by using nested domains. GEARN calculates the advection and diffusion of radioactive plumes, dry and wet deposition onto the ground surface, and air dose rate from radionuclides in the air and on the ground surface (ground-shine). GEARN can predict the atmospheric dispersion on both local and regional domains simultaneously by considering in- and out-flow between the domains. The areas of two GEARN domains are the same as the MM5 nested domains. The performance of this system was evaluated by its application to the field tracer experiment over Europe, ETEX (Furuno et al., 2004), the Chernobyl accident (Terada et al., 2004; Terada and Chino, 2005, 2008), and the FNPS1 accident (Katata et al., 2012a, b; Terada et al., 2012). A detailed description of the models is provided in Terada et al. (2004) and Terada and Chino (2005).

In the present study, the deposition scheme of WSPEEDI-II is modified to improve the atmospheric dispersion simulation and hence the resulting accuracy of the source term estimation. The scheme consists of parameterizations for dry deposition, wet deposition (in-cloud scavenging; CCN activation and scavenging in mixed phase clouds), and fogwater deposition of gaseous and particulate radionuclides based on existing modeling approaches. Details in the scheme are described in Appendix A.

SEA-GEARN-FDM is a finite difference model used to simulate radionuclide transport in ocean (Kawamura et al., 2014). The model calculates the time trend of sea surface concentration of ^{134}Cs (half-life = 2.1 years). Horizontal turbulent mixing is modeled using the Smagorinsky formula (Smagorinsky, 1963). For vertical mixing fluxes, an empirical value of eddy diffusivity in the mixing layer ($4.0 \times 10^{-3}\,m^2\,s^{-1}$) is adopted at all model grid points throughout the simulation period. SEA-GEARN-FDM uses the 10 day mean ocean current fields from the ocean–atmosphere global model K7 (Sugiura et al., 2008). The K7 model is a fully coupled global General Circulation Model (GCM) developed by the Data Research Center for Marine–Earth Sciences, Japan Agency for Marine–Earth Science and Technology (JAMSTEC/DrC). The coupled GCM is composed of the Atmospheric GCM for the Earth Simulator (AFES; Ohfuchi et al., 2004) and the Ocean–Sea Ice GCM for the Earth Simulator (OIFES; Masuda et al., 2006). The AFES and OIFES have horizontal grid resolutions of T42 (approximately $2.8^\circ \times 2.8^\circ$) and $1^\circ \times 1^\circ$ with 24 and 45 vertical layers in σ coordinates, respectively. The four-dimensional variation method is used to execute reanalysis data in K7.

2.2 Reverse estimation method over the land

Figure 1 depicts the flowchart of the source term estimation based upon coupling the simulations of the atmospheric and oceanic dispersion models. First, the release rates of the plumes discharged from FNPS1 are estimated by combining the atmospheric dispersion calculation and the data of air dose rates and concentration of radionuclides measured over the land areas of East Japan (reverse estimation method). In the case when the plume directly flowed toward the Pacific Ocean, the release rates are initially determined by temporally interpolating two available values. Then, only the interpolated values are revised by coupling a combination of models of atmospheric and oceanic dispersion and sea surface concentration at the Pacific Ocean (inverse estimation method; Sect. 2.3).

The release rates of individual radionuclides are estimated by the reverse estimation method following our previous work (Chino et al., 2011; Katata et al., 2012a, b), i.e., coupling environmental monitoring data with atmospheric dispersion simulations, assuming a unit release rate ($1\,Bq\,h^{-1}$). Release rates are obtained as the ratio of measured to calculated air concentrations of nuclide i at the sampling points, as follows:

$$Q_i = M_i / C_i, \quad (1)$$

where Q_i is the release rate (Bq h^{-1}) of i when discharged into the atmosphere, M_i the measured air concentration (Bq m^{-3}) of i, and C_i the dilution factor (h m^{-3}) of i, which is equal to the air concentration calculated under the assumption of a unit release rate. This method of using specific radionuclide air concentration data is more reliable than the dose methods described below because it does not require an assumption of the composition of the radionuclides contributing to the dose.

Depending on the number of available data, we estimated release rates using Eq. (1) as follows: first, if the data show a continuous time series at one location (mainly offsite stations), peak values from both the measurement and calculation were used in Eq. (1). Second, if significant concentration values were simultaneously observed at more than two sites, release rates were determined by averaging the model and measured values at all sites. The use of peak values and averaging reduced the impact of discrepancies in arrival time and plume location.

When air concentration data were not available, the release rates were estimated by comparing the observed spatial patterns and/or temporal changes of air dose rates from radionuclides on the ground surface (i.e., ground-shine) with the calculated values. This method was applied to estimate the release rate in the afternoon of 12 March after the venting and hydrogen explosion at Unit 1 and in the morning of 15 March to the afternoon of 16 March. First, the temporal changes of the observed air dose rate from ground-shine are computed by WSPEEDI-II by assuming a unit release rate. Then, the release rate (Bq h^{-1}) is computed from the ratio of the measured to calculated air dose rate values. This method assumes the fractional composition of the major radionuclides contributing ground-shine, e.g., ^{131}I, ^{132}I (^{132}Te), ^{134}Cs and ^{137}Cs. Katata et al. (2012b) has noted that this assumption is a major cause of uncertainty of the source term. To minimize the errors from this assumption, we determined the radioactive composition based on various datasets over East Japan: METI (METI, 2011a), FNPS1, FNPS2 (TEPCO, 2011a), MEXT (NRA, 2011b), MEXTsea (NRA, 2011b), DOE

(US DOE, 2011), JAEA-Tokai (Ohkura et al., 2012; Furuta et al., 2011), KEK (KEK, 2011), RIKEN (Haba et al., 2012), JCAC (Amano et al., 2012), and Tokyo Metropolitan Government (Tokyo Metropolitan Government, 2011). Figure 2 depicts the temporal changes of air concentrations and radioactive ratios for all dust sampling data. In Fig. 2a and b, the curves of the radioactive ratio (R_i) of radionuclide i to ^{131}I or ^{137}Cs calculated by the following equation:

$$R_i = \frac{I_i \exp(-\lambda_i t)}{I_{\text{total } ^{131}\text{I or } ^{137}\text{Cs}} \exp(-\lambda_{\text{total } ^{131}\text{I or } ^{137}\text{Cs}} t)}, \quad (2)$$

where I is the total inventory of Unit 1 to 3 (Table 2), λ is the decay constant, and t is the period from the shutdown time of the station. As shown in Fig. 2b, the radioactive ratio of ^{132}Te to ^{137}Cs exponentially decreased from approximately 20 on 12 March. On the basis of the measurements from the quality assured offsite monitoring stations, the ratios of ^{132}Te to ^{137}Cs were set to 20 on 12 March and 10 on 15–16 March. Although the ratio of ^{137}Cs to ^{131}I can be determined from the data for most of the simulation periods (Fig. 2c), no dust data is observed from the morning on 15 March to the morning on 16 March. Therefore, the ratio in this period was set to reproduce the measured deposition maps of ^{131}I and ^{137}Cs from the atmospheric dispersion simulations. ^{132}I (half-life = 2.3 h) was treated as ^{132}Te progeny nuclide and assumed to be radioactive equilibrium with ^{132}Te (half-life = 3.2 d). The concentration of ^{134}Cs was given to be equal to that of ^{137}Cs based on the same datasets (Katata et al., 2012a). It is noted that ^{133}I was neglected in the air dose rate calculations because of its relatively low radioactivity compared to the total air dose rates.

2.3 Inverse estimation method over the ocean

The inverse estimation method calculates the release rates of the radionuclides by coupling ocean monitoring data with atmospheric and oceanic dispersion simulations. This is applied to only the periods when the plume flowed toward the ocean, while our previous work using the oceanic monitoring data estimated the release rates throughout

the simulation period (Kobayashi et al., 2013). Two sets of off-line coupling simulations of WSPEEDI-II and SEA-GEARN-FDM are carried out: one simply uses the source term estimated by the reverse estimation method (hereinafter "New-land" source term) throughout the calculation period, and the other uses the release rates for each time segment separating the New-land source term into an arbitrary number of segments. From the first simulation, the comprehensive correction index of the New-land source term at the sampling point j (Ci_j) can be calculated as follows:

$$\mathrm{Ci}_j = \mathrm{Mo}_j / \mathrm{Co}_j, \tag{3}$$

where Mo_j and Co_j are the measurements and SEA-GEARN-FDM calculations of sea surface concentration of ^{134}Cs ($\mathrm{Bq\,L^{-1}}$) at the sampling point j over the Pacific Ocean, respectively. Note that the only the observational points that are not affected by the direct release of ^{134}Cs from FNPS1 to the ocean are used for the source term estimation. The input data of daily cumulative deposition of ^{134}Cs to SEA-GEARN-FDM are obtained from WSPEEDI-II calculations using the New-land source term.

From the second simulation, the sea surface concentration $\mathrm{Cos}_{j,k}$ ($\mathrm{Bq\,L^{-1}}$) of ^{134}Cs at the sampling point of j that originated from the discharge of time segment k can be calculated using SEA-GEARN-FDM in a manner similar to the first simulation. If the total number of time segments is represented as nt, the contribution ratio of k at the sampling point of j, $\mathrm{Cn}_{j,k}$, can be defined as the ratio of calculated sea surface concentration for the time segment of k to that for the whole simulation period, expressed as:

$$\mathrm{Cn}_{j,k} = \frac{\mathrm{Cos}_{j,k}}{\sum_{k=1}^{\mathrm{nt}} \mathrm{Cos}_{j,k}} = \frac{\mathrm{Cos}_{j,k}}{\mathrm{Co}_j}. \tag{4}$$

Here, a large value of $\mathrm{Cn}_{j,k}$ indicates a large contribution of the release for the time segment k to the concentration at the sampling point j accumulated for whole simulation period, i.e., Co_j in Eq. (3). The correction index Ci_k of the New-land source term

for k is expressed by weighting the contribution ratio $\mathrm{Cn}_{j,k}$ at sampling point of j:

$$\log_{10}\mathrm{Ci}_k \cdot \sum_{j=1}^{\mathrm{np}} \mathrm{Cn}_{j,k} = \sum_{j=1}^{\mathrm{np}} (\mathrm{Cn}_{j,k} \cdot \log_{10}\mathrm{Ci}_j),$$

and thus,

$$\mathrm{Ci}_k = 10^{\sum_{j=1}^{\mathrm{np}} (\mathrm{Cn}_{j,k} \cdot \log_{10}\mathrm{Ci}_j) / \sum_{j=1}^{\mathrm{np}} \mathrm{Cn}_{j,k}}, \tag{5}$$

where np is the total number of sampling points (46 in this study). By using Eq. (5), the new release rate of ^{134}Cs for the segment k, $\mathrm{Qo}_{\mathrm{Cs\text{-}134},k}$ ($\mathrm{Bq\,h^{-1}}$), is finally obtained by multiplying the release rate of ^{134}Cs for the same time segment in the New-land source term, $Q_{\mathrm{Cs\text{-}134},k}$, with the correction index, Ci_k:

$$\mathrm{Qo}_{\mathrm{Cs\text{-}134},k} = Q_{\mathrm{Cs\text{-}134},k} \mathrm{Ci}_k. \tag{6}$$

For other radionuclides, release rates are calculated by multiplying $\mathrm{Qo}_{\mathrm{Cs\text{-}134},k}$ with the time interpolated composition ratio of each nuclide to ^{134}Cs for the New-land source term.

2.4 Observational data and simulation settings

2.4.1 Observational data for reverse estimation method over the land

For the reverse estimation method over the land (Sect. 2.2), the datasets of air dose rate and dust sampling that were used are summarized in Table 3. The location maps of sampling points are illustrated in Fig. 3. For the period of 12 March and 15–16 March 2011, the release rates were estimated primarily using air dose rates from radionuclides deposited on the ground (ground-shine) observed by portable monitors (Fukushima Prefecture, 2011a, b; Ibaraki Prefecture, 2011; Tochigi Prefecture, 2011; TEPCO, 2011a) and at automatic monitoring posts (Fukushima Prefecture, 2012) located at 22–81 km and 4–21 km downwind from FNPS1, respectively. For other periods, we used the ^{131}I and ^{137}Cs dust sampling data in Fukushima Prefecture (TEPCO,

2011a; NRA, 2011, 2012b; US DOE, 2012) and Ibaraki Prefecture (Ohkura et al., 2012) (Fig. 2).

For the estimation of the source term during 15–16 March, we needed to determine the "net" increase of ground-shine due to the deposition of the objective plume, because the monitored air dose rates contained the effects of the deposition of multiple plumes (i.e., the objective plume plus the past plume). The net increase was then estimated by subtracting the effects of the past plumes from the ground-shine after the passage of the objective plume.

2.4.2 Observational data for inverse estimation method over the ocean

For the inverse estimation method over the ocean (Sect. 2.3), we used two datasets of sea water concentration of ^{134}Cs sampled from 14 April to 3 May 2011 at the northwestern north Pacific region (450–2000 km from FNPS1, Honda et al., 2012) and from 2 April to 17 May 2011 over a much larger north Pacific region (300–8400 km from FNPS1, Aoyama et al., 2012), respectively. Figure 4a and b depicts the location of all sampling points over the Pacific Ocean. From the results of a preliminary modeling study, the sampling points where the direct release to the ocean from the FNPS1 may have had an influence were not considered in the inverse estimation (crosses in the figures).

2.4.3 Observational data for verification of source term

For model verification of the source term, we used the cumulative surface deposition of ^{137}Cs over East Japan measured by the aerial radiological survey of 31 May 2012 (NRA, 2012a). The observed surface deposition map of ^{131}I near the plant on 1 April 2011 reconstructed by Torii et al. (2013) was also compared with the calculated one. For the evaluation of the release rates during the early stages of FNPS1 accident, we used the aerial survey of total air dose rate on 17–19 March 2011 (US DOE/NNSA, 2011). Furthermore, to analyze the plume movement over the Pacific Ocean, the time

series of daily mean surface concentration data of particulate ^{131}I and ^{137}Cs at the CTBTO stations (CTBTO, 2011) and spatial maps of surface concentration of ^{137}Cs for the largest calculation domain of the WSPEEDI simulation are illustrated in Figs. 5 and 6, respectively. In the atmospheric dispersion analysis, we mainly focus on time trends in air concentration sampled at four United States stations: Sacramento California, Melbourne Florida, Sand Point Alaska, and Oahu Hawaii (Fig. 4a), where the plume was detected in the early stages of the accident (Fig. 5).

2.4.4 Simulation settings

The study area covers regional and semi-hemispheric areas around FNPS1 (Fig. 4). The simulation conditions of WSPEEDI-II are summarized in Table 4. Two sets of meteorological input data, a Grid Point Value (GPV) of the Global Spectral Model for Japan region (GSM) and the Meso-Scale Model (MSM) provided by the Japan Meteorological Agency (JMA) were examined for each release case to find out which data are the most appropriate to reconstruct the air concentration and/or air dose rates observed in the environment. A four-dimensional data assimilation method was also employed in this work using the GPV data, observed wind data at FNPS1 and FNPS2 (METI, 2011b), and surface weather stations to improve the prediction accuracy of the meteorological fields around FNPS1. While most of settings were similar to Katata et al. (2012b), the revised approach used the more sophisticated Reisner graupel microphysics parameterization (Reisner et al., 1998) of MM5 to simulate the precipitation and ice physics. When compared to the observed rainfall amount in Fukushima Prefecture (Fig. S1), the new calculations were overall the same as or sometimes better than Katata et al. (2012b) and Terada et al. (2012). During 15–17 March 2011, the model also reproduced the upper-air observations of wind and air temperature above 400 m at Ibaraki Prefecture (Fig. S2). The ratios of gaseous and particulate ^{131}I for the input data of modified WSPEEDI-II were determined from the air concentration data collected at JAEA-Tokai (Ohkura et al., 2012). Te-132 should be a particulate in the atmosphere,

similar to ^{134}Cs and ^{137}Cs, according to the observational data of Ohkura et al. (2012) (Fig. 2b). The WSPEEDI-II calculation for the inverse estimation over the ocean was conducted using the GPV of the GSM by JMA. Time steps of MM5 and GEARN are set to 120 s and 60 s, respectively. The physical schemes of MM5 are the same as those used in the calculations for the reverse estimation over the land.

The time step in SEA-GEARN-FDM calculations is set to 60 min. The calculation period of SEA-GEARN was from 12 March to 30 June. Cesium-134 was used in the inverse estimation calculation. The horizontal spatial resolution of the model was set to $1^{\circ} \times 1^{\circ}$ with 45 vertical layers. The calculated deposition amounts by WSPEEDI-II were given to the surface layer of SEA-GEARN-FDM every 24 h.

3 Results

3.1 Source term estimation and local-scale dispersion analysis

The estimated source term is shown in Table 5 and the time trend of the release rates is depicted in Fig. 7. The relation of the estimated source term with the events in the reactors (TEPCO, 2011a, 2012; Tanabe, 2012) and the environmental monitoring data is described in the following subsections. The simulated deposition patterns of ^{137}Cs over the land are also shown in Fig. 8 to discuss the relation between the atmospheric releases and the extension of contamination over East Japan. Note that the time zone used in the following sections is Japan Standard Time (JST = UTC + 9 h).

3.1.1 12 March

During the morning of 12 March, a monitoring car at the main gate of FNPS1 and several monitoring stations of Fukushima Prefecture observed increases in the air dose rates. In addition, dust monitoring cars also detected ^{131}I and ^{137}Cs at several points around FNPS1 (METI, 2011a). Although these increases were probably due to

the leakage of radionuclides from the primary containment vessel of Unit 1 (PCV-U1) and/or the wet venting of Unit 1 at 10:17, the levels were lower than those detected at later stages of the accident.

In the afternoon, the wet venting that started at 14:00 and the extreme decrease of the pressure of PCV-U1 during the period from 14:30 to 15:00 indicated an atmospheric discharge of radionuclides. The air dose rates at the Kamihatori monitoring station (5 km northwest from FNPS1) increased to 1590 μGy h^{-1} at 15:00, and then rapidly decreased (Fig. 9a). The atmospheric transport and deposition simulations by WSPEEDI-II (hereafter the WSPEEDI simulation) showed this high air dose rate was due to the large releases during the wet venting of Unit 1. The estimated release rates were 2.3×10^{15} and 2.3×10^{14} Bq h^{-1} for ^{131}I and ^{137}Cs, respectively, which were approximately two-hundred times higher than estimated values during the morning. Here, we assumed that the release started just after the venting operation at 14:00 and continued until the end of the extreme decrease in the pressure of PCV-U1.

The hydrogen explosion of Unit 1 at 15:36 also discharged a huge amount of radionuclides into the atmosphere. The estimated release rates from 15:30–16:00 were 1.1×10^{16} and 1.1×10^{15} Bq h^{-1} for ^{131}I and ^{137}Cs, respectively. According to the WSPEEDI simulation, the radioactive plume flowed toward north-northwest, which drastically increased the air dose rates at monitoring posts of Shinzan (3.9 km north-northwest), Namie (8.6 km north-northwest), Kiyohashi (8.2 km north), and Minamisoma (24.9 km north-northwest) in Fukushima Prefecture, starting at 17:00, 17:00, 20:00, and 20:00, respectively. These increases of the air dose rate due to the hydrogen explosion are supported by airborne survey within 5 km from FNPS1 (Fig. 10), which shows a narrow contaminations band to the north-northwest direction of FNPS1 in both air dose rate and ^{137}Cs deposition. Because large increases of the air dose rates were not recorded in the areas from north-northwest to north directions of FNPS1 after 13 March, this contamination band over the monitoring post of Shinzan must have been due to the dry deposition of radionuclides discharged by the hydrogen explosion. The contamination band is narrow despite the fact that the wind direction observed at

FNPS1 (METI, 2011b) rapidly changed in a clockwise direction during that period. The narrow deposition band indicates that the major release due to hydrogen explosion was instantaneous. In contrast to the hydrogen explosion, the contamination by wet venting from 14:00 as estimated above did not clearly appear in Fig. 10 because the deposition area was far from the plant due to the elevated release from the stack (120 m in height) and was also overlapped by much higher deposition during the major releases from 15–16 March (Sect. 3.1.4).

The WSPEEDI simulation showed that the plume discharged by the hydrogen explosion changed its direction to the north-northeast after passing the north side of the coast line of Fukushima Prefecture (Fig. 8a). Then, elevated radiation levels were detected at the nuclear power plant in Onagawa (116.5 km north-northeast) at 0:00 on 13 March (Tohoku Electric Power, 2011). Afterwards, the plume dispersed over the north part of Pacific Ocean, and reached the west coast of the United States on 18–19 and 21–22 March (Fig. 6a and c), Sand Point in Alaska on 20–21 March (Fig. 6b), and Oahu in Hawaii on 20–21 March (Fig. 6b).

3.1.2 13 March–evening of 14 March

Venting operations were conducted to decrease the pressure of PCV-U3 at 9:24 and 12:30 on 13 March. The WSPEEDI simulation showed that the plume almost flowed toward the ocean in that period. Although the plume sometimes flowed over the coastline of Fukushima Prefecture or stagnated around FNPS1 due to calm conditions, only a very small number of monitoring posts near the coast caught the movement of the plume (Fukushima Prefecture, 2012). The estimation result shows that the large releases due to wet venting continued until 23:00 on 13 March on the order of 10^{14} and 10^{13} Bq h^{-1} for ^{131}I and ^{137}Cs, respectively. The plume discharged during the period broadly dispersed over the Pacific Ocean and increased air concentration at Sacramento California, Melbourne Florida, Sand Point Alaska, and Oahu Hawaii in 23–25 March (Fig. 6e).

Despite several venting operations at Unit 3 on 13 and 14 March, a hydrogen explosion also occurred at Unit 3 at 11:01 on 14 March (Fig. 7). According to our estimation, the release rates of ^{131}I and ^{137}Cs were 3.2×10^{15} and 3.2×10^{14} Bq h^{-1} for about 30 min, respectively, which were slightly smaller than those of the hydrogen explosion at Unit 1 (Sect. 3.1.1).

3.1.3 Night of 14 March–early morning of 15 March

Figure 11a and b depict the time evolution of the pressure of the reactor pressure vessel (RPV) at Unit 2 and the air dose rates and air concentrations measured at areas to the south of FNPS1. During this period, dry venting was tried at Unit 2, but it is not clear that the venting succeeded. The safety relief valve (SRV) was also opened at 21:00 and 23:00 on 14 March, and at 1:00 on 15 March to decrease the pressure of RPV and the pressures actually decreased (Fig. 11a). If a meltdown had already occurred in Unit 2, the vapor containing radionuclides would flow to the PCV and raise the possibility of atmospheric releases with the operation of SRV. In this period, the plume flowed toward the south to south-southwest and the observed air dose rates at FNPS2 (11.4 km south), Kitaibaraki (80 km south), and air concentrations of ^{131}I and ^{137}Cs at JAEA-Tokai (100 km south) showed three increases with time (Fig. 11b). Based upon the downwind distances from FNPS1 and the wind speed data, the time of appearance of the peaks at these three monitoring points were reasonably explained by the releases when the SRV was opened (Fig. 11a and b). In our source term estimation, the release rates in this period gradually increased with time from 2.3×10^{14} to 1.5×10^{15} Bq h^{-1} and from 1.5×10^{13} to 2.3×10^{14} Bq h^{-1} for ^{131}I and ^{137}Cs, respectively. These results indicate that the three-time large increases of releases as shown in our source term estimation occurred due to the opening of SRV.

The WSPEEDI simulation showed that this plume formed the high contaminated area of dry deposition along the southeastern coast and northeastern areas of Fukushima and Ibaraki Prefectures in the morning of 15 March, respectively (Fig. 11b). The plume then successively dispersed over Tokyo, Saitama, and Kanagawa Prefectures,

although the amount of dry deposition was not significant when the plume passed through those areas. From the afternoon of 15 March, precipitation was observed broadly across eastern Japan, due to the transient cyclone passing over East Japan (Morino et al., 2011; Terada et al., 2012). The plume finally encountered a rain band over the areas of Gunma, Tochigi, and Fukushima Prefectures., and this caused a large amount of wet deposition from the afternoon to the evening (Fig. 8c).

3.1.4 Morning of 15 March–early morning of 16 March

In the morning of 15 March, the pressure of PCV-U2 decreased between 7:00 and 12:00. This decrease corresponded with the extreme increase of air dose rate (peak approximately 1.5×10^4 μGy h^{-1}) observed at the main gate from 7:00 to 10:00, clearly indicating a huge release into the atmosphere. The release rate from 7:00 to 11:00 was estimated on the order of 10^{15} and 10^{14} Bq h^{-1} for ^{131}I and ^{137}Cs, respectively. The air dose rate map from the airborne survey of 17–19 March (US DOE/NNSA, 2011) is shown in Fig. 12a. This figure showed that the high dose rate zone due to dry deposition to the southwest was narrow suggesting that the period of the large release in the morning did not continue for very long. Figure 11c and d shows the temporal change in the drywell (DW) pressure at Units 2 and 3 and air dose rates observed around the plant. The time trend of the vertically accumulated air concentration and precipitation band during this period by the WSPEEDI simulation is shown in Fig. 13. According to the WSPEEDI simulation, the plume discharged in the morning first flowed toward the south-southwest and then gradually changed direction clockwise, also analyzed by Katata et al. (2012a). Around the area of FNPS1, the observed air dose rates first increased to 41 and 19 μGy h^{-1} at the two monitoring posts of Yonomori (7.3 km south-southwest) and at Matsudate (14.2 km south-southwest) at 7:00 on 15 March, respectively. Subsequently the following monitoring points detected higher air dose rates: 390 μGy h^{-1} at Ohno (4.9 km west-southwest) at 11:00, and 232 μGy h^{-1} at Yamada (4.1 km west-northwest) at 13:00 (Fig. 11d). This plume encountered light rain or drizzle bands along the Naka-Dori including Koriyama (58 km W) and Shirakawa (81 km

WSW) (Fig. 13a) and the north and northwest areas of FNPS1 including Fukushima (62.7 km NW) and Iitate (38.9 km NW) (Fig. 13b).

After the major release in the morning of 15 March, the decrease in the pressure of the DW at Unit 2 continued from afternoon to the evening (Fig. 11c). A southeasterly wind caused the emission during the period to flow directly toward Iitate and Fukushima, and resulted in a large amount of wet deposition to the northwest of the plant, as discussed in Katata et al. (2012a). However by our estimates, the release rates were not as high during the morning releases (Table 4), which was different from our previous study (Katata et al., 2012a) due to modifications of the deposition scheme (Sect. 4.1). We speculate that the release in the morning was larger than in the afternoon because a large increase in the air dose rates did not appear at Fukushima and Iitate areas to the the west and west-northwest of FNPS1, respectively. Afterward, the air dose rates largely increased around 13:00–14:00 on 15 March due to wet deposition of the plume that was released during the morning (Fig. S3).

The second huge increase of the release rate was estimated during the period from 18:00 of 15 March to 1:00 of 16 March with the maximum values from 20:00–22:00 on 15 March of 1.0×10^{16} and 1.5×10^{14} Bq h^{-1} for ^{131}I and ^{137}Cs. During the evening of 15 March, wet venting was conducted at Unit 3, corresponding to the decline in DW pressure at Unit 3 from 16:05 (Fig. 11c). Afterwards, wet venting was carried out at Unit 3 several times, and the decline in DW pressure finally stopped around 6:00 on 16 March. At the same time, the DW pressure dropped steeply at Unit 2 from 18:00 on 15 March to 2:00 on 16 March. These facts indicate that the large release rate estimated during the evening originated from Units 2 and 3. The WSPEEDI simulation showed that after the plume flowed clockwise from a west to northwest direction in the afternoon; it reached Namie (8.6 km north-northwest) at 21:00 on 15 March, and then the flow direction switched to counter-clockwise. At midnight on 15 March, the wind direction was from the east and the rain band approached FNPS1 (Fig. 13c), suggested by both the WSPEEDI simulations and the meteorological data at Ohno (Fig. S1). Furthermore, the air dose rates observed at monitoring posts on 16 March

drastically increased to 1020 μGy h^{-1} at Yamada at 0:00, 173 μGy h^{-1} at Ono at 1:00, and 44.5 μGy h^{-1} at Matsudate at 3:00 (Fig. 11d). Thus, the release around midnight on 15 March is considered to have created the highest dose rate zone in the western area close to FNPS1 between Yamada and Ohno, as shown by 5 km airborne survey (Fig. 10). At these locations, decreases of the air dose rates after the passage of the plume were small (Fig. 11d), indicating that this high dose rate zone was created by wet deposition. The 5 km airborne survey showed two clear high-contaminated bands to the west of FNPS1 between Yamada and Ohno, indicating the short-term variation in release rates during the period, while the temporal and spatial resolution of WSPEEDI simulations are not detailed enough to distinguish these bands.

Our source term estimation results and the local-scale atmospheric dispersion analysis from 15–16 March revealed that the highest contamination areas around the FNPS1 were not continuous but consisted of two parts; i.e., the west area close to the site including Yamada and Ohno, and the northwest band far away from FNPS1 including Iitate and Fukushima. Although wet deposition on 15–16 March is known to have created these zones as concluded in Chino et al. (2011), Katata et al. (2012a), and later studies (Mathieu et al., 2012; Srinvas et al., 2012; Korsakissok et al., 2013; Morino et al., 2013; Winiarek et al., 2014), our results indicated that the formation process of the highest dose rate zones near the plant were quite complicated.

More importantly, this interpretation enables us to understand the detailed dispersion and deposition patterns of the high-concentration plume. The spatial pattern of the high dose rate zone measured by the airborne survey on 17–19 March (Fig. 12a) shows the highest dose rate zones into two different directions near the plant. The explanation is that the northwest contamination area was created by the releases in both the morning and the afternoon of 15 March, and then the high-concentration plume discharged during the evening and night contaminated the west and west-southwest areas near the site. The above two contaminated areas in different directions of FNPS1 were created at different times. This conclusion is also supported by the 5 km airborne survey

(Fig. 10) showing the contamination areas near the site distributed not northwest direction but west-northwest and west directions of FNPS1.

Figure 12b and c shows the deposition distributions of ^{131}I and ^{137}Cs in the area within 80 km from FNPS1 observed by the airborne survey. The figure shows that the distribution patterns of both radionuclides are slightly different, e.g., the large deposition area of ^{137}Cs is limited to the narrow band to the northwest and south directions, while that of ^{131}I is distributed toward the west and southwest areas within 10 km from FNPS1. As discussed above, the major deposition of ^{131}I in the west and southwest areas was probably created by wet deposition during the midnight on 15 March when the rain band overlapped with the high-concentration plume. The WSPEEDI simulation showed that this plume flowed to the south of FNPS1 and reached JAEA-Tokai in the morning of 16 March. This movement contributed to the creation of the contaminated area in the south close to FNPS1 (Fig. 10). As described in Sect. 2.4, the ratio of ^{131}I/^{137}Cs = 50 sampled at JAEA-Tokai on 16 March was clearly higher than that of ^{131}I/^{137}Cs = 7.7 on 15 March (Ohkura et al., 2012). Therefore, it can be concluded that the high-concentration plume discharged near midnight was iodine-rich, resulting in the large deposition of ^{131}I near the plant compared with that of ^{137}Cs. One possible reason for the change in the ratio of ^{131}I/^{137}Cs at JAEA-Tokai from 15 and 16 March is that, according DW pressure data (Fig. 11c), the source was from Unit 2 on 15 March and Units 2 and 3 on 16 March. The ratio of gaseous to particulate iodine is also larger in the plume discharged on 16 March than that on 15 March, which increased the deposition amount of gaseous iodine to the areas west and southwest, while it did not have a large contribution to the formation of high dose rate zone (Sect. 4.2).

3.1.5 Morning–noon of 16 March

A pressure decrease was reported at Unit 3 from 9:00 to 11:00 on 16 March (Fig. 7). According to our source term estimation, the release rate increased to 2.1×10^{15} and 2.1×10^{14} Bq h^{-1} for ^{131}I and ^{137}Cs, respectively. Although the plume flowed toward the Pacific Ocean in the morning, large increases of air dose rates, to 33 and 324 μGy h^{-1},

appeared again at Matsudate and Ohno at 11:00 and 12:00 on 16 March, respectively (Fig. 11d). The WSPEEDI simulation showed that after the plume flowed toward the ocean, it returned inland around noon and increased the air dose rates near FNPS1 (Fig. 13d).

3.1.6 Noon of 16 March–early morning of 20 March

In this period, wet venting was done at Unit 3 on 21:30 of 17 March and 5:30 of 18 March (Fig. 7). According to our estimation, these events generated atmospheric releases on the order of 10^{14}–10^{15} and 10^{13}–10^{14} Bq h^{-1} for ^{131}I and ^{137}Cs. The WSPEEDI simulation shows that the plume primarily flowed toward the Pacific Ocean by the westerly and northwesterly winds from 16–19 March. As shown in Fig. 6d and f, this plume affected the air concentrations monitored at Sand Point in Alaska and Oahu in Hawaii on 22–23 and 26–27 March, respectively.

3.1.7 Early morning of 20 March to 24 March

The estimated release rates of ^{131}I were generally in the range of 2.2–1.6×10^{14} Bq h^{-1} from 20–23 March but with smaller release rates (4.1×10^{13} Bq h^{-1}) for an eight hour period from 8:00–16:00 on 21 March. In contrast, the release rates of ^{137}Cs rapidly decreased from the morning of 21 March down to the order of 10^{12} Bq h^{-1}. In this period, wet venting at Unit 3 at 11:25 on 20 March was reported (Fig. 7). Furthermore, Tanabe (2012) discussed the possibility of a core fuel materials re-melt at Units 3 and 1 on 21 March and 22–23 March, respectively, due to water shortage to cool the molten cores. The white and gray smoke that was observed at Unit 3 at 15:55 on 21 March and at 16:20 on 23 March, indicated a possible fire (Prime Minister of Japan and His Cabinet, 2011; TEPCO, 2011a). Unfortunately, the major automated monitoring stations near FNPS1 were shut down due to a limitation in the emergency electric power supply. Although several portable monitoring posts (Fukushima Prefecture, 2011a, b) were available in the Fukushima Prefecture, the air dose rate peaks (when the plume

passed through) were unclear because of the high air dose rate background levels (i.e., the ground-shine formed before 20 March). The lack of monitoring made it difficult to clarify the plume movement and the relationship between the time trend of estimated release rates and the above events at FNPS1 during this period. Meanwhile, the dust sampling data in Fukushima Prefecture (NRA, 2012b) showed very high concentrations of ^{131}I and ^{137}Cs up to 5600 and 1000 Bq m^{-3}, respectively (Table 3, Fig. 2d), indicating a large release of radionuclides.

The main features of the regional-scale atmospheric dispersion after 20 March are similar to that of our previous study (Terada et al., 2012). The WSPEEDI simulation shows that radionuclides discharged in the period mainly dispersed over the boundary of Iwate and Miyagi Prefectures the on 20 March (Fig. 8g) and Kanto region from 21–22 March (Fig. 8h) and contaminated these areas by wet deposition. For ^{131}I, the major (wet) deposition occurred over areas to the south and south-southwest areas of the FNPS1 (Fig. 12c) during the latter part of this period (not shown in the figure).

3.1.8 25–29 March

In this period, the estimated release rates of ^{131}I gradually decreased to the order of 10^{12} Bq h^{-1}, while the release of ^{137}Cs remained almost constant resulting in a decreased difference in the release rates between both radionuclides. The WSPEEDI simulation shows that from the afternoon to the night on 25 March, the plume was transported by the southeasterly wind from FNPS1 which resulted in wet deposition over Fukushima Prefecture and the southern areas of the Yamagata and Miyagi Prefectures. Then, the plume changed its direction counter-clockwise from northwest to southeast in the morning on 26 March. The plume continuously flowed toward the ocean until 29 March.

3.1.9 30–31 March

Due to a shortage of water for core cooling, Tanabe (2012) addressed the possibility of the core re-melting at Unit 2 on 30 March because the temperature inside Unit 2 was high between 13:00–16:00 on 29 March and again at 22:00 on 31 March. The estimated release rates of ^{131}I temporally increased up to 5.9×10^{13} Bq h^{-1} (4.9×10^{13} Bq h^{-1} for ^{137}Cs), which was comparable to the highest release rates from 21 to 25 March. The WSPEEDI simulation shows that the plume turned clockwise from the east to the southwest direction of FNPS1 and flowed over the Kanto region on the morning of 30 March. In the afternoon, wet deposition of this plume occurred over Tochigi and Ibaraki Prefectures. After the plume passed through the area northwest of FNPS1 during the afternoon and night, it head toward the ocean on 31 March (Fig. 8i).

The total release amounts of total ^{131}I and ^{137}Cs through the end of March were 142.9 PBq and 12.4 PBq, respectively.

3.2 Verification of source term

In this subsection, we first test the new source term for ^{137}Cs and ^{131}I with the modified WSPEEDI-II and compare the results over local- and regional-scales to the airborne survey's surface deposition and air dose rate data. Then, the new source term is further tested using different atmospheric dispersion and meteorological models over regional- and global-scales to evaluate its reliability for general atmospheric dispersion simulations using models that were not part of the source term estimation.

3.2.1 Validation using WSPEEDI-II

Optimization results by reverse and inverse estimation methods

By optimizing the source term using the reverse estimation method, the calculated ground-shine due to the large deposition event of 15–16 March agreed with observed data within a factor of 2 at most of the monitoring posts (Fig. S3). In particular, the

highest ground-shine observed at Yamada was accurately reproduced in the WSPEEDI simulation, while it was clearly underestimated in our prior work (Katata et al., 2012b).

Statistical comparisons of the calculated and observed sea surface concentrations of ^{134}Cs in Pacific Ocean are shown in Table 6. After using the inverse estimation method from the coupled WSPEEDI-II and SEA-GEARN-FDM simulations (Sect. 2.3), the accuracy of sea surface concentration of ^{134}Cs using WSPEEDI-II improved overall as most of the calculated concentrations within a factor of 10 of the observed concentrations (Table 6, Fig. S4).

Regional deposition of ^{137}Cs over East Japan

As described in Sect. 1, our previous study (Terada et al., 2012) showed some disagreement in the surface deposition of ^{137}Cs between observations from the airborne survey and the calculations at several areas over East Japan. In contrast, as shown in Fig. 8i, this issue was resolved in the revised WSPEEDI simulation. For example, although a large amount of ^{137}Cs deposition was seen in the south of Niigata Prefecture and the west of Fukushima (Terada et al., 2012), the model in this study reproduced the contaminated areas observed in the airborne survey in Tochigi and Gunma Prefectures and Naka-Dori in the middle of Fukushima Prefecture. Furthermore, the overestimation of surface deposition from the north part of Fukushima Prefecture to Miyagi Prefecture (Terada et al., 2012) completely disappeared in the WSPEEDI simulation. Both improvements resulted from the enhancement of the scavenging coefficient by including in-cloud scavenging in the modified wet deposition scheme (Fig. A2a) and the revised source term during 15–16 March. The scatter plots (Fig. 14a and b) and statistics (Table 6) show that the simulation accuracy of the spatial pattern of the high contamination areas over East Japan was improved in the WSPEEDI simulation.

Local depositions of ^{131}I and ^{137}Cs over Fukushima Prefecture

Figure 15a and b shows the spatial distribution of the calculated cumulative surface deposition of ^{137}Cs and ^{131}I around FNPS1, respectively. Comparisons of these figures with the observations (Fig. 12b and c) show that the model reproduced the deposition patterns of each radionuclide; i.e., the large deposition area of ^{137}Cs is limited to the northwest direction of FNPS1 compared with that of ^{131}I which has a larger southern component. This indicates that the new source term, which increases in the ratio of ^{131}I to ^{137}Cs around midnight on 15 March (Sect. 3.1.4) reproduced the difference in the observed deposition patterns between both radionuclides in the WSPEEDI simulation. Figures 14c and d show the scatter plots of surface deposition for ^{137}Cs and ^{131}I and at most locations near the plant the calculation results agreed with airborne observations within a factor of 10.

Local air dose rate over Fukushima Prefecture

In addition to the surface deposition, the spatial patterns in calculated and observed air dose rates just after the formation of the highest contamination areas near FNPS1 (17–18 March) were compared for the northwest and southwest regions of the plant (Figs. 15c and 16). In our previous study (Katata et al., 2012b), we underestimated the observed air dose rate in both regions (Fig. 16a and c). In contrast, the current WSPEEDI simulation reproduced the high dose rate zones (Fig. 15c) and the slopes of the calculations to the observations in the scatter diagrams were close to unity (Fig. 16b and d). These performance improvements indicate that the modification of new deposition scheme and source term are reasonable, particularly for ^{132}Te and ^{131}I, which are the major contributors to the ground-shine in the early phases of the accident.

The statistical comparisons of the surface deposition of ^{131}I and ^{137}Cs, and air dose rate over regional- and local-scales are summarized in Table 6. In general, the WSPEEDI simulation reproduced each observational data set, and furthermore, the results showed higher statistical scores than our previous results (Katata et al., 2012b;

Terada et al., 2012). Most of data points (79–95 %) of air dose rate and cumulative surface depositions were within a factor 5. Therefore, it can be concluded that our revised emission estimates for the major releases during the FNPS1 accident are reasonable.

3.2.2 Validation using several regional and global atmospheric dispersion models

To evaluate the new source term independently of the one dispersion model used to develop the source term, numerical simulations from three atmospheric dispersion models (MLDP0; D'Amours et al., 2010, HYSPLIT; Draxler and Rolph, 2012, and NAME; Jones et al., 2007) were compared to observations using our new source term estimates. These model simulations, organized by the World Meteorological Organization (WMO, 2014), were initially conducted prior to our study to assist the Scientific Committee on the Effects of Atomic Radiation (UNSCEAR, 2014) in its dose assessment efforts. The WMO sponsored calculations were all done in 3 h time segments using a unit source emission rate, which permitted their use with our revised source term. The calculations from the above mentioned three models as well as several others are available on-line (NOAA, 2014) where any source term combination can be interactively evaluated and compared with observations.

The simulation settings of the deposition scheme in each atmospheric dispersion model are summarized in Table 1. Meteorological data from the Meso-Scale Model (MSM) were provided by the Japan Meteorological Agency (JMA) at three-hourly intervals and a 5 km horizontal resolution and were used to drive the three dispersion models. For NAME, two additional meteorological input data were used in the calculations to evaluate the surface deposition patterns under different meteorological conditions: the JMA radar/rain gauge-analyzed precipitation fields (MSM-RAP, 1 km resolution at 30 min intervals) and European Centre for Medium-Range Weather Forecasts (ECMWF, 0.125° resolution at 3 h intervals). A one-domain calculation covering East Japan was carried out for each model run from 11–31 March 2011. Details of simulation settings are available in Draxler et al. (2014). Both the MLDP0 and NAME

calculations were the original WMO (2014) calculations. However, the HYSPLIT calculation settings were changed from the original calculation to turn off the use of the vertical motion field from MSM. Both the original and revised NOAA calculations are available on-line (NOAA, 2014). Two source terms, Terada et al. (2012) and this study, averaged at 3 h intervals, were used for the emission scenarios.

Figure 17 shows the temporal changes in air concentrations at JAEA-Tokai in the simulations using the three WMO models. Modeled results using the source terms of this study and Terada et al. (2012) generally reproduced the observed time trends of air concentrations such as the high values observed on 15, 16, 20–21, and 30 March. The scatter plots between observed and modeled concentrations with the new source term are depicted in Fig. 18. Although there are biases depending on the model, good correlations are generally found in the diagrams as also shown in comparisons of the time series (Fig. 17), indicating that the new source term would be suitable for regional atmospheric dispersion simulations of the FNPS1 accident.

Figure 19 shows the spatial distributions of the cumulative ^{137}Cs surface deposition over East Japan calculated using three WMO models. In contrast to air concentration (Fig. 17), the improvement when using the new source term compared with Terada et al. (2012) is more obvious in the deposition pattern. In particular, the calculated large deposition areas extending from the north part of Fukushima Prefecture to Miyagi Prefecture not observed by the airborne survey (NRA, 2012a), significantly decreased when using the new source term because of a decrease of release rates during the afternoon of 15 March (Sect. 3.1.4). This is also apparent in the scatter plots (Fig. 20), which show overestimation in the range of measured surface deposition between 10–1000 kBq m^{-2} for all model results using the source term of Terada et al. (2012) (Fig. 20b) which is similar to the results shown in Fig. 14a. The differences in slopes between observations and calculations can be explained by differences in the wet scavenging schemes of each model. For example, MLDP0 showed underestimation of measurements as indicated from the slope less than the unity. This model does not use the precipitation field directly as other atmospheric transport and dispersion

models. Wet deposition is treated with a simple scheme and will occur when a particle is presumed to be in a cloud (in-cloud scavenging) and is modeled in terms of a wet scavenging rate. The tracer removal rate is proportional to the wet scavenging coefficient, the local cloud fraction (parameterized as a function of relative humidity), and the particle mass. Therefore, the resulting low values of the wet scavenging coefficient (order of 10^{-5} s^{-1} as in the original WSPEEDI-II, Fig. A2a) and/or cloud fraction may contribute to the underestimation of ^{137}Cs deposition measurements. In contrast, NAME showed a slope value close to the unity (Fig. 20b) because the model applies a larger value of scavenging coefficient, generally on the order of 10^{-4}–10^{-3} s^{-1}, by considering the enhancement of wet deposition due to in-cloud scavenging and orographical (seeder–feeder) effects under both rain and snow situations. This is similar to the value of scavenging coefficient in our modified scheme with a small cloud liquid water content (Fig. A2a), resulting in the good correlation to the calculation results in the WSPEEDI simulation (Fig. 14b). Similar results were also obtained in the parametric study of Morino et al. (2013) by changing the scavenging coefficient in the atmospheric dispersion model of CMAQ.

Figure 21a compares the spatial distributions of cumulative deposition of ^{137}Cs calculated by NAME with different meteorological input data. Although the highest dose rate zone lay northwest from FNPS1 in all the calculation results, several differences were found in the deposition patterns in East Japan when they were compared with observations from the airborne survey. For example, the observed high deposition region along the mountain areas in Tochigi and Gunma Prefectures was not reproduced in the calculations of NAME-MSM-RAP. This is because very little precipitation was detected by the radar/rain gauge observations when the plume passed over those regions during the afternoon on 15 March. This indicates that both NAME-MSM and NAME-ECMWF have a possibility to overestimate observed precipitation in this region. Furthermore, NAME-ECMWF calculations produced a large amount of surface deposition to the northwest near FNPS1 compared with NAME-MSM and NAME-MSM-RAP. This is caused by the overestimation of precipitation intensity near the plant calculated

by ECMWF (not shown in the figure). As shown in scatter plots comparing observations with calculations (Fig. 21b), the prediction accuracy seems to be the best when the input data of MSM are used with the NAME model.

The summary of the statistical comparisons for air concentration and surface deposition based on the regional WMO modeling is shown in Table 7. It is not straightforward to determine the superior source term because the variations in the statistical scores also strongly depend upon the model. Nevertheless, the correlation coefficients of air concentrations for both radionuclides with the new source term were higher than those of Terada et al. (2012), suggesting that the new source term provides more reasonable time trends in the release rate. The statistical ranks for the surface deposition of ^{137}Cs using the new source term were overall lower than those of Terada et al. (2012), which are also shown by increases in the normalized mean square error (NMSE). Consequently, 92, 66, and 91 % of calculated surface deposition with the new source term for MLDP0, HYSPLIT, and NAME, respectively, were within a factor of 5 of the measurements.

For testing the new source term for the plume flowing over the ocean, the global simulation results from HYSPLIT were compared with measurements at several locations over the Pacific, the Americas, and Europe. The global HYSPLIT simulations had previously been described by Draxler and Rolph (2012). The model configuration used here is identical except that the computational particle release rate was increased to 100 000 per hour for each six hour time segment. The calculations used the 0.5° horizontal resolution meteorological data from NOAA's Global Forecast System (GFS), consisting of a series of 0 to +6 h forecasts available on GFS native model sigma levels (56) with meteorological fields available every three hours. The concentration grid was global at 1-degree horizontal resolution with a vertical extent of 500 m. The global measurement data used for the evaluations consisted of the United States' National Data Center (US NDC, 2011) and Health Canada's Radiation Monitoring (HCRM, 2011) stations in the Comprehensive Test Ban Treaty Organization's (CTBTO) network, the US Environmental Protection Agency's Radiation Monitoring Network (RADNET, 2011), and selected

stations in Europe run by various national authorities (Masson et al., 2011). The model was run with a unit emission so that different emission scenarios could easily be tested. Interactive model results and verification are also available on-line (NOAA, 2012).

Figures 22 and 23 show the time series in air concentrations of particulate and gaseous ^{131}I and ^{137}Cs at a few selected locations in North America, Hawaii, Alaska, Ireland, and Canada representing the emissions from FNPS1 that flowed over the Pacific Ocean and arrived during the early phases of the accident. For both radionuclides, there is a good coincidence in the first arrival time of the plume. In particular, the general time trends in particulate ^{131}I concentrations were quite well reproduced by HYSPLIT with the new source term at most of the stations.

Scatter diagrams of the observed and calculated air concentrations for the global scale results using HYSPLIT with the new source term were depicted in Fig. 24. General results of both gaseous and particulate ^{131}I were better than those of ^{137}Cs. There are several possible explanations for these results. One is that the initial higher source terms for iodine and its larger decay compared with cesium would mean that the early emissions dominate the downwind air concentrations which is related to the uncertainty in the ratio of ^{131}I/^{137}Cs for major releases during the early stages of the accident due to lack of dust data. Another possibility is that the model's deposition parameters were more appropriate for iodine than cesium. In HYSPLIT, the same parameters for wet and dry deposition are applied to particulate cesium and iodine. Another possibility is that perhaps some of the gaseous iodine was converted to particulate form (Uematsu et al., 1988) resulting in a preferentially smaller particle size compared with cesium. Perhaps cesium and iodine attached to other larger particles with different scavenging efficiencies.

Table 8 summarizes the global calculation statistics using HYSPLIT with the source terms of Terada et al. (2012) and this study. The correlation coefficients increased for both radionuclides and the other statistical scores were improved overall for ^{131}I when the new source term was used. More than 60 % of calculations agreed with observations within a factor of 5 for both radionuclides (not shown in the table). Considering

uncertainties of the model as discussed above and the fact that other global modeling results (Stohl et al., 2012; Christoudias and Lelieveld, 2013; Evangeliou et al., 2013) did not use any common standards in their evaluation metrics such as was used in the WMO (2014) regional model evaluations, we conclude that the good performance in these global-scale simulations obtained with HYSPLIT and the new source term was comparable with existing studies.

4 Discussion

4.1 Comparison in source terms

Figure 25 shows the source terms estimated in the present study and those from prior studies (Terada et al., 2012; Stohl et al., 2012; Hirao et al., 2013; Saunier et al., 2013; Winiarek et al., 201). In terms of the land contamination, the most important result of this study is that the highest release rates shifted from the afternoon to evening–nighttime on 15 March (Sect. 3.1.4). As a result, the period of the major release is now coincident with the wet venting at Unit 3 and DW pressure deficits at both Units 2 and 3 reported on 15–16 March (Fig. 7). This result is completely opposite to all the other studies based on the inverse estimation methods using regional (Hirao et al., 2013; Saunier et al., 2013), global (Stohl et al., 2012), and daily fallout and surface deposition datasets (Winiarek et al., 2014).

There are several reasons for the improved estimation of this major release. First, the results of local-scale simulations with much higher spatial resolution (1 km) were compared with the automated monitoring data of air dose rate close to FNPS1 (Fig. 3b) that were not available for any of the past studies. Second, we modified the wet scavenging scheme to increase wet deposition, particularly for conditions with low cloud water content (Fig. A2a). This caused an increase of the modeled ground-shine at Fukushima and Iitate and also decreased the release rate in the afternoon on 15 March because the previous model's under prediction no longer needed to be compensated by an in-

creased emission rate. Third, the time segment of release periods from 15–16 March was set to 1 h to resolve drastic temporal changes in the release rate. Our results show that combinations of local-scale monitoring and detailed numerical analysis using atmospheric dispersion models with sophisticated deposition schemes are the most important factors required to estimate the release rates associated with the time-varying events in the reactors (e.g., hydrogen explosion, venting, and pressure drop).

For the period when the plume flowed over the land from the night on 14 March to the morning 15 March, and from 20–21 March, the release rates of the new source term were on the same order of those estimated by previous regional simulation studies (Hirao et al., 2013; Saunier et al., 2013) as well as Terada et al. (2012). In other periods, Saunier et al. (2013) frequently shows higher release rates with uncertainties when the plume flowed toward the ocean. Winiarek et al. (2014) acknowledged that they also overestimated the release rate on 20, 22–23, 25, 27, and 30 March.

Interestingly, when the plume flowed toward the Pacific Ocean, our new source term often agreed well with that of Stohl et al. (2012), despite using the different estimation methods. The former used the data of sea surface concentration of ^{134}Cs, while the latter was mainly based on daily mean air concentration of ^{137}Cs sampled throughout the world. This indicates that the estimated values in this study were also indirectly confirmed as being reasonable.

Table 9 shows the total release amounts of ^{131}I and ^{137}Cs to the atmosphere from FNPS1. For both radionuclides, the total amounts estimated by coupling the atmospheric and oceanic simulations are clearly larger (approximately 19 and 3.6 PBq for ^{131}I and ^{137}Cs, respectively) than those of Terada et al. (2012). These increases were mainly due to an increase of the release rate when the plume flowed over the ocean resulting from the optimization of release rates using additional data over the land and the ocean. The estimated release amount of ^{137}Cs to the atmosphere was lower than those of prior studies (Stohl et al., 2012; Saunier et al., 2013; Winiarek et al., 2014).

4.2 Role in deposition process

Figure 26 shows the spatial maps of modeled cumulative dry and wet deposition for each radionuclide. Cumulative dry deposition of ^{131}I was largest for gaseous I_2, then particulate iodine, and finally gaseous CH_3I as indicated by the order of modeled deposition velocities (Fig. A1). Large dry deposition of gaseous I_2 over the ocean was caused by high release rates on the order of 10^{14} Bq h^{-1} and a large gas fraction up to 67 % of ^{131}I, from 22–24 March. These results indicate that both the gas and particle forms are important to predict the total dry deposition of ^{131}I in FNPS1 accident. In contrast, wet deposition of I_2 and CH_3I were significantly lower than particulate iodine due to the solubility of the gas species as modeled in Eq. (A7) (Fig. 26b). This indicates that the gas species of ^{131}I did not contribute to the contamination of East Japan.

As shown in Fig. 26b, in the WSPEEDI simulation, a large part of the regional-scale contamination was derived from in-cloud scavenging of particulate species; e.g., large deposition of ^{137}Cs in Fukushima, Gunma, and Tochigi Prefectures. This deposition was reproduced by using high values of the scavenging coefficient (Λ) ranging from 10^{-4}–10^{-2} s^{-1} on 15 March (Fig. S5). These values are similar to those used by the WRF-CMAQ atmospheric dispersion simulation (Morino et al., 2013). However, there is an unresolved issue regarding precipitation rates vs. scavenging efficiency as both models overestimated the observed precipitation amount over Tochigi and Gunma Prefectures (WSPEEDI, Fig. S1; WRF-CMAQ results are not shown in the figure). This is also apparent in comparisons between the calculation results of NAME-MSM and NAME-MSM-RAP (Fig. 21a) which showed that the contamination in the region was not reproduced by MSM-RAP assimilated precipitation because the data showed no radar or rain gauge rainfall. Such overestimation of precipitation was found at Yamagata Prefecture in the evening on 20 March (Fig. S1). Further work with improved precipitation fields for atmospheric dispersion simulation is clearly required to quantify the impact of in-cloud scavenging.

As described in Terada et al. (2012) and Kaneyasu et al. (2012), fog and drizzle were observed in the above region and Naka-Dori in the afternoon on 15 March. Figure 27a illustrates the distribution of calculated cumulative fogwater deposition of ^{137}Cs. In the WSPEEDI simulation, fogwater deposition does not make a large contribution to the total deposition (Fig. 27a) compared with wet deposition (Fig. 26b). However, the model clearly underestimated observed cloud liquid water content (CLW) derived from visibility data at Okunikko and Karuizawa in the afternoon on 15 March (Figs. 27a and S6), while modeled rainfall was overestimated (Fig. S1). Moreover, the microphysics and fogwater deposition schemes do not explicitly consider drizzle deposition, i.e., horizontal wind-driven precipitation of large droplets (typically 100–500 µm in diameter). Because the spatial pattern of calculated fog deposition was consistent with the large contamination areas in Tochigi and Gunma Prefectures (Fig. 27a), fog and drizzle may have contributed to the contamination in the area.

Figure 27b–f depicts the spatial patterns of CCN activation fraction (f_{ccn}) and the accretion efficiency of cloud droplets by settling ice crystals (i.e., snow and graupel) (f_{ice}) averaged for the atmospheric layers where the calculated plume existed. On 15 and 20 March, although most of areas showed the complete activation of aerosols ($f_{ccn} \approx 1$), aerosols were not completely activated on the windward side of the mountains in Gunma and Tochigi Prefectures. This is because the modeled vertical wind velocity was weak (< 0.1 m s^{-1}) in orographic clouds. In contrast, when the plume from FNPS1 flowed toward the southwestern direction on 21 March, aerosols in the plume were completely activated over the flat terrain of the Kanto region (Fig. 27f). This indicates that predicting the activation fraction of aerosols (i.e., aerosol size, hygroscopicity, and vertical wind velocity) is also important to the wet scavenging of radionuclides over the complex terrain.

On 15 and 20 March, ice crystals enhanced the wet scavenging by 1.2–1.6 times the scavenging coefficient of rain droplets along the plume pathway (Fig. 27c and e) due to high accretion rate of cloud by ice crystals compared with that by raindrops. This increase was mainly observed in the north part of Fukushima Prefecture and

Tohoku region during the FNPS1 accident because the water content consisted of large amounts of water from ice crystals under low air temperature conditions.

The total regional scale deposition budget was calculated in the WSPEEDI simulation using the new source term (Table 10). Twenty seven percent of the total ^{137}Cs release deposited to the land over East Japan, while 6 % deposited onto the ocean near the coast. More than 60 % of ^{137}Cs discharged from FNPS1 flowed out of the region, which was larger than estimated in prior studies using our previous source term (42 % in Terada et al., 2012; 54 % in Morino et al., 2013). The change is primarily because the release rates significantly increased from our prior source term when the plume flowed directly toward the ocean (Sect. 4.1).

As shown in Table 10, the contamination areas over the land were primarily caused by wet deposition and account for 20 % of to the total release amount. Dry deposition only accounted for 5 % of total release amount onto the land around the plant (Figs. 26a and 27a), which was clearly larger than that of the prior study (Morino et al., 2013). This difference is considered to be due to increases in the source term and dry deposition velocity. Although only 2 % of the release was removed by fogwater, this value may change if rainfall amount and drizzle and fog events in Tochigi and Gunma Prefectures are correctly reproduced by the model as previously discussed.

For the ecological assessment of radionuclides, deposition amounts of ^{137}Cs to the forest areas in East Japan (Fig. 4c) were calculated from the WSPEEDI simulation. A large part of ^{137}Cs discharged from the plant deposited to forest areas (20 %), corresponding to 73 % of total deposition over East Japan. The wet deposition was also dominant in forest regions representing 16 % of the total release amount compared with 3 % for dry and 1 % for fogwater deposition.

5 Conclusions

The detailed source term of total ^{131}I and ^{137}Cs was estimated by coupling the simulation of an atmospheric dispersion model (WSPEEDI-II) and an oceanic dispersion

model (SEA-GEARN-FDM) developed by the authors. To improve the accuracy of the predicted deposition patterns, we enhanced the deposition scheme of WSPEEDI-II to calculate dry deposition of gaseous and particulate substances, in-cloud scavenging, the consideration of CCN activation and subsequent wet scavenging by mixed-phase clouds, and the fogwater deposition of radionuclides. The source estimation was made in two steps: first, the reverse estimation method using the results from WSPEEDI-II by assuming unit release rate (1 Bq h^{-1}) was compared with measurement data to estimate the release rates over the land, and then when the plume flowed directly toward the Pacific Ocean, the interpolated release rates were revised by an inverse estimation method based on the coupled simulation of WSPEEDI-II and SEA-GEARN-FDM. Additional air dose rate data at automated monitoring posts, dust sampling, and an airborne survey, not available for our previous work (Terada et al., 2012), were also used for the source term estimation.

The major differences in the estimated source term in this work from our previous work are as follows: (1) afternoon of 12 March: the release amount from the wet venting of Unit 1 between 14:00 and 15:00 was newly estimated from the air dose rate at the automated monitoring post near FNPS1 using the reverse estimation method. The release rate was approximately half of that from the hydrogen explosion of Unit 1 at 15:36, which was also re-estimated using the data at the automated monitoring post. Although these estimated values require the composition data of the radionuclides released and sampled on 12 March to predict the air dose rate at the monitoring post, it is difficult to distinguish the contribution of each plume due to the continuing leakage from the primary contaminant vessel (PCV), wet venting, and the hydrogen explosion, which all contribute to the air concentration. (2) Morning of 13 March: the major release due to the wet venting and pressure decline of PCV at Unit 3 was estimated by the inverse estimation method using the sea surface concentration data. (3) Night of 14 March to early morning of 15 March: it was determined that the major release from Unit 2 could be separated into three time segments starting from 21:00, 23:00, and 01:00, although the previous study estimated one release rate for this entire period. The results suggest

a relationship between the operations of the Safety Relief Valve (SRV) of Unit 2 and discharges to the atmosphere. (4) Morning of 15 March to noon of 16 March: the major releases were estimated during three periods from 07:00 to 11:00, and from 18:00 on 15 March to 1:00 on 16 March, and from 9:00 to 11:00 on 16 March by the reverse estimation method using the air dose rate at automated monitoring posts near the plant. The first two release period rates were similar to those estimated by our previous work, while the third major release was estimated for the first time in this study. However, the second major release started 4 h later and continued for 3 h longer than the previous work. Furthermore, it was revealed that the plume of this release was iodine-rich compared with other releases, which was supported by the spatial patterns of the airborne survey of ^{131}I and ^{137}Cs depositions and the dust sampling data at JAEA-Tokai located 100 km south of FNPS1. The plume of the second release created the highest dose rate zone to the northwest of FNPS1 by wet deposition with complicated interactions between rainfall, plume movements, and temporal variety in the release rates. (5) After noon on 16 March: the time trend of the release rate is revised by using recently obtained monitoring data. The release rates estimated by the inverse estimation method using sea surface concentration data were several times larger than those estimated previously for the afternoon on 16 March to the noon on 19 March. For 22–25 March, the release rate corresponding to possible plant events (wet venting at Unit 3 on 20 March, and white and gray smoke from Unit 3 on 23 March, and re-melting of core fuel materials at Units 1 and 3 on 21–22 and at Unit 2 on 29 March) generally decreased the emission rates compared with the previous study, while the temporal changes of the release rate more closely follows a relationship to these events.

The total amounts of released ^{131}I and ^{137}Cs estimated in this work were 142.9 and 12.4 PBq, respectively, which were clearly larger than those of the previous work for both radionuclides. The major reason for this increase was that when the plume flowed toward the Pacific Ocean we directly computed a significantly larger release amount, while previously it was simply estimated by a temporal interpolation between release rates computed from land based measurements.

The new source term estimated in this study was first validated by comparing calculation results of the modified WSPEEDI-II (the WSPEEDI simulation) with the data of cumulative surface deposition of ^{137}Cs and ^{131}I and air dose rate over local- and regional-scales. The spatial patterns of cumulative surface deposition were reproduced in the WSPEEDI simulation. The simulation accuracies including both ^{137}Cs and ^{131}I were within a factor of 5 for 79–95 % of data points for cumulative surface deposition and air dose rate. Furthermore, the new source term was also tested with three atmospheric dispersion models (MLDP0, HYSPLIT, and NAME) for regional and global simulations. All models using the new source term and the same meteorological input data generally reproduced the time series of air concentrations at JAEA-Tokai and surface deposition of ^{137}Cs over East Japan. However, there are some differences in simulation accuracies among the three model results mainly due to the difference in their deposition schemes. The global calculations using HYSPLIT showed a good agreement with the time of the first arrivals of the plume by comparing the model results with daily mean air concentration data at various monitoring sites over North America, Hawaii, Alaska, Ireland, and Canada. Considering uncertainties due to lack of the data of ^{131}I/^{137}Cs ratios, the deposition parameters, and the gas-particle conversion for iodine, the result that more than 60 % of calculated air concentrations for both radionuclides agreed with observed ones within a factor of 5 indicated the applicability of the new source term for global-scale simulations.

Finally, the role of deposition process in the formation of contaminated areas was discussed in the WSPEEDI simulation. The simulation result revealed that gaseous elemental iodine (I_2) has a large contribution to cumulative dry deposition of ^{131}I particularly near the plant. This was not the case for wet deposition for both local- and regional-scales, where most of contamination areas were created by wet deposition (in-cloud scavenging) of particulate ^{131}I and ^{137}Cs. However, the result has uncertainties because of the over-prediction of precipitation amount and the high values required for the scavenging coefficient (Λ) with less cloud water content in Tochigi and Gunma Prefectures. Potential effects of drizzle and fog observed in this region should also be

considered to accurately estimate the wet deposition because the spatial distribution of fogwater also corresponded to the contamination areas. The process of cloud condensation nuclei (CCN) activation decreased the wet scavenging rate to some extent in the mountain areas of the same Prefectures. Meanwhile, in the northern part of Fukushima and Tohoku region, the existence of ice crystals increased the wet scavenging of radionuclides. In summary, the simulation suggested that approximately 27 % of ^{137}Cs discharged from FNPS1 to the atmosphere deposited to the land (73 % of deposition was to forest areas) in East Japan mainly due to wet deposition (in-cloud scavenging). For further analysis of the formation process of high-contamination areas, data assimilation of accurate precipitation amount (including drizzle/horizontal wind-driven rain) and experimental work for evaluation of each modeled deposition process are required.

Appendix A: Modifications of deposition scheme in WSPEEDI-II

The processes in the following subsections are incorporated into WSPEEDI-II to improve the accuracy of the source term estimation and the atmospheric dispersion simulation.

A1 Dry deposition of gases

Dry deposition flux of gases and particles is normally represented by the deposition velocity, V_d (m s^{-1}), and the concentration, c (Bq m^{-3}) according to the inferential technique (Hicks et al., 1987):

$$F = cV_d, \tag{A1}$$

where the downward flux is positive for F. As described in Sect. 1, WSPEEDI-II used the typical constant values for V_d over short vegetation, the same as many of the other dispersion models (Table 1). However, the V_d of gases and particles depends on many

factors such as the meteorological variables (wind speed and atmospheric stability), the physical-chemical forms of substances, and the land surface characters (Katata et al., 2011b). To improve the accuracy of dry deposition by considering the influence of these factors, the more sophisticated resistance model of Zhang et al. (2003) for gaseous radioactive iodine (I_2 and CH_3I) is incorporated into WSPEEDI-II.

The original model of Zhang et al. (2003) calculates the deposition velocity of gases (V_{dg}) based on the big-leaf resistance modeling approach for various chemical species. Deposition velocity is parameterized by an analogy to electrical flow through a series of transfer resistances. The model of Zhang et al. (2003) considers transfer resistances of the aerodynamic, quasi-laminar sublayer, and overall canopy resistance. The canopy resistance is separated into two parallel paths; one is the stomatal resistance with its associated mesophyll resistance, and the other is non-stomatal resistance. The non-stomatal resistance is further decomposed into resistance to soil uptake, which includes the in-canopy aerodynamic resistance and the subsequent soil resistance, as well as resistance to cuticle uptake.

According to the scheme, the non-stomatal resistance for gas species i, r_{nsi}, is parameterized by combining those for O_3 and SO_2 with the scaling factors of α_i and β_i:

$$r_{nsi}^{-1} = \alpha_i / r_{nsSO_2}^{-1} + \beta_i / r_{nsO_3}^{-1}, \tag{A2}$$

where α_i and β_i represent the solubility and half-redox reactivity for species i, respectively. We rely on the equation to calculate dry deposition of gaseous ^{131}I by determining appropriate values for α_i and β_i for the non-stomatal resistance in the following way. The behavior of ^{131}I in the atmosphere is complicated because it is either bound to particles (aerosols) or in gaseous form. Unfortunately there are no data available of the chemical analysis of gaseous ^{131}I during FNPS1 accident, therefore we focus on two species of elemental (I_2) and organic forms (CH_3I) which have been known to be dominant in past nuclear accidents (Baklanov and Sørensen, 2001). The former gas is more reactive than the latter probably due to a larger reactivity and solubility. The ob-

servational results summarized in Sehmel (1980) also suggest that deposition velocity for I_2 (V_{dg} = 0.02–7.2 cm s^{-1}) are in the same range as SO_2 (V_{dg} = 0.04–7.5 cm s^{-1}) and more than ten times that of CH_3I (V_{dg} = 0.0001–0.01 cm s^{-1}). By considering this fact, we set the values of (α_i,β_i) = (1,0) and (0.01,0) for I_2 and CH_3I, respectively. The ratio of gaseous CH_3I to ^{131}I gas was assumed to be constant of 0.6 throughout the simulation period (US NRC, 2012) due to lack of field data.

A2 Dry deposition of particles

With regard to the calculation of the dry deposition for particles, the modified parameterization of Zhang et al. (2001) is implemented for V_d for particle V_{dp} in Eq. (A1) as described by Kajino et al. (2012). The original parameterization calculates deposition velocity of particles as a reciprocal of total transfer resistance in series of aerodynamic and surface resistances for each particle size bin. From this, the following modification is made based on more recent studies (Katata et al., 2008, 2011; Petroff and Zhang, 2010): (1) on the basis of the fact that forests can collect a large amount of sub-micron particles (Gallagher et al., 1997; Matsuda et al., 2010) caused by high turbulence over the canopy (e.g., Petroff et al., 2009), hygroscopic growth of particles under humid conditions (Katata et al., 2013), and other collection mechanisms, the empirical constant ε_0, which is inversely proportional to the surface resistance (Zhang et al., 2001), was set to 5 and 1 for the forest and short vegetation categories, respectively. (2) For the collection efficiency by leaves due to inertial impaction, the modified function of Peters and Eiden (1992) was used. (3) Collection efficiencies for vegetative surfaces due to interception and Brownian diffusion were modeled based on Kirsch and Fuchs (1968) and Fuchs (1964), respectively. (4) For the land use categories of desert, tundra, ice cap, glacier, inland water, and ocean, the surface resistance for non-vegetated surfaces proposed by Petroff and Zhang (2010) were adopted.

After these modifications, the dry deposition velocity calculated by the modified model better agreed with the observational data than did the original model of Zhang

et al. (2001). For example, the size-segregated V_d for a forest is 0.1–1 cm s^{-1} in the size range from 0.1–1 µm diameter and these values corresponded with the observations. For ground and water surfaces, good agreement was found between the modified model calculations and the observations from the literature, as shown in Petroff and Zhang (2010) (not shown in the figure). For the calculation of V_{dp}, a single log-normal size distribution is assumed for all radioactive particles. The mean mass equivalent particle diameters are set to 0.5 and 1.5 µm for ^{131}I and other radionuclides, respectively, based on the observational results at JAEA-Tokai from 17 March to 1 April (Miyamoto et al., 2014) with a geometric standard deviation of 1.6 µm (Kaneyasu et al., 2012).

Figure A1 illustrates the dry deposition velocity of ^{131}I, gaseous I_2 and CH_3I, and particulate ^{131}I and ^{137}Cs (expecting the chemical form of CsI) for grassland and forest against the horizontal wind speed for a typical clear period during the accident. Generally, the deposition velocity for particles is larger over the forest than over short vegetation as explained above. However, for gases the deposition velocities over the two vegetation types do not show a large difference because stomata resistance is dominant rather than aerodynamic resistance. Atmospheric stability significantly decrease the nighttime V_d under low wind speed condition < 5 m s^{-1} (Fig. A1b). Consequently, the modeled dry deposition velocity of I_2, CH_3I, particulate iodine, and other particles can vary in the range of 0.001–0.5 cm s^{-1}, 0.0004–0.001 cm s^{-1}, 0.005–0.1 cm s^{-1}, and 0.02–0.3 cm s^{-1} over short vegetation. The deposition velocity of ^{131}I depends on the chemical composition, and has values from 0.003–0.2 cm s^{-1}. For example I_2 : CH_3I : particulateI = 2 : 3 : 5 based on the measurement of gaseous and particulate ^{131}I concentration at JAEA-Tokai on 15 March 2011. It should be noted that the original WSPEEDI-II used constant values of V_d of 0.3 and 0.1 cm s^{-1} for ^{131}I and ^{137}Cs, respectively, which are similar to daytime values calculated by the modified scheme.

During the FNPS1 accident, a few studies have reported the V_d for ^{131}I and ^{137}Cs calculated by the data of deposition flux and air concentration measured by bulk samplers and combined samplers of the dust filter and charcoal cartridge, respectively. Amano et al. (2012) showed that daily mean values of V_d were from 0.1–0.2 cm s^{-1}

and 0.2–0.3 cm s^{-1} for ^{131}I and ^{137}Cs, respectively, at Chiba Prefecture from 14–17 March. Takeyasu and Sumiya (2014) used the daily fallout data sampled at JAEA-Tokai in Ibaraki Prefecture, and estimated the similar values of V_d of both radionuclides as 0.26 cm s^{-1} and 0.43 cm s^{-1} in 15–16 March, respectively. Those results indicate that the modified dry deposition scheme is reasonable.

A3 In-cloud scavenging

Previously wet deposition has been treated in WSPEEDI-II by a simple exponential function between the scavenging coefficient (Λ) and precipitation intensity (P_r) without separation of chemical forms as some other dispersion models (Table 1). We modify the scheme to be more mechanistic based on the in-cloud scavenging parameterization of Giorgi and Chameides (1986) for highly hygroscopic aerosols and soluble gases. Furthermore, the effects of gas solubility, aerosol hygroscopicity, and ice phase cloud microphysics are also considered in the scheme. The new equation for Λ due to nucleation (in-cloud) scavenging for non-convective clouds, which considers the chemical forms of radionuclides, height dependency, aerosol activation, and ice phase, is expressed as:

$$\Lambda(z) = \frac{F}{\Delta t}[1 - \exp(-b\Delta t)] f_{\mathrm{ccn}}(z) f_{\mathrm{ice}}(z) f_{q_c}(z), \tag{A3}$$

$$F = \frac{F_0}{1 + b_0 \tau}, \tag{A4}$$

$$b = \frac{b_0 + \tau^{-1}}{F_0}, \tag{A5}$$

where z is the height, f_{q_c} is the fraction of liquid water content of cloud droplet (q_c) at each height to q_c accumulated throughout the cloud layer, τ is the washout time of clouds, and F_0 and b_0 are the parameters given as 0.8 and 10^{-4}, respectively (Giorgi and Chameides, 1986). f_{ccn} and f_{ice} in Eq. (A3) are the fraction of the CCN activated

aerosols forming the cloud droplets and the accretion efficiency of the cloud droplets by settling ice crystals, respectively, which are described later. It should be noted that $f_{\mathrm{ccn}} = 1$ for gaseous iodine.

The washout time for gases and aerosols in the accumulation mode, τ, represents the amount of time required to remove aerosols or gases dissolved into all of the water from the cloud layer at the specified precipitation rate, P_r (Byun and Schere, 2006), and is given by

$$\tau = \frac{\overline{W}_{q_c}}{\rho_w P_r}(1 + \gamma), \tag{A6}$$

$$\gamma = \begin{cases} 0 & \text{(particles)} \\ \frac{\rho_w}{H_i^* \overline{W}_{q_c} RT} & \text{(gases)} \end{cases}, \tag{A7}$$

where $\overline{W}_{q_c}$ is the vertically averaged total (i.e., cloud + rainwater) liquid water content, ρ_w is the density of liquid water, R is the universal gas constant, T is the in-cloud air temperature, and H_i^* is the effective Henry's constant for gas species i. H_i^* is calculated for gaseous ^{131}I using input data of I^- concentration in rainwater of 3×10^{-9} mol L^{-3} (Gilfedder et al., 2008) and a typical value of rainwater pH = 5 observed in Eastern Japan (Ministry of the Environment of Japan, 2010), resulting in H_i^* of approximately 55 and 0.23 for I_2 and CH_3I, respectively.

The modeled scavenging coefficient (Λ) for particle and gas is depicted in Fig. A2. It is shown that for particles Λ decreases with an increase of cloud liquid water content ($\overline{W}_{q_c}$) with constant precipitation rate (P_r) according to Eqs. (A3)–(A5) because Λ is a function of a reciprocal of τ represented as Eq. (A6). This means that less scavenged water is created in the atmosphere when $\overline{W}_{q_c}$ is small. For I_2 and CH_3I gases, γ becomes large compared with that of particle (Eq. A7) because it takes longer for the cloud droplets to dissolve less soluble gases. This increases the removal time of clouds (Eq. A6), resulting in a lower scavenging coefficient. The original WSPEEDI-II

has $\Lambda = 10^{-5}$–$10^{-4}\,s^{-1}$ empirically determined from field measurement data of Λ by Brenk and Vogt (1981). This value is consistent with the calculation result of the modified scheme of Eq. (A3) when cloud liquid water content is high. For low cloud water content ($< 1\,g\,m^{-3}$), Λ becomes large up to $10^{-1}\,s^{-1}$ in the new scheme. In the FNPS1 accident, for example, calculated values of Λ in the areas of Naka-Dori and Tochigi and Gunma Prefectures in the WSPEEDI simulation were ranged from 10^{-4}–$10^{-3}\,s^{-1}$ when the plume passed through there in the afternoon on 15 March (Fig. S5). This result is reasonable when compared with many observational studies for light and moderate rain events in various areas including Japan (Jylhä, 1991; Okita et al., 1996; Minoura and Iwasaka, 1997; Laakso et al., 2003; Andronache, 2004; Zhang et al., 2013). A few studies also reported very high values of $\Lambda > 10^{-3}\,s^{-1}$ for cosmogenic radionuclides (Davis, 1972) and of $\Lambda = 0.2\,s^{-1}$ for cloud droplets in 5–60 µm diameter range (Levine and Schwartz, 1982).

The Λ for particle is two orders of magnitude higher than that of I_2 gas due to the effect of gas solubility modeled in Eqs. (A6) and (A7). In the same manner, the Λ for CH_3I gas has very small values in the range of 10^{-10}–$10^{-8}\,s^{-1}$ due to its very low Henry's constant. The tendency for gases to have lower Λ than particles is supported by the observational studiy of Brenk and Vogt (1981).

A4 Cloud condensation nuclei (CCN) activation

For calculating f_{ccn}, the CCN activation and subsequent cloud microphysical processes were parameterized using Abdul-Razzak and Ghan (2000) and Lin et al. (1983). When the Abdul-Razzak and Ghan (2000) parameterization predicts that CCN activation occurs in a grid cell, the portions of the mass (calculated based on the predicted critical diameters and prescribed log-normal size distribution parameters of radioactive aerosols) were transferred to the grid-scale cloud droplets (f_{ccn}). Lin et al. (1983) developed an explicit cloud microphysics model describing the interactions between cloud droplets and other hydrometers, such as rain, snow and graupel droplets. The autocon-

version rate (cloud → rain) and the accretion rate of cloud droplets by rain, snow, and graupel (cloud → rain, cloud → snow, cloud → graupel), predicted by Lin et al. (1983), were used to calculate the transfer of the aerosol moments and mass in the cloud droplets to the other hydrometers. Subgrid scale scavenging is not considered here because the horizontal grid resolution is fine enough in the regional scale analysis (< 3 km) and, in addition, the subgrid scale convection should not be strong during the cold season. In the above CCN activation scheme, the following size distribution parameters are adopted. Number equivalent geometric mean dry diameter was set to 100 nm with geometric standard deviation of 1.6 (Adachi et al., 2013). The aerosol hygroscopicity $\kappa = 0.4$ was assumed based on an internal mixture of sulfate and organics (Petters and Kreidensweis, 2007), which is consistent with the activity (mass) equivalent wet particle diameter obtained by Kaneyasu et al. (2012) under the typical meteorological conditions during the cold season in Japan. Figure A2b shows the sensitivity of CCN activation fraction, f_{ccn}, to vertical wind velocity. As shown in the figure, the value of f_{ccn} rapidly increases with an increase of vertical wind speed, and ambient aerosols become almost completely activated when the vertical wind speed exceeds $0.1\,m\,s^{-1}$.

A5 Scavenging by settling ice crystals

To include the difference in the scavenging coefficient between liquid (rain) and ice phases (snow and graupel), f_{ice} in Eq. (A3) the accretion rates are used for both phases from the cloud microphysics model of Lin et al. (1983). First, the accretion rate from cloud to the mixture of rain, snow, and graupel is calculated at each atmospheric layer. Then, the accretion rate of cloud droplets by rain is computed by assuming all the snow and graupel water are rain water. Finally, f_{ice} is determined by dividing the former accretion ratio for the mixture of rain, snow, and graupel by the latter for rain, which is considered to represent the scavenging velocity of cloud-borne aerosols by settling ice crystals. The accretion of cloud droplets by cloud ice particles is neglected in the study because the gravitational settling velocity is very small (Morrison et al., 2005).

During the FNPS1 accident, the modeling approach using f_{ice} increased the snowfall Λ up to three times greter than the rainfall Λ in the areas where the concentration of radionuclides was high (Fig. 27c and e) due to higher accretion rate of cloud droplets by ice crystals than that of raindrops. This is consistent with the experimental (Wolf and Dana, 1969; Graedel and Franey, 1975; Sparmacher et al., 1993; Kyrö et al., 2009; Paramonov et al., 2011) and modeling studies of snow scavenging of aerosols with 1 µm in mass-equivalent diameter (Stier et al., 2005; Croft et al., 2009; Zhang et al., 2013). However, some modeling studies reported a lower scavenging rate for snow crystals (Maryon and Ryall, 1996; Hongisto, 1998) than rain drops. This difference may be caused by a large variety in collection efficiency of cloud droplets by snow crystals (Sauter and Wang, 1989; Mircea and Stefan, 1998) which depends upon the size and shape of ice crystals and the ambient humidity (Miller and Wang, 1991; Feng, 2009; Wang et al., 2010).

A6 Below-cloud scavenging

The aerosol–hydrometeor coagulation (below-cloud) scavenging of raindrops and settling ice crystals is not considered in the study because for accumulation mode aerosol particles it is very small when compared with the nucleation scavenging rate for low and moderate rainfall rates of 0.1–10 mm h^{-1} (Andronache, 2003; Henzing et al., 2006; Zhang et al., 2013; Oshima et al., 2013).

A7 Fogwater deposition

Fogwater deposition is the phenomenon that transports radionuclides in water droplets of fog or low-cloud downward toward the ground by turbulence, and eventually these droplets are intercepted by the plant canopies (Lovett, 1984). Although the potential effect of this process has been suggested in prior work (Baklanov and Sørensen, 2001), modeling of fogwater deposition is not done yet in any of the existing dispersion models (Table 1). This study introduces a simple and accurate Fog Deposition EStimation

(FogDES) scheme for meteorological models (Katata et al., 2011a; Katata, 2014). In general, fogwater deposition can be also calculated with Eq. (A1), using the concentration of radionuclides in cloud liquid water in the lowest atmospheric layer. To simplify, radionuclides are assumed to be completely absorbed by fogwater. Only the parameter of V_d is required to calculate the fogwater deposition flux. In FogDES scheme, V_d for fogwater (V_{df}) can be parameterized as a linear function of the horizontal wind speed and vegetation parameters:

$$V_{df} = R_{LUC} A_c U, \tag{A8}$$

$$A_c = \begin{cases} 0.0164(\mathrm{LAI}/h)^{-0.5} \\ 0.0095\mathrm{LAI}^3 - 0.05\mathrm{LAI}^2 + 0.0916\mathrm{LAI} + 0.0082 \end{cases}, \tag{A9}$$

where LAI is the leaf area index, h is the canopy height, R_{LUC} is the ratio of V_{df} for each landuse category (LUC) of MM5 to that for coniferous forest (i.e., $R_{LUC} = 1$ for coniferous forest). The A_c value was set to be constant (0.0248) as determined at a dense mountainous forest in Germany (Katata et al., 2008) due to lack of accurate data of vegetation parameters (LAI and h) in the study area. By considering a relatively small V_{df} for short vegetation compared with tall vegetation (e.g., Gallagher et al., 1988), the value of 1, 0.2, and 0.1 were applied to R_{LUC} for forest, short vegetation (such as crop- and grassland), and smooth surface (such as water bodies and bare soil).

The deposition velocity due to fogwater is plotted against wind speed in Fig. A1. The calculations are in the range of the observation data ranging from 2–8 cm s^{-1} and 1–100 cm s^{-1} over short vegetation (e.g., Gallagher et al., 1988; Thalmann et al., 2002) and dense closed forest (e.g., Dasch, 1988; Klemm and Wrzesinsky, 2007; Eugster et al., 2006) as reviewed in Katata (2014). Importantly, the figure also shows the relatively large impacts of fogwater deposition to total deposition compared with dry deposition because the fog droplets are larger than submicron aerosols and have a higher impaction efficiency to plant leaves.

The Supplement related to this article is available online at doi:10.5194/acpd-14-14725-2014-supplement.

Acknowledgements. The authors express their gratitude to Fumiya Tanabe and Yu Maruyama for their helpful comments and suggestions. Foster Kevin, Lawrence Livermore National Laboratory, Livermore (LLNL) of the USA, provided the digital data of air dose rate by US-DOE airborne monitoring. The source terms of Hirao et al. (2013) and Winiarek et al. (2014) were provided by Shigekazu Hirao, Nagoya University in Japan and Victor Winiarek, Centre d'Enseignement et de Recherche en Environnement Atmosphérique (CEREA) in France, respectively. Calculation results of WRF-CMAQ were provided by Yu Morino, National Institute for Environmental Studies (NIES) in Japan. This study was partly supported by a Postdoctoral Fellowship for Research Abroad, No. 22865, provided by the Japan Society for the Promotion of Science (JSPS).

References

Abdul-Razzak, H. and Ghan, S. J.: A parameterization of aerosol activation. 2. Multiple aerosol types, J. Geophys. Res., 105, 6837–6844, 2000.

Achim, P., Monfort, M., Le Petit, G., Gross, P., Douysset, G., Taffary, T., Blanchard, X., and Moulin, C.: Analysis of radionuclide releases from the Fukushima Dai-ichi Nuclear Power Plant Accident Part II, Pure Appl. Geophys., 171, 645–667, 2014.

Adachi, K., Kajino, M., Zaizen, Y., and Igarashi, Y.: Emission of spherical cesium-bearing particles from an early stage of the Fukushima nuclear accident, Sci. Rep., 3, 2554, doi:10.1038/srep02554, 2013.

Amano, H., Akiyama, M., Chunlei, B., Kawamura, T., Kishimoto, T., Kuroda, T., Muroi, T., Odaira, T., Ohta, Y., Takeda, K., Watanabe, Y., and Morimoto, T.: Radiation measurements in the Chiba Metropolitan Area and radiological aspects of fallout from the Fukushima Dai-ichi Nuclear Power Plants accident, J. Environ. Radioactiv., 111, 42–52, 2012.

Andronache, C.: Estimated variability of below-cloud aerosol removal by rainfall for observed aerosol size distributions, Atmos. Chem. Phys., 3, 131–143, doi:10.5194/acp-3-131-2003, 2003.

Andronache, C.: Estimates of sulfate aerosol wet scavenging coefficient for locations in the Eastern United States, Atmos. Environ., 38, 795–804, 2004.

Aoyama, M., Tsumune, D., and Hamajima, Y.: Distribution of ^{137}Cs and ^{134}Cs in the North Pacific Ocean: impacts of the TEPCO Fukushima-Daiichi NPP accident, J. Radioanal. Nucl. Ch., 296, 535–539, 2012.

Baklanov, A. and Sørensen, J. H.: Parameterisation of radionuclide deposition in atmospheric long-range transport modelling, Phys. Chem. Earth, 26, 787–799, 2001.

Brenk, H. D. and Vogt, K. J., The calculation of wet deposition from radioactive plumes, Nucl. Safety, 22, 362–371, 1981.

Byun, D. and Schere, K. L.: Review of the governing equations, computational algorithms, and other components of the models-3 Community Multiscale Air Quality (CMAQ) modeling system, Appl. Mech. Rev., 59, 1–6, 2006.

Chino, M., Nakayama, H., Nagai, H., Terada, H., Katata, G., and Yamazawa, H.: Preliminary estimation of release amounts of ^{131}I and ^{137}Cs accidentally discharged from the Fukushima Daiichi nuclear power plant into atmosphere, J. Nucl. Sci. Technol., 48, 1129–1134, 2011.

Christoudias, T. and Lelieveld, J.: Modelling the global atmospheric transport and deposition of radionuclides from the Fukushima Dai-ichi nuclear accident, Atmos. Chem. Phys., 13, 1425–1438, doi:10.5194/acp-13-1425-2013, 2013.

Comprehensive Nuclear-Test-Ban Treaty Organization, Preparatory Commission (CTBTO): Fukushima-related Measurements by CTBTO, available at: http://www.ctbto.org/press-centre/highlights/2011/fukushima-related-measurements-by-the-ctbto (last access: 25 April 2014), 2011.

Croft, B., Lohmann, U., Martin, R. V., Stier, P., Wurzler, S., Feichter, J., Posselt, R., and Ferrachat, S.: Aerosol size-dependent below-cloud scavenging by rain and snow in the ECHAM5-HAM, Atmos. Chem. Phys., 9, 4653–4675, doi:10.5194/acp-9-4653-2009, 2009.

D'Amours, R., Malo, A., Servranckx, R., Bensimon, D., Trudel, S., and Gauthier, J.-P.: Application of the atmospheric Lagrangian particle dispersion model MLDP0 to the 2008 eruptions of Okmok and Kasatochi volcanoes, J. Geophys. Res., 115, D00L11, doi:10.1029/2009JD013602, 2010.

Dasch, M. J.: Hydrological and chemical inputs to fir trees from rain and clouds during a 1-month study at Clingmans Peak, NC, Atmos. Environ., 22, 2255–2262, 1988.

Davis, W. E.: A model for in-cloud scavenging of cosmogenic radionuclides, J. Geophys. Res., 77, 2159–2165, 1972.

Draxler, R. R.: The use of global and mesoscale meteorological model data to predict the transport and dispersion of tracer plumes over Washington, DC, Weather Forecast., 21, 383–394, 2006.

Draxler, R. R. and Rolph, G. D.: Evaluation of the transfer coefficient matrix (TCM) approach to model the atmospheric radionuclide air concentrations from Fukushima, J. Geophys. Res., 117, D05107, doi:10.1029/2011JD017205, 2012.

Draxler, R., Arnold, D., Chino, M., Galmarini, S., Hort, M., Jones, A., Leadbetter, S., Malo, A., Maurer, C., Rolph, G., Saito, K., Servranckx, R., Shimbori, T., Solazzo, E., and Wotawa, G.: World Meteorological Organization's model simulations of the radionuclide dispersion and deposition from the Fukushima Daiichi Nuclear Power Plant accident, J. Environ. Radioactiv., in press, doi:10.1016/j.jenvrad.2013.09.014, 2014.

Dvorzhak, A., Puras, C., and Montero, M.: Spanish experience on modeling of environmental radioactive contamination due to Fukushima Daiichi NPP Accident using JRODOS, Environ. Sci. Technol., 46, 11887–11895, 2012.

Eugster, W., Burkard, R., Holwerda, F., Scatena, F. N., and Bruijnzeel, L. A.: Characteristics of fog and fogwater fluxes in a Puerto Rican elfin cloud forest, Agr. Forest Meteorol., 139, 288–306, 2006.

Evangeliou, N., Balkanski, Y., Cozic, A., and Moller, A. P.: Global transport and deposition of Cs-137 following the Fukushima Nuclear Power Plant Accident in Japan: emphasis on Europe and Asia using high-resolution model versions and radiological impact assessment of the human population and the environment using interactive tools, Environ. Sci. Technol., 47, 5803–5812, 2013.

Feng, J.: A size-resolved model for below-cloud scavenging of aerosols by snowfall, J. Geophys. Res., 114, D08203, doi:10.1029/2008JD011012, 2009.

Fuchs, N. A.: The Mechanics of Aerosols, Pergamon Press, Oxford, 1964.

Fukushima Prefecture: Results of environmental radioactivity monitoring around 20 km–50 km zone, available at: http://www.pref.fukushima.jp/j/20-50km0315-0331.pdf (last access: 25 April 2014), 2011a (in Japanese).

Fukushima Prefecture: Results of environmental radioactivity monitoring in Fukushima Prefecture, available at: http://www.pref.fukushima.jp/j/7houbu0311-0331.pdf (last access: 25 April 2014), 2011b (in Japanese).

Fukushima Prefecture: Results of air dose rate measurement on March 2011 (data retrieved from monitoring posts in Fukushima Prefecture), available at: http://www.

atom-moc.pref.fukushima.jp/monitoring/monitoring201103/201103_mpdata.html (last access: 25 April 2014), 2012 (in Japanese).

Furuno, A., Terada, H., Chino, M., and Yamazawa, H.: Experimental verification for real-time environmental emergency response system: WSPEEDI by European tracer experiment, Atmos. Environ., 38, 6989–6998, 2004.

Furuta, S., Sumiya, S., Watanabe, H., Nakano, M., Imaizumi, K., Takeyasu, M., Nakada, A., Fujita, H., Mizutani, T., Morisawa, M., Kokubun, Y., Kono, T., Nagaoka, M., Yokoyama, H., Hokama, T., Isozaki, T., Nemoto, M., Hiyama, Y., Onuma, T., Kato, C., and Kurachi, T.: Results of the environmental radiation monitoring following the accident at the Fukushima Daiichi Nuclear Power Plant; Interim report (Ambient radiation dose rate, radioactivity concentration in the air and radioactivity concentration in the fallout), JAEA-Review 2011-035, Japan Atomic Energy Agency, Ibaraki, Japan, 2011 (in Japanese with English abstract).

Gallagher, M. W., Choularton, T. W., Morse, A. P., and Fowler, D.: Measurements of the size dependence of cloud droplet deposition at a hill site, Q. J. Roy. Meteor. Soc., 114, 1291–1303, 1988.

Gallagher, M. W., Beswick, K. M., Choularton, T. W., Duyzer, J., Westrate, H., and Hummelshøj, P.: Measurements of aerosol fluxes to speulder forest using a micrometeorological technique, Atmos. Environ., 31, 359–373, 1997.

Gilfedder, B. S., Lai, S. C., Petri, M., Biester, H., and Hoffmann, T.: Iodine speciation in rain, snow and aerosols, Atmos. Chem. Phys., 8, 6069–6084, doi:10.5194/acp-8-6069-2008, 2008.

Giorgi, F. and Chameides, W. L.: Rainout lifetimes of highly soluble aerosols and gases inferred from simulations with a general circulation model, J. Geophys. Res., 91, 14367–14376, 1986.

Graedel, T. E. and Franey, J. P.: Field measurements of submicron aerosol washout by snow, Geophys. Res. Lett., 2, 325–328, 1975.

Grell, G. A., Dudhia, J., and Stauffer, D. R.: A Description of the Fifth-generation Penn State/NCAR Mesoscale Model (MM5), NCAR Tech. Note NCAR/TN-3921STR, Boulder, CO, 122 pp., 1994.

Haba, H., Kaneya, J., Mukai, H., Kambara, T., and Kase, M.: One-year monitoring of airborne radionuclides in Wako, Japan, after the Fukushima Dai-ichi nuclear power plant accident in 2011, Geochem. J., 46, 271–278, 2012.

HCRM (Health Canada's Radiation Monitoring): Health Canada's Radiation Monitoring (HCRM) Data and the Nuclear Emergency in Japan, the CTBTO data for Canadian stations, http://www.hc-sc.gc.ca/hc-ps/ed-ud/respond/nuclea/data-donnees-eng.php (last access: 25 April 2014), 2011.

Henzing, J. S., Olivié, D. J. L., and van Velthoven, P. F. J.: A parameterization of size resolved below cloud scavenging of aerosols by rain, Atmos. Chem. Phys., 6, 3363–3375, doi:10.5194/acp-6-3363-2006, 2006.

Hertel, O., Christensen, J., Runge, E. H., Asman, W. A. H., Berkowicz, R., Hovmand, M. F., and Hov, Ø.: Development and testing of a new variable scale air pollution model – ACDEP, Atmos. Environ., 29, 1267–1290, 1995.

Hicks, B. B., Baldocchi, D. D., Meyers, T. P., Hosker, R. P., and Matt, D. R.: A preliminary multiple resistance routine for deriving dry deposition velocities from measured quantities, Water Air Soil Poll., 36, 311–330, 1987.

Hirao, S., Yamazawa, H.; Nagae, T.: Estimation of release rate of iodine-131 and cesium-137 from the Fukushima Daiichi nuclear power plant, J. Nucl. Sci. Technol., 50, 139–147, 2013.

Honda, M. C., Aono, T., Aoyama, M., Hamajima, Y., Kawakami, H., Kitamura, M., Masumoto, Y., Miyazawa, Y., Takigawa, M., and Saino, T.: Dispersion of artificial caesium-134 and -137 in the western North Pacific one month after the Fukushima accident, Geochem. J., 46, E1–E9, 2012.

Hongisto, M.: HILATAR, a Regional Scale Grid Model for the Transport of Sulphur and Nitrogen Compounds, Description of the Model and Simulation Results for the Year 1993, Finnish Meteorological Institute, Helsinki, No. 21, 1998.

Ibaraki Prefecture: Radiation Dose Measurements in Ibaraki Prefecture, available at: http://www.pref.ibaraki.jp/20110311eq/radiation.html (last access: 25 April 2014), 2011 (in Japanese).

Jacobson, M. Z.: Fundamentals of Atmospheric Modeling, Cambridge University Press, Cambridge, 828 pp., 2005.

Jones, A. R., Thomson, D. J., Hort, M. C., and Devenish, B.: The UK Met Office's next-generation atmospheric dispersion model, NAME III, in: Air Pollution and its Applications XVII, edited by: Borrego, C. and Norman, A. L., Proceedings of the 27th NATO/CCMS International Technical Meeting on Air Pollution Modelling and its Application, Springer, 580–589, 2007.

Jylhä, K.: Empirical scavenging coefficients of radioactive substances released from chernobyl, Atmos. Environ., 25, 263–270, 1991.

Kajino, M., Inomata, Y., Sato, K., Ueda, H., Han, Z., An, J., Katata, G., Deushi, M., Maki, T., Oshima, N., Kurokawa, J., Ohara, T., Takami, A., and Hatakeyama, S.: Development of the RAQM2 aerosol chemical transport model and predictions of the Northeast Asian aerosol mass, size, chemistry, and mixing type, Atmos. Chem. Phys., 12, 11833–11856, doi:10.5194/acp-12-11833-2012, 2012.

Kaneyasu, N., Ohashi, H., Suzuki, F., Okuda, T., and Ikemori, F.: Sulfate aerosol as a potential transport medium of radiocesium from the Fukushima nuclear accident, Environ. Sci. Technol., 46, 5720–5726, 2012.

Katata, G.: Fogwater deposition modeling for terrestrial ecosystems: a review of developments and measurements, J. Geophys. Res., in review, 2014.

Katata, G., Kajino, M., Hiraki, T., Aikawa, M., Kobayashi, T., and Nagai, H.: A method for simple and accurate estimation of fog deposition in a mountain forest using a meteorological model, J. Geophys. Res., 116, D20102, doi:10.1029/2010JD015552, 2011a.

Katata, G., Nagai, H., Zhang, L., Held, A., Serça, D., and Klemm, O.: Development of an atmosphere–soil–vegetation model for investigation of radioactive materials transport in the terrestrial biosphere, Prog. Nucl. Sci. Technol., 2, 530–537, 2011b.

Katata, G., Nagai, H., Wrzesinsky, T., Klemm, O., Eugster, W., and Burkard, R.: Development of a land surface model including cloud water deposition on vegetation, J. Appl. Meteorol.Climatol., 47, 2129–2146, 2008.

Katata, G., Terada, H., Nagai, H., and Chino, M.: Numerical reconstruction of high dose rate zones due to the Fukushima Daiichi Nuclear Power Plant accident, J. Environ. Radioact., 111, 2–12, 2012a.

Katata, G., Ota, M., Terada, H., Chino, M., and Nagai, H.: Atmospheric discharge and dispersion of radionuclides during the Fukushima Dai-ichi Nuclear Power Plant accident, Part I: Source term estimation and local-scale atmospheric dispersion in early phase of the accident, J. Environ. Radioactiv., 109, 103–113, 2012b.

Katata, G., Kajino, M., Matsuda, K., Takahashi, A., and Nakaya, K.: A numerical study of the effects of aerosol hygroscopic properties to dry deposition on a broad-leaved forest, Atmos. Environ., doi:10.1016/j.atmosenv.2013.11.028, in press, 2014.

Kawamura, H., Kobayashi, T., Furuno, A., Usui, N., and Kamachi, M.: Numerical simulation on the long-term variation of radioactive cesium concentration in the North Pacific due to the Fukushima disaster, J. Environ. Radioactiv., in review, 2014.
KEK (High Energy Accelerator Research Organization): Radiation monitoring at KEK, available at: http://legacy.kek.jp/quake/radmonitor/index-e.html (last access: 25 April 2014), 2011.
Kerkweg, A., Buchholz, J., Ganzeveld, L., Pozzer, A., Tost, H., and Jöckel, P.: Technical Note: An implementation of the dry removal processes DRY DEPosition and SEDImentation in the Modular Earth Submodel System (MESSy), Atmos. Chem. Phys., 6, 4617–4632, doi:10.5194/acp-6-4617-2006, 2006.
Kirsch, A. A. and Fuchs, N. A.: Studies on fibrous aerosol filters. III. Diffusional deposition of aerosols in fibrous filters, Ann. Occup. Hyg., 11, 299–304, 1968.
Klemm, O. and Wrzesinsky, T.: Fog deposition fluxes of water and ions to a mountainous site in Central Europe, Tellus B, 59, 705–714, 2007.
Kobayashi, T., Otosaka, S., Togawa, O., and Hayashi, K.: Development of a non-conservative radionuclides dispersion model in the ocean and its application to surface cesium-137 dispersion in the Irish Sea, J. Nucl. Sci. Technol., 44, 238–247, 2007.
Kobayashi, T., Nagai, H., Chino, M., and Kawamura, H.: Source term estimation of atmospheric release due to the Fukushima Dai-ichi Nuclear Power Plant accident by atmospheric and oceanic dispersion simulations, J. Nucl. Sci. Technol., 50, 255–264, 2013.
Korsakissok, I., Mathieu, A., and Didier, D.: Atmospheric dispersion and ground deposition induced by the Fukushima Nuclear Power Plant accident: a local-scale simulation and sensitivity study, Atmos. Environ., 70, 267–279, 2013.
Kyrö, E. M., Grönholm, T., Vuollekoski, H., Virkkula, A., Kulmala, M., and Laakso, L.: Snow scavenging of ultrafine particles: field measurements and parameterization, Boreal Environ. Res., 14, 527–538, 2009.
Laakso, L., Grönholm, T., Rannik, U., Kosmale, M., Fiedler, V., Vehkamäki, H., and Kulmala, M.: Ultrafine particle scavenging coefficients calculated from 6 years field measurements, Atmos. Environ., 37, 3605–3613, 2003.
Leadbetter, S., Hort, M., Jones, A., Webster, H., and Draxler, R.: Sensitivity of the modeled deposition of Caesium-137 from the Fukushima Dai-ichi nuclear power plant to the wet deposition parameterization in NAME, doi:10.1016/j.atmosenv.2014.03.018, in press, 2014.
Levine, S. Z. and Schwartz, S. E.: In-cloud and below-cloud scavenging of Nitric acid vapor, Atmos. Environ., 16, 1725–1734, 1982.

Lin, Y.-L., Richard, D. F., and Harold, D. O.: Bulk parameterization of the snow field in a cloud model, J. Clim. Appl. Meteorol., 22, 1065–1092, 1983.
Lovett, G. M.: Rates and mechanisms of cloud water deposition to a subalpine balsam fir forest, Atmos. Environ., 18, 361–371, 1984.
Masson, O., Baeza, A., Bieringer, J., Brudecki, K., Bucci, S., Cappai, M., Carvalho, F. P., Connan, O., Cosma, C., Dalheimer, A., Didier, D., Depuydt, G., De Geer, L. E., De Vismes, A., Gini, L., Groppi, F., Gudnason, K., Gurriaran, R., Hainz, D., Halldorsson, O., Hammond, D., Hanley, O., Holey, K., Zs Homoki,., Ioannidou, A., Isajenko, K., Jankovic, M., Katzlberger, C., Kettunen, M., Kierepko, R., Kontro, R., Kwakman, P. J. M., Lecomte, M., Leon Vintro, L., Leppänen, A.-P., Lind, B., Lujaniene, G., Mc Ginnity, P., Mc Mahon, C., Mala, H., Manenti, S., Manolopoulou, M., Mattila, A., Mauring, A., Mietelski, J. W., Moller, B., Nielsen, S. P., Nikolic, J., Overwater, R. M. W., Palsson, S. E., Papastefanou, C., Penev, I., Pham, M. K., Povinec, P. P., Ramebäck, H., Reis, M. C., Ringer, W., Rodriguez, A., Rulik, P., Saey, P. R. J., Samsonov, V., Schlosser, C., Sgorbati, G., Silobritiene, B. V., Söderström, C., Sogni, R., Solier, L., Sonck, M., Steinhauser, G., Steinkopff, T., Steinmann, P., Stoulos, S., Sykora, I., Todorovic, D., Tooloutalaie, N., Tositti, L., Tschiersch, J., Ugron, A., Vagena, E., Vargas, A., Wershofen, H., and Zhukova, O.: Tracking of airborne radionuclides from the damaged Fukushima Dai-Ichi nuclear reactors by European Networks, Environ. Sci. Technol., 45, 7670–7677, 2011.
Masuda, S., Awaji, T., Sugiura, N., Toyoda, T., Ishikawa, Y., and Horiuchi, K.: Interannual variability of temperature inversions in the subarctic North Pacific, Geophys. Res. Lett., 33, L24610, doi:10.1029/2006GL027865, 2006.
Matsuda, K., Fujimura, Y., Hayashi, K., Takahashi, A., and Nakaya, K.: Deposition velocity of $PM_{2.5}$ sulfate in the summer above a deciduous forest in central Japan, Atmos. Environ., 44, 4582–4587, 2010.
Maryon, R. H. and Ryall, D. B.: Developments to the UK Nuclear Accident Response Model (NAME), Department of Environment, UK Met. Office, DoE Report # DOE/RAS/96.011, London, UK, 1996.
Mathieu, A., Korsakissok, I., Quélo, D., Groëll, J., Tombette, M., Didier, D., Quentric, E., Saunier, O., Benoit, J.-P., and Isnard, O.: Atmospheric dispersion and deposition of radionuclides from the Fukushima Daiichi nuclear power plant accident, Elements, 8, 195–200, 2012.

METI (Ministry of Economy, Trade and Industry), available at: http://www.meti.go.jp/press/2011/06/20110603019/20110603019.html (last access: 25 April 2014), 2011a (in Japanese).
METI, available at: http://www.meti.go.jp/press/20110316001/20110316001-2.pdf (last access: 25 April 2014), 2011b (in Japanese).
Miller, C. T., Poirier Mcneill, M. M., and Mayer, A. S.: Dissolution of trapped nonaqueous phase liquids: mass transfer characteristics, Water Resour. Res., 26, 2783–2796, 1990.
Miller, N. L. and Wang, P. K.: Theoretical determination of the efficiency of aerosol particle collection by falling columnar ice crystals, J. Atmos. Sci., 46, 1656–1663, 1989.
Ministry of the Environment of Japan: Comprehensive summary report on acid deposition monitoring survey Phase 4, available at: http://db.cger.nies.go.jp/dataset/acidrain/ja/04/index.html (last access: 25 April 2014), 2010 (in Japanese).
Minoura, H. and Iwasaka, Y.: Ion concentration changes observed in drizzling rains, Atmos. Res., 45, 165–182, 2006.
Mircea, M. and Stefan, S.: A theoretical study of the microphysical parameterization of the scavenging coefficient as a function of precipitation type and rate, Atmos. Environ., 32, 2931–2938, 1998.
Miyamoto, Y., Yasuda, K., and Magara, M.: Size distribution of radioactive particles collected at Tokai, Japan 6 days after the nuclear accident, J. Environ. Radioactiv., 132, 1–7, 2014.
Morino, Y., Ohara, T., and Nishizawa, M.: Atmospheric behavior, deposition, and budget of radioactive materials from the Fukushima Daiichi nuclear power plant in March 2011, Geophys. Res. Lett., 38, L00G11, doi:10.1029/2011GL048689, 2011.
Morino, Y., Ohara, T., Watanabe, M., Hayashi, S., and Nishizawa, M.: Episode analysis of deposition of radiocesium from the Fukushima Daiichi nuclear power plant accident, Environ. Sci. Technol., 47, 2314–2322, 2013.
Morrison, H., Curry, J. A., and Khvorostyanov, V. I.: A new double-moment microphysics parameterization for application in cloud and climate models, Part I: Description, J. Atmos. Sci., 62, 1665–1677, 2005.
NOAA (National Oceanic and Atmospheric Administration): National Oceanic and Atmospheric Administration, Air Resources Laboratory, Fukushima Daiichi Nuclear Power Plant Transfer Coefficient Matrix, available at: http://ready.arl.noaa.gov/READY_fdnpp.php (last access: 25 April 2014), 2012.

NOAA: World Meteorological Organization (WMO) Atmospheric Dispersion Model Simulations of Fukushima Daiichi Accident, US National Oceanic and Atmospheric Administration, available at: http://ready.arl.noaa.gov/READY_fdnppwmo.php (last access: 25 April 2014), 2014.
Nishihara, K., Iwamoto, H., and Suyama, K.: Estimation of fuel compositions in Fukushima-Daiichi nuclear power plant, JAEA-Data/Code 2012-018, Japan Atomic Energy Agency, Ibaraki, Japan, 2012 (in Japanese with English abstract).
NRA (Nuclear Regulation Authority): Readings of Seawater and Dust Monitoring in Sea Area by MEXT (March 2011), available at: http://radioactivity.nsr.go.jp/en/list/259/list-201103.html (last access: 25 April 2014), 2011.
NRA: Results of the (i) Fifth Airborne Monitoring Survey and (ii) Airborne Monitoring Survey Outside 80 km from the Fukushima Dai-ichi NPP, available at: http://radioactivity.nsr.go.jp/en/contents/6000/5790/24/203_0928_14e.pdf (last accress: 25 April 2014), 2012a.
NRA: Readings of dust sampling (All Results for May 2011), available at: http://radioactivity.nsr.go.jp/en/contents/4000/3156/24/dustsampling_AllResultsforMay~2011.pdf (last access: 25 April 2014), 2012b.
Ohfuchi, W., Nakamura, H., Yoshioka, M. K., Enomoto, T., Takaya, K., Peng, X., Yamane, S., Nishimura, T., Kurihara, Y., and Ninomiya, K.: 10-km mesh meso-scale resolving simulations of the global atmosphere on the Earth Simulator: preliminary outcomes of AFES (AGCM for the Earth Simulator), J. Earth Simulator, 1, 8–34, 2004.
Ohkura, T., Oishi, T., Taki, M., Shibanuma, Y., Kikuchi, M., Akino, H., Kikuta, Y., Kawasaki, M., Saegusa, J., Tsutsumi, M., Ogose, H., Tamura, S., and Sawahata, T.: Emergency Monitoring of Environmental Radiation and Atmospheric Radionuclides at Nuclear Science Research Institute, JAEA Following the Accident of Fukushima Daiichi Nuclear Power Plant, JAEA-Data/Code 2012-01, Japan Atomic Energy Agency, Ibaraki, Japan, 2012 (in Japanese with English abstract).
Okita, T., Hara, H., and Fukuzaki, N.: Measurements of atmospheric SO_2 and SO_4^{2-}, and determination of the wet scavenging coefficient of sulfate aerosols for the winter monsoon season over the sea of Japan, Atmos. Environ., 30, 3733–3739, 1996.
Oshima, N., Koike, M., Kondo, Y., Nakamura, H., Moteki, N., Matsui, H., Takegawa, N., and Kita, K.: Vertical transport mechanisms of black carbon over East Asia in spring during the A-FORCE aircraft campaign, J. Geophys. Res., 118, 13175–13198, 2013.
Paramonov, M., Grönholm, T., and Virkkula, A.: Below-cloud scavenging of aerosol particles by snow at an urban site in Finland, Boreal Environ. Res., 16, 304–320, 2011.

Peters, K. and Eiden, R.: Modelling the dry deposition velocity of aerosol particles to a spruce forest, Atmos. Environ., 26A, 2555–2564, 1992.
Petroff, A. and Zhang, L.: Development and validation of a size-resolved particle dry deposition scheme for application in aerosol transport models, Geosci. Model Dev., 3, 753–769, doi:10.5194/gmd-3-753-2010, 2010.
Petroff, A., Zhang, L., Pryor, S. C., and Belot, Y.: An extended dry deposition model for aerosols onto broadleaf canopies, J. Aerosol Sci., 40, 218–240, 2009.
Petters, M. D. and Kreidenweis, S. M.: A single parameter representation of hygroscopic growth and cloud condensation nucleus activity, Atmos. Chem. Phys., 7, 1961–1971, doi:10.5194/acp-7-1961-2007, 2007.
Prime Minister of Japan and His Cabinet: Report of Japanese Government to the IAEA Ministerial Conference on Nuclear Safety – The Accident at TEPCO's Fukushima Nuclear Power Stations, available at: http://japan.kantei.go.jp/kan/topics/201106/iaea_houkokusho_e.html (last access: 25 April 2014), 2011.
RADNET: United States Environmental Protection Agency's Radiation monitoring Network (RADNET) Sampling Data for the Japanese Nuclear Emergency, available at: http://www.epa.gov/japan2011/rert/radnet-sampling-data.html (last access: 25 April 2014), 2011.
Reisner, J., Rasmussen, R. M., and Bruintjes, R. T.: Explicit forecasting of supercooled liquid water in winter storms using the MM5 mesoscale model, Q. J. Roy. Meteor. Soc., 124, 1071–1107, 1998.
Sanada, N. and Torii, T.: Aerial radiation monitoring around the Fukushima Dai-ichi Nuclear Power Plant using an unmanned helicopter, J. Environ. Radioactiv., in review, 2014.
Saunier, O., Mathieu, A., Didier, D., Tombette, M., Quélo, D., Winiarek, V., and Bocquet, M.: An inverse modeling method to assess the source term of the Fukushima Nuclear Power Plant accident using gamma dose rate observations, Atmos. Chem. Phys., 13, 11403–11421, doi:10.5194/acp-13-11403-2013, 2013.
Sauter, D. P. and Wang, P. K.: An experimental study of the scavenging of aerosol particles by natural snow crystals, J. Atmos. Sci., 46, 1650–1655, 1989.
Sehmel, G. A.: Particle and gas dry deposition: a review, Atmos. Environ., 14, 983–1011, 1980.
Smagorinsky, J.: General circulation experiments with the primitive equations, Mon. Weather Rev., 91, 99–164, 1963.
Sparmacher, H., Fulber, K., and Bonka, H.: Below-cloud scavenging of aerosol particles: particle-bound radionuclides – experimental, Atmos. Environ., 27, 605–618, 1993.

Srinivas, C. V., Venkatesan, R., Baskaran, R., Rajagopal, V., and Venkatraman, B.: Regional scale atmospheric dispersion simulation of accidental releases of radionuclides from Fukushima Dai-ichi reactor, Atmos. Environ., 61, 66–84, 2012.
Stier, P., Feichter, J., Kinne, S., Kloster, S., Vignati, E., Wilson, J., Ganzeveld, L., Tegen, I., Werner, M., Balkanski, Y., Schulz, M., Boucher, O., Minikin, A., and Petzold, A.: The aerosol-climate model ECHAM5-HAM, Atmos. Chem. Phys., 5, 1125–1156, doi:10.5194/acp-5-1125-2005, 2005.
Stohl, A., Seibert, P., Wotawa, G., Arnold, D., Burkhart, J. F., Eckhardt, S., Tapia, C., Vargas, A., and Yasunari, T. J.: Xenon-133 and caesium-137 releases into the atmosphere from the Fukushima Dai-ichi nuclear power plant: determination of the source term, atmospheric dispersion, and deposition, Atmos. Chem. Phys., 12, 2313–2343, doi:10.5194/acp-12-2313-2012, 2012.
Sugiyama, G., Nasstrom, J., Pobanz, B., Foster, K., Simpson, M., Vogt, P., Aluzzi, F., and Homann, S.: Atmospheric sispersion modeling: challenges of the Fukushima Daiichi response, Health Phys., 102, 493–508, 2012.
Sugiura, N., Awaji, T., Masuda, S., Mochizuki, T., Toyoda, T., Miyama, T., Igarashi, H., and Ishikawa, Y.: Development of a four-dimensional variational coupled data assimilation system for enhanced analysis and prediction of seasonal to interannual climate variations, J. Geophys. Res., 113, C10017, doi:10.1029/2008JC004741, 2008.
Takemura, T., Nakamura, H., Takigawa, M., Kondo, H., Satomura, T., Miyasaka, T., and Nakajima, T.: A numerical simulation of global transport of atmospheric particles emitted from the Fukushima Daiichi nuclear power plant, Sola, 7, 101–104, 2011.
Takeyasu, M. and Sumiya, S.: Estimation of dry deposition velocities of radionuclides released by the accident at the Fukushima Dai-ichi Nuclear Power Plant, Prog. Nucl. Sci. Technol., in press, 2014.
Tanabe, F.: A scenario of large amount of radioactive materials discharge to the air from the Unit 2 reactor in the Fukushima Daiichi NPP accident, J. Nucl. Sci. Technol., 49, 360–365, 2012.
Ten Hoeve, J. E. and Jacobson, M. Z.: Worldwide health effects of the Fukushima Daiichi nuclear accident, Energ. Environ. Sci., 5, 8743–8757, 2012.
TEPCO (Tokyo Electric Power Company): Press Releases, available at: http://www.tepco.co.jp/en/press/corp-com/release/index-e.html (last access: 25 April 2014), 2011a.

TEPCO: Radiation dose measured in the Fukushima Daini Nuclear Power Station 2011 Archives, available at: http://www.tepco.co.jp/en/nu/fukushima-np/f2/index-e.html (last access: 25 April 2014), 2011b.

TEPCO: Release of the Fukushima Nuclear Accidents Investigation Report, available at: http://www.tepco.co.jp/en/press/corp-com/release/2012/1205638_1870.html (last access: 25 April 2014), 2012.

Terada, H. and Chino, M.: Improvement of Worldwide Version of System for Prediction of Environmental Emergency Dose Information (WSPEEDI), (II) Evaluation of numerical models by ^{137}Cs deposition due to the Chernobyl nuclear accident, J. Nucl. Sci. Technol., 42, 651–660, 2005.

Terada, H. and Chino, M.: Development of an atmospheric dispersion model for accidental discharge of radionuclides with the function of simultaneous prediction for multiple domains and its evaluation by application to the Chernobyl nuclear accident, J. Nucl. Sci. Technol., 45, 920–931, 2008.

Terada, H., Furuno, A., and Chino, M.: Improvement of Worldwide Version of System for Prediction of Environmental Emergency Dose Information (WSPEEDI), (I) New combination of models, atmospheric dynamic model MM5 and particle random walk model GEARN-new, J. Nucl. Sci. Technol., 41, 632–640, 2004.

Terada, H., Katata, G., Chino, M., and Nagai, H.: Atmospheric discharge and dispersion of radionuclides during the Fukushima Dai-ichi Nuclear Power Plant accident, Part II: Verification of the source term and analysis of regional-scale atmospheric dispersion, J. Environ. Radioactiv., 112, 141–154, 2012.

Thalmann, E., Burkard, R., Wrzesinsky, T., Eugster, W., and Klemm, O.: Ion fluxes from fog and rain to an agricultural and a forest ecosystem in Europe, Atmos. Res., 64, 147–158, 2002.

Tochigi Prefecture: Results of Environmental Radioactivity (Air Dose Rate), available at: http://www.pref.tochigi.lg.jp/kinkyu/documents/20110312-18.pdf (last access: 25 April 2014), 2011 (in Japanese).

Tohoku Electric Power, available at: http://www.tohoku-epco.co.jp/news/atom/topics/1183332_1984.html (last access: 25 April 2014), 2011 (in Japanese).

Tokyo Metropolitan Government: Measurement of nuclear fission products of dust particles in the air in Tokyo, available at: http://www.sangyo-rodo.metro.tokyo.jp/whats-new/measurement-kako.html (last access: 25 April 2014), 2011 (in Japanese).

Torii, T., Sugita, T., Okada, C. E., Reed, M. S., and Blumenthal, D. J.: Enhanced analysis methods to derive the spatial distribution of I-131 deposition on the ground by airborne surveys at an early stage after the Fukushima Daiichi nuclear power plant accident, Health Phys., 105, 192–200, 2013.

Tost, H., Jöckel, P., Kerkweg, A., Sander, R., and Lelieveld, J.: Technical note: A new comprehensive SCAVenging submodel for global atmospheric chemistry modelling, Atmos. Chem. Phys., 6, 565–574, doi:10.5194/acp-6-565-2006, 2006.

Uematsu, M., Merrill, J. T., Patterson, T. L., Duce, R. A., and Prospero, J. M.: Aerosol residence times and iodine gas/particle conversion over the North Pacific as determined from Chernobyl radioactivity, Geochem. J., 22, 157–163, 1988.

UNSCEAR (United Nations Scientific Committee on the Effects of Atomic Radiation): UNSCEAR 2013 Report: Sources, Effects and Risks of Ionizing Radiation, vol. I, available at: http://www.unscear.org/docs/reports/2013/13-85418_Report_2013_Annex_A.pdf (last access: 25 April 2014), 2014.

US DOE (Department of Energy): Response to 2011 Fukushima Incident – Data and Documentation, available at: http://energy.gov/downloads/us-doennsa-response-2011-fukushima-incident-data-and-documentation (last access: 25 April 2014), 2011.

US DOE/NNSA (National Nuclear Security Administration): Response to 2011 Fukushima incident – raw aerial data and extracted ground exposure rates and cesium deposition, available at: https://explore.data.gov (last access: 25 April 2014), 2011.

US NDC (United States National Data Center): United States National Data Center, International Monitoring System Data for the CTBTO network, available at: http://www.usandc.gov/radionuclide.html (last access: 25 April 2014), 2011.

US NRC (Nuclear Regulatory Commission): RASCAL 4: Description of Models and Methods, NUREG-1940, Richland, WA, 2012.

Wang, X., Zhang, L., and Moran, M. D.: Uncertainty assessment of current size-resolved parameterizations for below-cloud particle scavenging by rain, Atmos. Chem. Phys., 10, 5685–5705, doi:10.5194/acp-10-5685-2010, 2010.

Wesely, M. L.: Parameterization of surface resistances to gaseous dry deposition in regional-scale numerical models, Atmos. Environ., 23, 1293–1304, 1989.

Wesely, M. L. and Hicks, B. B.: Some factors that affect the deposition rates of sulfur dioxide and similar gases on vegetation, J. Air Pollut. Control Assoc., 27, 1110–1116, 1977.

Winiarek, V., Bocquet, M., Duhanyan, N., Roustan, Y., Saunier, O., and Mathieu, A.: Estimation of the caesium-137 source term from the Fukushima Daiichi nuclear power plant using a consistent joint assimilation of air concentration and deposition observations, Atmos. Environ., 82, 268–279, 2014.

WMO (World Meteorological Organization): Evaluation of Meteorological Analyses for the Radionuclide Dispersion and Deposition from the Fukushima Daiichi Nuclear Power Plant Accident, 1120, 64 pp., available at: https://www.wmo.int/e-catalog/detail_en.php?PUB_ID=669&SORT=N&q= (last access: 25 April 2014), 2014.

Wolf, M. A. and Dana, M. T.: Experimental studies on precipitation scavenging, USAEC Report BNWL-105, Battelle Pacific Northwest Laboratory, Richland, Wash., 18–25, 1969.

Yasunari, T. J., Stohl, A., Hayano, R. S., Burkhart, J. F., Eckhardt, S., and Yasunari, T.: Cesium-137 deposition and contamination of Japanese soils due to the Fukushima nuclear accident, Proc. Natl. Acad. Sci. USA, 108, 19530–19580, 2011.

Zhang, L., Gong, S., Padro, J., and Barrie, L.: A size-segregated particle dry deposition scheme for an atmospheric aerosol module, Atmos. Environ., 35, 549–560, 2001.

Zhang, L., Brook, J. R., and Vet, R.: A revised parameterization for gaseous dry deposition in air-quality models, Atmos. Chem. Phys., 3, 2067–2082, doi:10.5194/acp-3-2067-2003, 2003.

Zhang, L., Wang, X., Moran, M. D., and Feng, J.: Review and uncertainty assessment of size-resolved scavenging coefficient formulations for below-cloud snow scavenging of atmospheric aerosols, Atmos. Chem. Phys., 13, 10005–10025, doi:10.5194/acp-13-10005-2013, 2013.

Table 1. The simulation settings of deposition scheme in atmospheric dispersion models applied to the FNPS1 accident; CCN: cloud condensation nuclei, d_m: geometric mass particle diameter, d_n: geometric number particle diameter, U: wind speed, RH: relative humidity, P_r: precipitation, CLW: cloud liquid water content, T: air temperature, H: (effective) Henry's constant, z: height, dz_c: cloud height, dz_p: depth of the pollutant layer. The reverse and inverse estimation methods are defined in UNSCEAR (2014). Note that only the studies to estimate the source term through March 2011 using environmental monitoring data are shown in the table.

Model name	Dispersion	Radionuclides	Chemical form	Particle size distribution	Dry deposition	Wet deposition	Fog deposition	Snow scavenging	CCN activation	Source term estimation	Model application papers to the FNPS1 accident
GEARN	Lagrangian	^{131}I, ^{132}Te (^{132}I), ^{134,137}Cs	Bulk	No	Constant	P_r	No	No	No	Reverse and Inverse methods	Chino et al. (2011), Katata et al. (2012a, b), Terada et al. (2012), Kobayashi et al. (2013)
CMAQ	Eulerian	^{131}I, ^{137}Cs	Gas/submicron particle	Log-normal (Kaneyasu et al., 2012)	Resistance (Zhang et al., 2001)	P_r, CLW, H, dz_c	No	No	Complete activation	No	Morino et al. (2011, 2013)
SPRINTERS	Eulerian	Not specified	Coarse particle	Log-normal (d_m = 10 µm)	Constant	CLW, P_r	No	No	30–60 % activation	No	Takemura et al. (2011)
FLEXPART	Lagrangian	^{133}Xe, ^{137}Cs	Gas/submicron particle	Log-normal (d_m = 0.4 µm)	Resistance (Wesely and Hicks, 1977)	RH, P_r, H, z (Hertel et al., 1995)	No	No	Complete activation	Inverse method	Yasunari et al. (2011), Stohl et al. (2012), Srinvas et al. (2012), Sugiyama et al. (2012), Draxler et al. (2014), Achim et al. (2014)
HYSPLIT	Lagrangian	^{131}I, ^{137}Cs	Gas/particle	No	Constant	RH, P_r, H, dz_p	No	No	No	No[a]	Draxler and Rolph (2012), Srinvas et al. (2012), Draxler et al. (2014)
RASCAL v3	Gauss plume	^{131}I, ^{137}Cs	I_2 or HI, CH_3I, CsI	1 µm	Constant	P_r	No	Yes	No	No	Dvorzhak et al. (2012)
ldX, Polair3D//pX	Eulerian/puff	73 species	Bulk	No	Constant	P_r	No	No	No	Inverse method	Mathieu et al. (2012), Korsakissok et al. (2013), Saunier et al. (2013), Winiarek et al. (2012, 2014)

Table 1. Continued.

LODI	Lagrangian	^{131}I, ^{132}Te (^{132}I), ^{134,137}Cs	Gas/particle	Log-normal	Resistance	P_r	No	No	No	No	Sugiyama et al. (2012)
GATOR-GCMOM	Lagrangian	^{131}I, ^{137}Cs	Gas/particle	Log-normal (d_n = 0.06 µm)	Resistance (Wesely, 1989)	Jacobson (2005)	No	No	Jacobson (2005)	Inverse estimation	Ten Hoeve and Jacobson (2012)
EMAC	Lagrangian	^{131}I, ^{137}Cs	Gas/particle	Log-normal	Resistance (Kerkweg et al., 2006)	P_r, CLW, dz_c, U (Tost et al., 2006)	No	No	No	No	Christoudias and Lelieveld (2013)
LPRM	Lagrangian	^{131}I, ^{137}Cs	Bulk	No	Constant	P_r	No	No	No	Inverse estimation	Hirao et al. (2013)
MLDP0	Lagrangian	^{131}I, ^{137}Cs	Gas/particle	No	Constant	Cloud fraction	No	No	No	No	Draxler et al. (2014)
RATM	Lagrangian	^{131}I, ^{137}Cs	Gas/particle	No	Constant	RH, P_r, H, $z < 1500$ m (Hertel et al., 1995)	No	No	90 % activation	No	Draxler et al. (2014)
NAME	Lagrangian	^{131}I, ^{137}Cs	Gas/particle	No	Resistance	P_r, CLW, dz_c	No	Yes	No	No	Leadbetter et al. (2014), Draxler et al. (2014)
Modified GEARN	Lagrangian	^{131}I, ^{132}Te (^{132}I), ^{134,137}Cs	I_2, CH_3I, CsI	Log-normal (Miyamoto et al., 2014)	Resistance (Kajino et al., 2012)	P_r, CLW, H, dz_c (Giorgi and Chameides, 1986)	CLW, U (Katata, 2014)	Yes	Abdul-Razzak and Ghan (2000)	Reverse and inverse methods	This study

[a] These models are available for inverse estimation for source attribution, while this option was not exercised for FNPS1 accident.

Table 2. Characteristics and total inventories of radionuclides for Unit 1-3 at FNPS1 (Nishihara et al., 2012).

Radionuclide	State in atmosphere	Half-life	Boiling point (°C)	Total inventory (PBq)
I-131	Gas/aerosol	8.0 day	180	6.02E+6
I-132	Gas/aerosol	2.3 h	180	8.85E+6
Te-132	Gas/aerosol	3.2 day	1400	8.68E+6
I-133	Gas/aerosol	21.0 h	180	1.26E+7
Cs-137	Aerosol	30.0 year	670	6.98E+5
Cs-134	Aerosol	2.1 year	670	7.18E+5

Table 3. Dust sampling data used for the source term estimation. The locations of monitoring data are illustrated in Fig. 3. The concentration calculations for source term estimation were carried out under the assumption of a unit release rate (1 Bq h^{-1}).

Location code in Fig. 3	Nos. in Table 5	Sampling location	Sampling date and time (JST)	Total ^{131}I Concentration (Bq m^{-3})		^{137}Cs Concentration (Bq m^{-3})	
				Observed	Calculated	Observed	Calculated
a	20L	JAEA-Tokai	15 Mar 01:25–15 Mar 01:45	234	9.4×10^{-13}	15	1.0×10^{-12}
	22L	(Ohkura et al.,	15 Mar 4:25–15 Mar 04:45	1257	–	161	–
	24L–26L	2012)	15 Mar 6:55–15 Mar 08:15	2430–2800	–	282–366	–
	55L		20 Mar 11:35–20 Mar 11:55	140	1.1×10^{-12}	26	1.2×10^{-12}
	56L		21 Mar 03:45–21 Mar 07:05	1092	8.6×10^{-12}	243	1.1×10^{-11}
b	55L	MEXT21	20 Mar 14:13–20 Mar 14:33	4800	1.0×10^{-11}	1000	1.1×10^{-11}
c	55L	MEXT31	20 Mar 14:15–20 Mar 14:35	1000	5.2×10^{-12}	180	5.5×10^{-12}
d	55L	MEXT41	20 Mar 11:37–20 Mar 11:49	970	6.3×10^{-12}	–	–
e	57L, 59L	MEXT44	21 Mar 10:05–21 Mar 11:08	1420	6.2×10^{-11}	–	–
f	58L	MEXT71	21 Mar 13:00–21 Mar 13:04	5600	1.3×10^{-10}	36	1.3×10^{-10}
	60L		22 Mar 14:55–22 Mar 16:30	570–1100	3.4×10^{-12}–1.2×10^{-11}	7.7–11	3.5×10^{-12}–1.2×10^{-11}
	61L		23 Mar 13:15–23 Mar 15:59	110–530	1.6×10^{-12}–1.1×10^{-11}	2.1–6.6	1.6×10^{-12}–1.1×10^{-11}
	62L		24 Mar 10:06–24 Mar 12:26	5.9–12	4.0×10^{-13}	0–1.1	4.1×10^{-13}
	63L		25 Mar 11:51–25 Mar 16:42	10–43	5.4×10^{-13}	1.3–2.5	5.7×10^{-13}
	68O		31 Mar 12:22–31 Mar 15:44	13–24	9.9×10^{-12}	0.96–4.5	1.0×10^{-11}
g	55L	MEXT46	20 Mar 14:45–20 Mar 14:55	4100	1.1×10^{-11}	–	–
	63L		25 Mar 15:02–25 Mar 15:22	555	4.6×10^{-12}	12.4	4.7×10^{-12}
	67L		30 Mar 14:11–30 Mar 14:32	89	1.0×10^{-12}	91	1.0×10^{-12}
h	60L	DOE	22 Mar 06:00–22 Mar 07:00	357–2961	3.8×10^{-12}–1.0×10^{-11}	2–19	3.6×10^{-12}–1.0×10^{-11}
i	62L	MEXT80	24 Mar 14:55–24 Mar 15:15	193	7.2×10^{-12}	2.94	7.4×10^{-12}
	65O		29 Mar 11:17–29 Mar 15:00	29–75	1.1×10^{-11}	23–46	1.1×10^{-11}
j	64O	MEXTsea8	27 Mar 11:45–	20	1.5×10^{-12}	0.88	1.5×10^{-12}
k	66L	FNPS2	30 Mar 09:27–30 Mar 09:35	1490	1.6×10^{-10}	820	1.6×10^{-10}
l	67L	MEXT61	30 Mar 14:15–30 Mar 14:35	28	1.0×10^{-12}	20	1.0×10^{-12}
	69O		1 Apr 12:00–1 Apr 12:20	1.78	1.0×10^{-11}	1.69	1.1×10^{-11}

Table 4. The settings for the WSPEEDI-II atmospheric dispersion model used in the coupling of the atmospheric and oceanic dispersion simulations.

	reverse estimation over the land			inverse estimation over the ocean
	Domain 1	Domain 2	Domain 3	Domain 1
Study areas	East Japan			North Pacific
Applied GEARN calculations	No	Yes	Yes	Yes
Simulation period for GEARN	5:00 on 12 March–0:00 on 17 Mar 2011			5:00 on 12 March–9:00 on 31 May 2011
Horizontal grid cell	100 × 100	190 × 130	190 × 190	250 × 150
Spatial resolutions	9 km	3 km	1 km	80 km
Boundary and initial conditions of MM5	Grid Point Value (Global Spectral Model for Japan region, GSM, and Meso-Scale Model, MSM) by Japan Meteorological Agency (JMA)			GSM for the global region by JMA
3-D/surface analysis nudging	Utilized with wind data at FNPP1 (surface), FNPP2 (120 m) (METI, 2011b), and surface weather stations			Utilized for 3-D
Observation nudging	Utilized with wind data at FNPP1 (surface) and FNPP2 (120 m)			No
Release rates and heights	See Table 5			
Other parameters	Same as Katata et al. (2012a, b) and Kobayashi et al. (2013) except for microphysics parameterization of Reisner graupel scheme			

Table 5. Release period, release duration, release rate of total ^{131}I, radioactivity ratio of ^{137}Cs/total ^{131}I, the ratio of gaseous ^{131}I to total ^{131}I, and release height for the period between 5:00 on 12 March to 0:00 on 1 May 2011. Notations of "L" and "O" in the first column represent estimations using land and ocean environmental monitoring data, respectively. In the last column, MP: monitoring post, C: concentration, and AMS: Aerial Measuring System of US Department of Energy/National Nuclear Security Administration (US DOE/NNSA, 2011).

No.	Release period (Japan Standard Time)	Release duration (h)	Release rate of total ^{131}I (Bq h^{-1})	^{137}Cs/ total ^{131}I	Gaseous ^{131}I/ total ^{131}I	Release height/ volume (m)	Monitoring data
1O	12 Mar 05:00–12 Mar 09:30	4.5	4.9×10^{13}	0.100	0.500	20	Sea water C
2O	12 Mar 09:30–12 Mar 14:00	4.5	2.3×10^{13}	0.100	0.500	20	Sea water C
3L	12 Mar 14:00–12 Mar 15:00	1.0	2.3×10^{15}	0.100	0.500	120	Kamihatori MP
4O	12 Mar 15:00–12 Mar 15:30	0.5	6.3×10^{13}	0.100	0.500	20	Sea water C
5L	12 Mar 15:30–12 Mar 16:00	0.5	1.1×10^{16}	0.100	0.500	100 × 100 × 100[a]	Shinzan MP
6O	12 Mar 16:00–12 Mar 22:00	6.0	4.7×10^{14}	0.100	0.500	120	Sea water C
7O	12 Mar 22:00–13 Mar 04:00	6.0	4.2×10^{14}	0.100	0.500	120	Sea water C
8O	13 Mar 04:00–13 Mar 09:00	5.0	1.7×10^{14}	0.100	0.500	120	Sea water C
9O	13 Mar 09:00–13 Mar 12:30	3.5	1.9×10^{14}	0.100	0.500	120	Sea water C
10O	13 Mar 12:30–13 Mar 15:00	2.5	4.1×10^{14}	0.100	0.500	120	Sea water C
11O	12 Mar 15:00–13 Mar 23:00	8.0	3.1×1^{14}	0.100	0.500	120	Sea water C
12O	13 Mar 23:00–14 Mar 02:30	3.5	5.8×10^{13}	0.100	0.500	120	Sea water C
13O	14 Mar 02:30–14 Mar 07:00	4.5	1.8×10^{13}	0.100	0.500	120	Sea water C
14O	14 Mar 07:00–14 Mar 11:00	4.0	3.2×10^{13}	0.100	0.500	120	Sea water C
15O	14 Mar 11:00–14 Mar 11:30	0.5	3.2×10^{15}	0.100	0.500	300 × 100 × 100[a]	Sea water C
16O	14 Mar 11:30–14 Mar 18:00	6.5	9.2×10^{13}	0.100	0.500	20	Sea water C
17O	14 Mar 18:00–14 Mar 19:00	1.0	3.3×10^{13}	0.100	0.500	20	Sea water C
18O	14 Mar 19:00–14 Mar 20:00	1.0	1.2×10^{13}	0.100	0.500	20	Sea water C
19O	14 Mar 20:00–14 Mar 21:00	1.0	1.1×10^{13}	0.100	0.500	20	Sea water C
20L	14 Mar 21:00–14 Mar 22:00	1.0	2.3×10^{14}	0.068	0.500	20	JAEA-Tokai C
21O	14 Mar 22:00–14 Mar 23:00	1.0	1.3×10^{13}	0.100	0.500	20	Sea water C
22L	14 Mar 23:00–15 Mar 00:00	1.0	5.8×10^{14}	0.120	0.500	20	JAEA-Tokai C & FNPS2 MP
23O	15 Mar 00:00–15 Mar 01:00	1.0	1.7×10^{13}	0.100	0.500	20	Sea water C
24L	15 Mar 01:00–15 Mar 02:00	1.0	1.5×10^{15}	0.151	0.500	20	JAEA-Tokai C & FNPS2 MP
25L	15 Mar 02:00–15 Mar 03:00	1.0	2.9×10^{14}	0.127	0.500	20	JAEA-Tokai C & FNPS2 MP
26L	15 Mar 03:00–15 Mar 04:00	1.0	2.8×10^{14}	0.117	0.500	20	JAEA-Tokai C & FNPS2 MP
27L	15 Mar 04:00–15 Mar 05:00	1.0	4.6×10^{14}	0.100	0.500	20	Nasu MP
28L	15 Mar 05:00–15 Mar 06:00	1.0	4.6×10^{14}	0.100	0.500	20	Nasu MP
29L	15 Mar 06:00–15 Mar 07:00	1.0	4.6×10^{14}	0.100	0.500	20	Nasu MP
30L	15 Mar 07:00–15 Mar 10:00	3.0	1.2×1^{15}	0.100	0.500	20	Koriyama & Iitate MPs
31L	15 Mar 10:00–15 Mar 11:00	1.0	8.9×10^{14}	0.100	0.500	20	Kawauchi & Ohno MPs
32L	15 Mar 11:00–15 Mar 16:00	5.0	1.0×10^{14}	0.100	0.500	20	AMS air dose rate
33L	15 Mar 16:00–15 Mar 18:00	2.0	1.9×10^{14}	0.100	0.500	20–120[b]	Iitate MP
34L	15 Mar 18:00–15 Mar 19:00	1.0	1.7×10^{15}	0.100	0.500	20–120[b]	Kawafusa[c] & AMS air dose rate
35L	15 Mar 19:00–15 Mar 20:00	1.0	8.6×10^{14}	0.100	0.500	20–120[b]	Kawafusa[c] & AMS air dose rate
36L	15 Mar 20:00–15 Mar 22:00	2.0	1.0×10^{16}	0.014	0.700	20–120[b]	Yamada MP
37L	15 Mar 22:00–15 Mar 23:00	1.0	7.8×10^{15}	0.014	0.700	20–120[b]	Ohno MP & AMS air dose rate
38L	15 Mar 23:00–16 Mar 01:00	2.0	1.5×10^{15}	0.014	0.700	20–120[b]	Futatsunuma & Yamadaoka MPs
39O	16 Mar 01:00–16 Mar 06:00	5.0	1.0×10^{14}	0.014	0.700	20–120[b]	Sea water C
40O	16 Mar 06:00–16 Mar 09:00	3.0	1.0×10^{14}	0.100	0.500	20	Sea water C
41L	16 Mar 09:00–16 Mar 11:00	2.0	2.1×10^{15}	0.100	0.500	20	FNPS2, Futatsunuma & Yamadaoka MPs

Table 5. Continued.

No.	Release period (Japan Standard Time)	Release duration (h)	Release rate of total ^{131}I (Bq h^{-1})	^{137}Cs/ total ^{131}I	Gaseous ^{131}I/ total ^{131}I	Release height/ volume (m)	Monitoring data
42O	16 Mar 11:00–16 Mar 12:00	1.0	7.3×10^{13}	0.100	0.500	20	Sea water C
43O	16 Mar 12:00–16 Mar 13:00	1.0	1.3×10^{14}	0.100	0.500	20	Sea water C
44O	16 Mar 13:00–16 Mar 14:00	1.0	6.1×10^{14}	0.100	0.500	20	Sea water C
45O	16 Mar 14:00–16 Mar 15:00	1.0	1.4×10^{15}	0.100	0.500	20	Sea water C
46O	16 Mar 15:00–17 Mar 06:00	15.0	9.1×10^{14}	0.100	0.500	20	Sea water C
47O	17 Mar 06:00–17 Mar 21:00	15.0	3.1×10^{14}	0.100	0.500	20	Sea water C
48O	17 Mar 21:00–18 Mar 00:00	3.0	1.9×10^{14}	0.100	0.500	20	Sea water C
49O	18 Mar 00:00–18 Mar 05:00	5.0	1.4×10^{14}	0.100	0.500	20	Sea water C
50O	18 Mar 05:00–18 Mar 08:00	3.0	8.5×10^{14}	0.100	0.500	20	Sea water C
51O	18 Mar 08:00–18 Mar 13:00	5.0	6.8×10^{14}	0.100	0.500	20	Sea water C
52O	18 Mar 13:00–18 Mar 18:00	5.0	7.5×10^{14}	0.100	0.500	20	Sea water C
53O	18 Mar 18:00–19 Mar 05:00	11.0	5.5×10^{14}	0.100	0.500	20	Sea water C
54O	19 Mar 05:00–19 Mar 15:00	10.0	1.1×10^{15}	0.100	0.500	20	Sea water C
55L	19 Mar 15:00–21 Mar 03:00	36.0	2.2×10^{14}	0.190	0.500	20	MEXT21, 31, 41, 46 & JAEA-Tokai C
56L	21 Mar 03:00–21 Mar 08:00	5.0	1.6×10^{14}	0.218	0.486	20	JAEA-Tokai C
57L	21 Mar 08:00–21 Mar 12:00	4.0	4.1×10^{13}	0.113[d]	0.658	20	MEXT44 C
58L	21 Mar 12:00–21 Mar 16:00	4.0	5.9×10^{13}	0.007	0.594	20	MEXT71 C
59L	21 Mar 16:00–21 Mar 21:00	5.0	4.1×10^{13}	0.113[d]	0.658	20	Assumed same as 57L
60L	21 Mar 21:00–22 Mar 23:00	26.0	1.5×10^{14}	0.08	0.671	20	DOE & MEXT 71 C
61L	22 Mar 23:00–24 Mar 00:00	25.0	2.6×10^{14}	0.013	0.495	20	MEXT71 C
62L	24 Mar 00:00–25 Mar 00:00	24.0	1.8×10^{13}	0.035	0.605	20	MEXT71 & 80 C
63L	25 Mar 00:00–26 Mar 11:00	35.0	4.1×10^{13}	0.056	0.681	20	MEXT46 & 71 C
64O	26 Mar 11:00–28 Mar 10:00	47.0	2.1×10^{13}	0.042	0.901	20	Sea water & MEXTsea8 C
65O	28 Mar 10:00–29 Mar 21:00	35.0	5.0×10^{12}	0.781	0.927	20	Sea water & MEXT80 C
66L	29 Mar 21:00–30 Mar 11:00	14.0	9.0×10^{12}	0.621	0.544	20	FNPS2 C
67L	30 Mar 11:00–31 Mar 00:00	13.0	5.9×10^{13}	0.833	0.688	20	MEXT46 & 61 C
68O	31 Mar 00:00–31 Mar 22:00	22.0	1.5×10^{13}	0.186	0.707	20	Sea water & MEXT71 C
69O	31 Mar 22:00–2 Apr 09:00	35.0	9.4×10^{11}	0.973	0.934	20	Sea water & MEXT61 C
70L	2 Apr 09:00–4 Apr 09:00	48.0	1.0×10^{13}	0.323	0.894	20	Chino et al. (2011)
71L	4 Apr 09:00–7 Apr 17:00	80.0	3.9×10^{12}	0.204	0.894	20	Chino et al. (2011)
72L	7 Apr 17:00–13 Apr 23:00	150.0	7.0×10^{11}	0.500	0.948	20	Terada et al. (2012)
73L	13 Apr 23:00–1 May 00:00	409.0	7.0×10^{11}	0.257	0.948	20	Terada et al. (2012)

[a] Volume sources were assumed to hydrogen explosion at Units 1 and 3 (Katata et al., 2012b).
[b] The situations of both leakage from the Primary Containment Vessel (PCV) and venting at the top of stack with 20 and 120 m height were assumed.
[c] Up to 330 μGy h^{-1} was observed at the northwest of FNPS1 around 21:00 on 15 Mar (Fig. S3).
[d] Interporated from the ratios of 56L and 58L due to lack of the data of ^{137}Cs.

Table 6. Statistics of the surface depositions of total ^{131}I and ^{137}Cs, and sea surface concentration of ^{134}Cs between observations and calculations of Terada et al. (2012) and using modified WSPEEDI-II with the new source term estimated from land data only (referred as "New-land") and both land and sea data (referred as "New-landsea"). The values of FA2, 5, and 10 denote the percentage of calculations within factors of 2, 5, and 10 of the measurements, respectively. Regional- and local-scale data were compared with calculations of WSPEEDI-II over domain 2 and 3, respectively.

Source term & model	Radionuclide	FA2 (%)	FA5 (%)	FA10 (%)	Correlation coefficient
Regional-scale surface deposition over East Japan at 0:00 on 1 Apr 2011					
Terada et al. (2012)	^{137}Cs	41.6	78.8	92.1	0.64
New-land	^{137}Cs	46.4	80.6	92.1	0.70
Local-scale surface deposition near FNPS1 at 0:00 on 1 Apr 2011					
New-land	total ^{131}I	45.2	84.1	94.9	0.65
	^{137}Cs	42.7	78.5	90.9	0.58
Local-scale air dose rate in the north-west area of FNPS1 at 0:00 on 18 Mar 2011					
Katata et al. (2012b)	Total	44.	87.2	98.3	0.63
New-land	Total	42.4	83.1	95.3	0.56
Local-scale air dose rate in the south-west area of FNPS1 at 0:00 on 18 Mar 2011					
Katata et al. (2012b)	Total	30.8	72.3	90.8	0.45
New-land	Total	56.8	95.1	99.6	0.79
Sea surface concentration from 2 April–17 May 2011					
New-land	^{134}Cs	32.6	54.3	71.7	0.65
New-landsea	^{134}Cs	21.7	60.9	82.6	0.69

Table 7. Statistics of the air concentrations and surface depositions of gaseous and particulate ^{131}I and ^{137}Cs between observations and calculations using three WMO models with Terada at al. (2012) and the new source terms (referred as "Terada" and "New", respectively). Five statistical parameters were selected to represent different evaluation metrics: the correlation coefficient (CC), the fractional bias (FB), the figure-of-merit in space (FMS), the Kolmogorov–Smirnov parameter (KSP), and the normalized mean square error (NMSE). Also a ranking method (Draxler, 2006) was defined by giving equal weight to the normalized (0–1) sum of the CC, FB, FMS, and KSP, such that the total model rank (RANK) would range from 0 to 4 (from worst to best).

Source term & model & meteorological data	CC	NMSE	FB	FMS	KSP	Rank
Particulate ^{131}I concentration at JAEA-Tokai from 15–31 Mar						
Terada-MLDP0-MESO	0.35	11.19	0.12	82.5	24.0	2.64
New-MLDP0-MESO	0.40	12.65	0.01	82.5	27.0	2.71
Terada-HYSPLIT-MESO	0.09	38.41	−1.04	77.5	46.0	1.80
New-HYSPLIT-MESO	0.24	68.35	−1.42	77.5	51.0	1.61
Terada-NAME-MESO	0.30	16.04	−0.29	82.5	41.0	2.36
New-NAME-MESO	0.54	20.08	−0.79	82.5	52.0	2.20
Gaseous ^{131}I concentration at JAEA-Tokai from 15–31 Mar						
Terada-MLDP0-MESO	0.41	18.01	−0.89	82.5	44.0	2.11
New-MLDP0-MESO	0.70	24.82	−1.19	82.5	42.0	2.30
Terada-HYSPLIT-MESO	0.16	39.19	−1.30	77.5	54.0	1.61
New-HYSPLIT-MESO	0.27	64.88	−1.55	77.5	61.0	1.47
Terada-NAME-MESO	0.29	14.13	−0.52	82.5	54.0	2.11
New-NAME-MESO	0.51	19.60	−1.00	82.5	58.0	2.01
^{137}Cs concentration at JAEA-Tokai from 15–31 Mar						
Terada-MLDP0-MESO	0.26	15.24	−0.09	82.5	34.0	2.51
New-MLDP0-MESO	0.32	13.79	0.00	82.5	29.0	2.64
Terada-HYSPLIT-MESO	0.14	54.54	−1.22	77.5	53.0	1.66
New-HYSPLIT-MESO	0.21	67.34	−1.36	77.5	56.0	1.58
Terada-NAME-MESO	0.29	21.33	−0.50	82.5	53.0	2.13
New-NAME-MESO	0.44	19.56	−0.60	82.5	54.0	2.18
Regional-scale ^{137}Cs surface deposition over East Japan at 0:00 on 1 Apr 2011						
Terada-MLDP0-MESO	0.77	10.85	−0.30	100.0	25.0	3.19
New-MLDP0-MESO	0.81	17.10	−0.68	100.0	29.0	3.03
Terada-HYSPLIT-MESO	0.67	7.32	0.21	100.0	36.0	2.98
New-HYSPLIT-MESO	0.62	14.63	−0.21	99.93	45.0	2.83
Terada-NAME-MESO	0.78	4.99	0.14	100.0	19.0	3.35
New-NAME-MESO	0.74	9.79	−0.34	100.0	21.0	3.17
New-NAME-MESO-RAP	0.78	9.00	−0.34	100.0	32.0	3.12
New-NAME-ECMWF	0.84	5.04	−0.12	100.0	14.0	3.50

Table 8. Statistics (similar to Table 7) of the air concentrations and surface depositions of gaseous and particulate ^{131}I and ^{137}Cs between observations and calculations using HYSPLIT with Terada at al. (2012) and the new source terms (referred as "Terada" and "New", respectively). Although it depends upon the site, the sampling data used for the analysis are generally available from 15 March through 4 April for the EPA sites and through 20 Apr for the CTBTO and European sites. The EPA sites contain both gaseous and particulate measurements, while the CTBTO sites only particulate concentrations are provided.

Source term & model & meteorological data	CC	NMSE	FB	FMS	KSP	Rank
Particulate ^{131}I concentration						
Terada-HYSPLIT-GFS	0.48	8.79	−0.49	99.58	27.0	2.71
New-HYSPLIT-GFS	0.46	11.52	−0.19	99.58	29.0	2.82
Gaseous ^{131}I concentration						
Terada-HYSPLIT-GFS	0.63	3.65	−0.11	99.69	17.0	3.17
New-HYSPLIT-GFS	0.69	5.02	0.11	99.69	14.0	3.28
^{137}Cs concentration						
Terada-HYSPLIT-GFS	0.32	12.76	0.41	100.	16.0	2.74
New-HYSPLIT-GFS	0.31	32.35	0.95	100.0	28.0	2.34

Table 9. Total release amount of total ^{131}I and ^{137}Cs to the atmosphere from 12 March–1 May 2011 using source terms estimated from land data only (referred as "New-land") and from both land and sea data in this study (referred as "New-landsea") and those of past studies. Note that the values of Winiarek et al. (2014) and Stohl et al. (2012) are derived from hourly estimation results using the daily fallout, airborne survey data, and aggregated for all release layers from 0–1000 m, respectively. It is also noted that the release rates of Saunier et al. (2013), when the plume directly flowed to the Pacific Ocean, could not be reconstructed correctly.

Name of source term	Integration period	Total ^{131}I (PBq)	^{137}Cs (PBq)
New-land	12 March–1 May 2011	117.6	9.3
New-landsea	12 March–1 May 2011	142.9	12.4
Terada et al. (2012)	12 March–1 May 2011	123.9	8.8
Kobayashi et al. (2013)	12 March–1 May 2011	200.0	13.
Saunier et al. (2013)	12 March–27 Mar 2011	105.9	15.5
Winiarek et al. (2014)	11 March–1 Apr 2011	–	19.3
Stohl et al. (2012)	10 March–20 Apr 2011	–	35.9

Table 10. The calculated percentages of each deposition process to the total amount of ^{137}Cs released from 5:00 on 11 March to 0:00 on 1 April 2011 over the land (forest and other landuse categories) and sea in East Japan region (Domain 2; Fig. 4c).

	Deposition (%)					Outflow from
	Forest	Other land	All land	Sea	Land + Sea	the domain (%)
Wet deposition	15.7	4.7	2.4	5.5	25.9	–
Dry deposition	3.3	1.6	4.9	0.5	5.4	–
Fog deposition	1.0	0.8	1.8	0.3	2.1	–
Total deposition	2.0	7.5	27.1	6.3	33.4	66.6

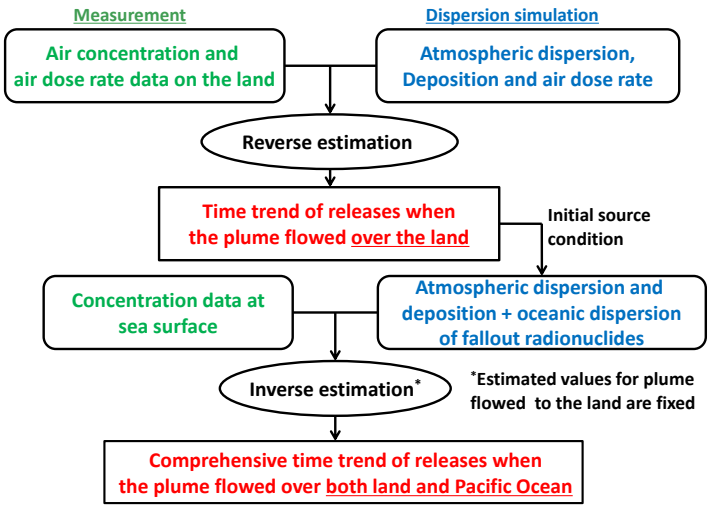

Figure 1. The flowchart of the source term estimation technique based on coupling the atmospheric and oceanic dispersion model simulations. The reverse and inverse estimations methods are described in Sects. 2.2 and 2.3, respectively.

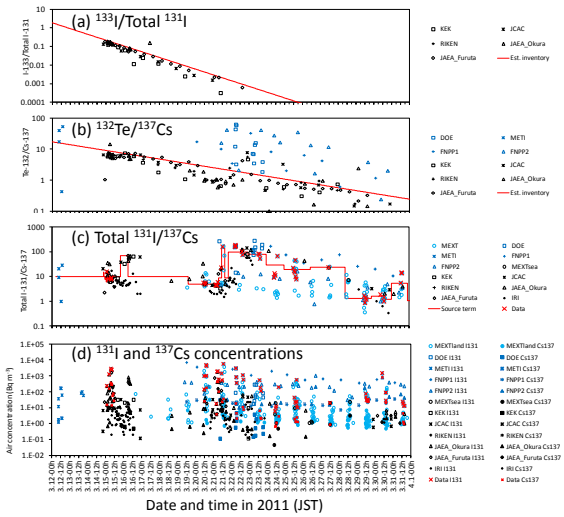

Figure 2. The time series in **(a)** the ratios of ^{133}I to total ^{131}I, and **(b)** ^{132}Te to ^{137}Cs and **(c)** total ^{131}I to ^{137}Cs in atmosphere, and **(d)** air concentrations of total ^{131}I and ^{137}Cs for the data sampled near each station (blue symbols: METI, FNPS1, FNPS2, MEXT, MEXTsea, and DOE) and at offsite monitoring sites in Eastern Japan (black symbols: JAEA-Tokai, KEK, RIKEN, JCAC, and Tokyo Metropolitan Government (Tokyo)) from 12–31 March 2011. The red solid lines in **(a)** and **(b)** are the curves derived from Eq. (2) with the value of ^{132}Te/^{137}Cs = 20 (for ^{132}Te) at the shutdown time. The red solid line in **(c)** represents the ratio of total ^{131}I to ^{137}Cs for the source term estimated in this study, which is assumed or determined from the data shown as the red symbols in **(c)** and **(d)**.

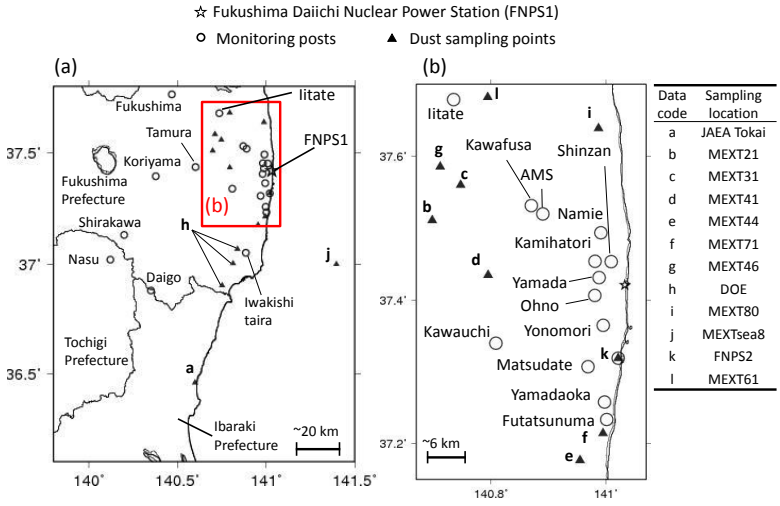

Data code	Sampling location
a	JAEA Tokai
b	MEXT21
c	MEXT31
d	MEXT41
e	MEXT44
f	MEXT71
g	MEXT46
h	DOE
i	MEXT80
j	MEXTsea8
k	FNPS2
l	MEXT61

Figure 3. The sampling locations of the environmental monitoring data used for source term estimation using the reverse estimation method over land.

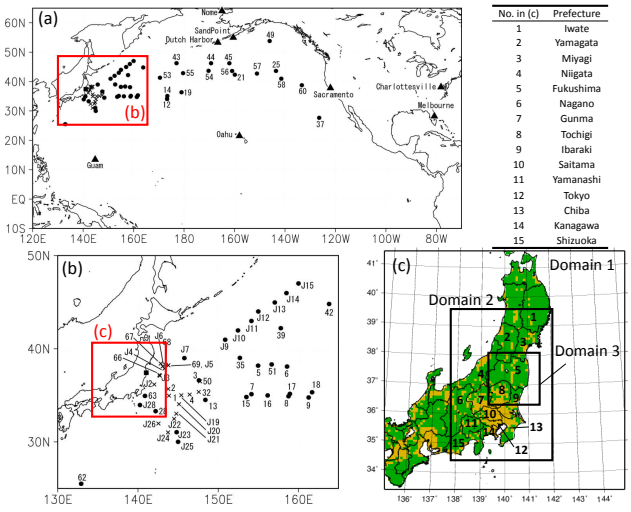

Figure 4. The simulation domains for **(a)** and **(b)** the oceanic dispersion and **(c)** the atmospheric dispersion simulations. The sampling locations of the sea surface concentration data for the source term estimation using the inverse estimation method are plotted in **(a)** and **(b)** (black circles), while the sampling points affected by the direct release of radionuclides from the FNPS1 to the ocean were not considered in the inverse estimation (crosses), as indicated by Kobayashi et al. (2013). The prefectures (number) and forest cover (green shaded areas) over East Japan were also shown in **(c)**.

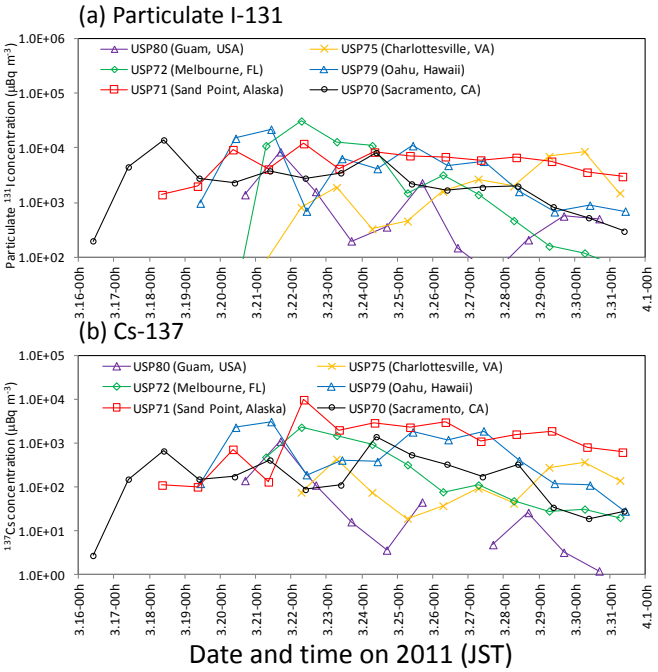

Figure 5. Temporal changes in the observed daily mean surface concentrations of **(a)** particulate ^{131}I and **(b)** ^{137}Cs at several stations of the United States, Alaska, and Hawaii from 16 March to 1 April 2011.

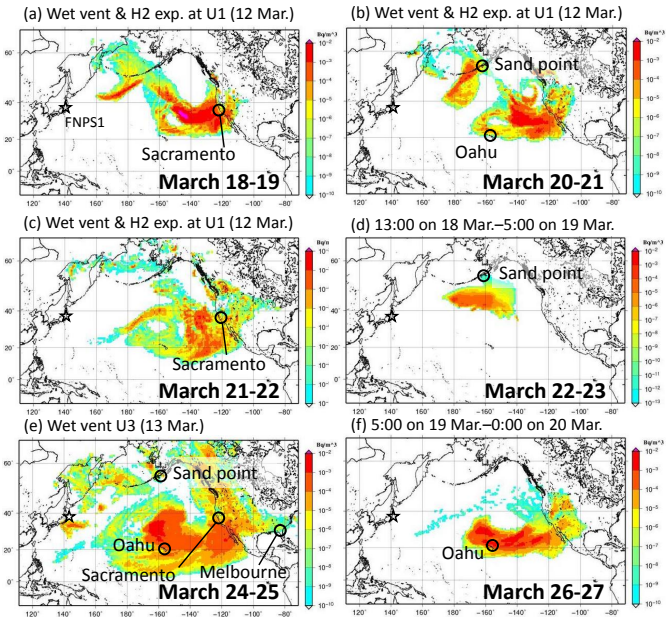

Figure 6. Daily mean surface concentrations of ^{137}Cs calculated by WSPEEDI-II using the new source term **(a)** on 18–19 March, **(b)** 20–21 March, **(c)** 21–22 March, **(d)** 22–23 March, **(e)** 24–25 March, and **(f)** 26–27 March 2011. The recognized events in the reactors (Fig. 7) when the plume was discharged are shown in captions for each panel.

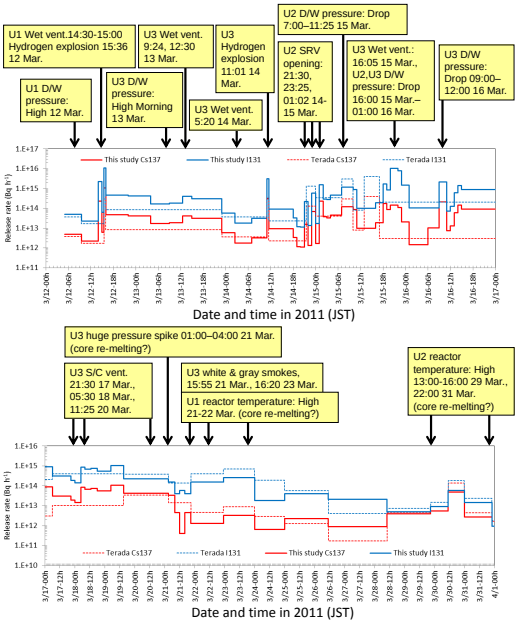

Figure 7. Temporal changes in release rate of total ^{131}I and ^{137}Cs from 12 March to 1 April 2011 reconstructed in this study (solid lines) and Terada et al. (2012) (dashed lines). The recognized events in the reactors (Prime Minister of Japan and his cabinet, 2011; TEPCO, 2011a, 2012) are shown above the figure.

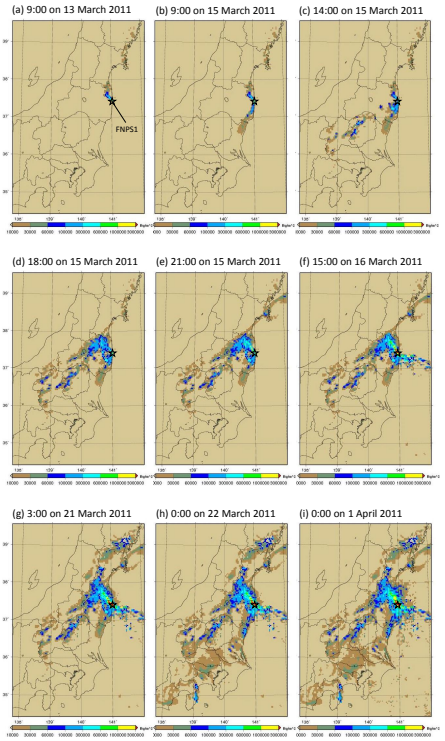

Figure 8. Spatial distributions of surface deposition of ^{137}Cs over East Japan calculated by WSPEEDI-II using the new source term **(a)** at 09:00 on 13 March, **(b)** 9:00, **(c)** 14:00, **(d)** 18:00, and **(e)** 21:00 on 15 March, **(f)** 15:00 on 16 March, **(g)** 3:00 on 21 March, **(h)** 00:00 on 22 March, and **(i)** 0:00 on 1 April 2011.

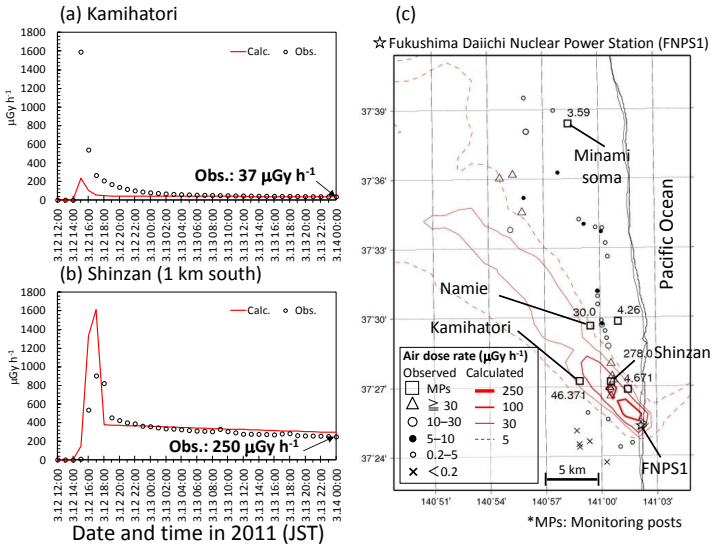

Figure 9. The time series of calculated (solid lines) and observed air dose rates (dashed lines with open circles) at the automated monitoring posts **(a)** Kamihatori and **(b)** Shinzan (1 km south of the actual monitoring post of Shinzan), and **(c)** comparison of the calculated air dose rates at 12:00 on 13 March 2011 in the north-northwest area of the FNPS1 vs. measurements from 6:00 to 15:00. In **(b)**, the calculated air dose rate at 1 km south of Shinzan was compared with the observed one because the principal axis of the calculated plume seemed to be several kilometers further west from that of the observed axis.

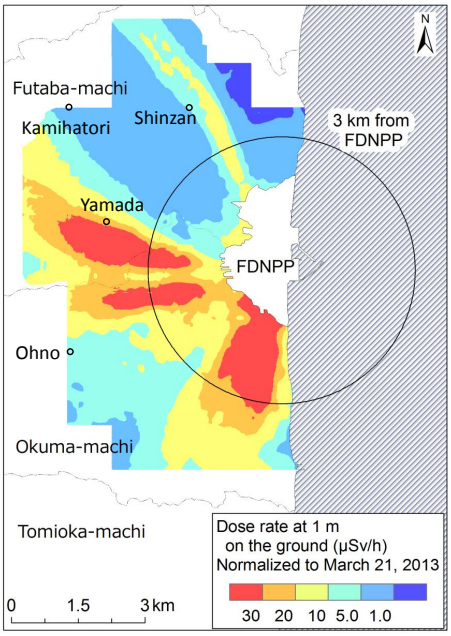

Figure 10. Spatial distributions of air dose rate within the 5 km area around FNPS1 observed by airborne survey from 28 January to 20 March 2013 (Sanada and Torii, 2014).

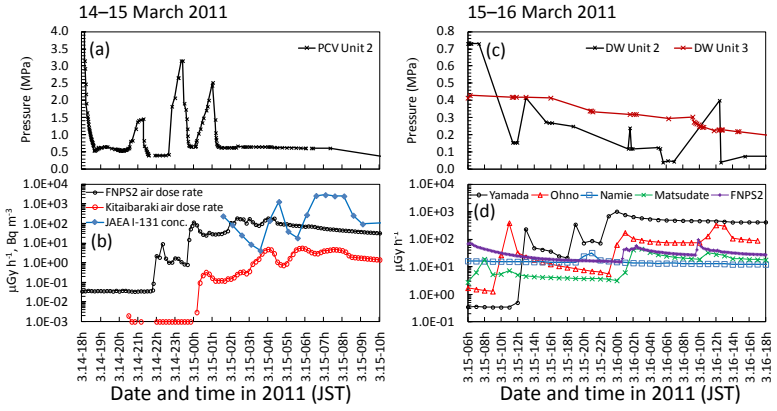

Figure 11. Temporal changes in measurements of **(a)** and **(c)** the pressures of the reactor pressure vessel (RPV) and drywell (DW) at Units 2 and 3 of FNPS1, and **(b)** and **(d)** the air dose rates and total ^{131}I concentration at several monitoring posts and JAEA-Tokai, respectively, **(a, b)** from 14–15 March and **(c, d)** from 15–16 March 2011. The location of monitoring posts is depicted in Fig. 3.

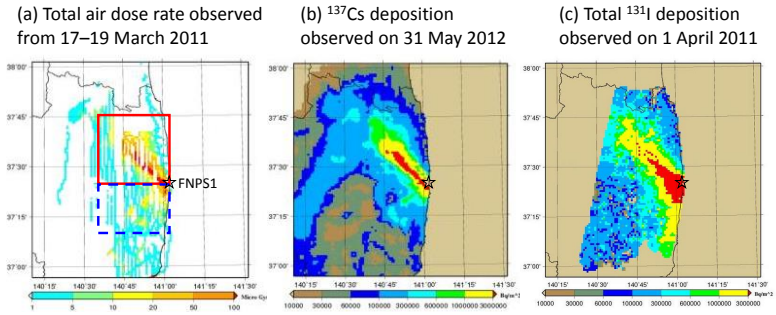

Figure 12. Aerial monitoring maps of **(a)** observed air dose rates (US DOE, 2011) from 17–19 March, **(b)** ^{137}Cs deposition (NRA, 2012), and **(c)** total ^{131}I deposition around FNPS1 (Torii et al., 2013). The squares surrounded by solid and dashed lines represent the northwest and southeast areas compared with calculation results in Fig. 16, respectively.

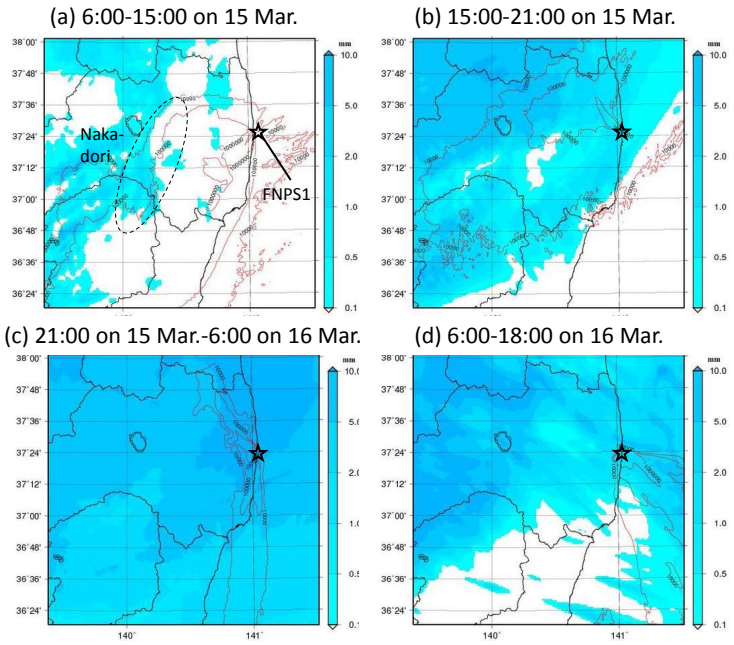

Figure 13. Spatial distributions of the vertical cumulative air concentration of ^{137}Cs (Bq m^{-3}, contour lines) and precipitation amount (mm, shaded areas) accumulated from **(a)** 06:00–15:00 on 15 March, **(b)** 15:00–21:00 on 15 March, **(c)** 21:00 on 15 March–06:00 on 16 March, and **(d)** 06:00–18:00 on 16 March calculated by WSPEEDI-II using the new source term.

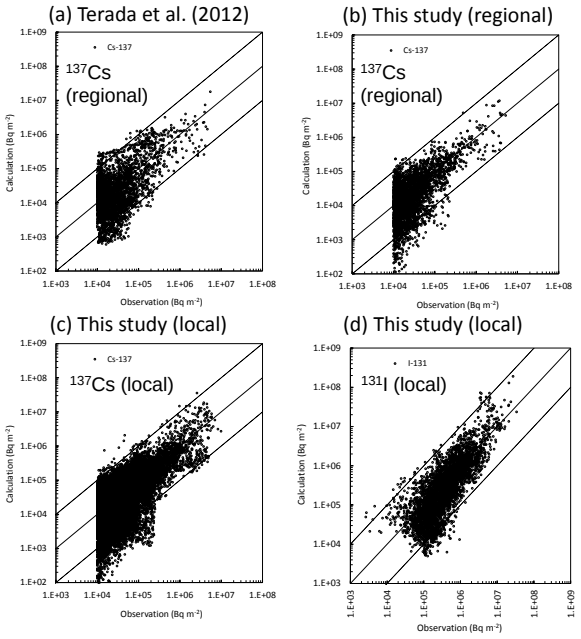

Figure 14. Scatter diagrams of the surface deposition of **(a–c)** ^{137}Cs and **(d)** total ^{131}I (Bq m^{-2}) on 1 April 2011 comparing measurements and calculations of **(a)** Terada et al. (2012) and [**(b)**–**(d)**] using modified WSPEEDI-II with the new source term for **(a, b)** Domain 2 and **(c, d)** Domain 3. The black solid lines show the 1 : 1 correspondence, and the areas between two black dashed lines indicate the bands within a factor of 10.

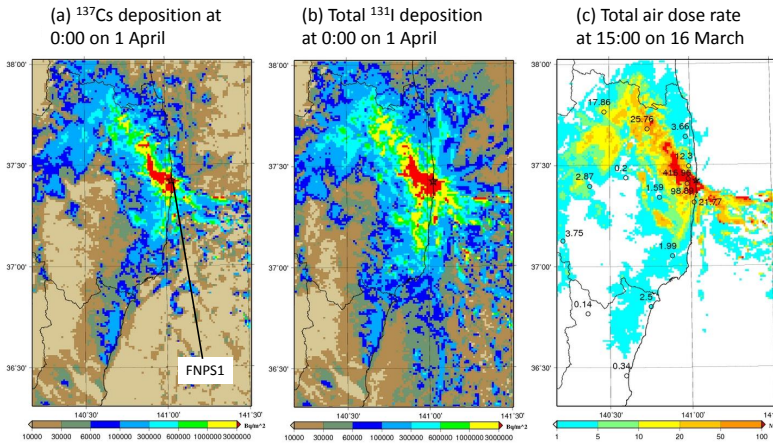

Figure 15. The local-scale spatial distributions of surface depositions of **(a)** ^{137}Cs and **(b)** total ^{131}I, and **(c)** air dose rate at 00:00 on 1 April and 15:00 on 16 March 2011, respectively, simulated by WSPEEDI-II using the new source term. Values and colors of circles in **(c)** represent observed air dose rates at monitoring posts. The minimum significant digit is 0.01, which was determined from the observational data of air dose rates.

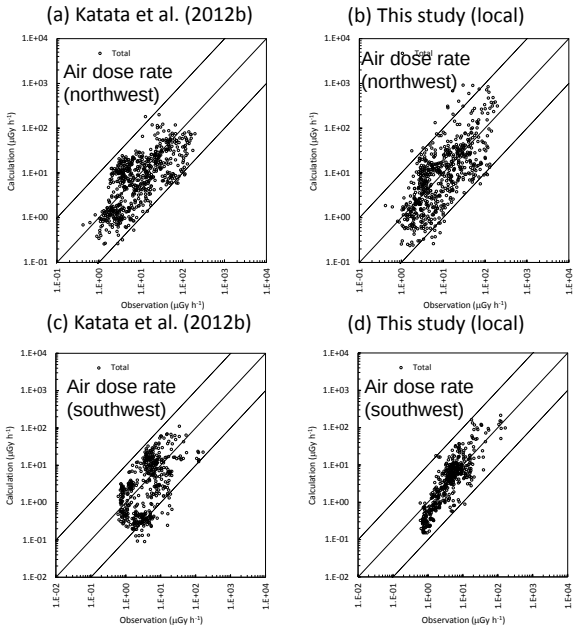

Figure 16. Scatter diagrams of the total air dose rate (μGy h^{-1}) comparing the measurements and calculations of **(a, c)** Katata et al. (2012b) and **(b, d)** using the modified WSPEEDI-II with the new source term for **(a, b)** the northwest and **(c, d)** southwest regions in Domain 3 on 18 March 2011. The black solid lines show 1 : 1 correspondence, and the areas between two black dashed lines indicate the bands within a factor of 10. The northwest and southwest regions are depicted in Fig. 12a.

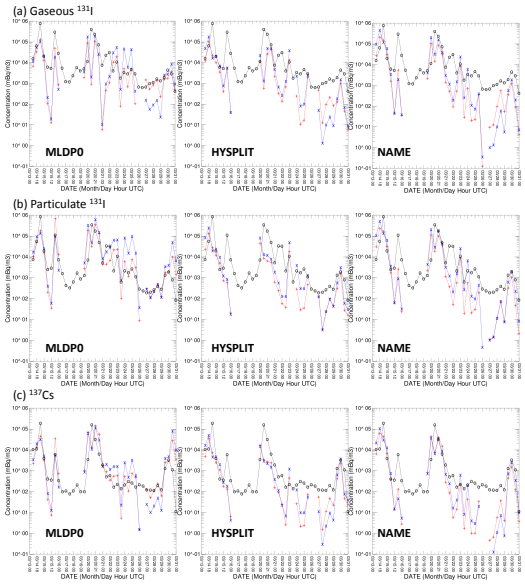

Figure 17. Temporal changes in observed (lines with open circles) and modeled air concentrations (mBq m^{-3}) using three WMO models (MLDP0, HYSPLIT, and NAME) with the source terms of this study (lines with pluses) and Terada et al. (2012) (lines with crosses) for **(a)** gaseous and **(b)** particulate ^{131}I, and **(c)** ^{137}Cs at JAEA-Tokai in Ibaraki Prefecture from 13–31 March 2011.

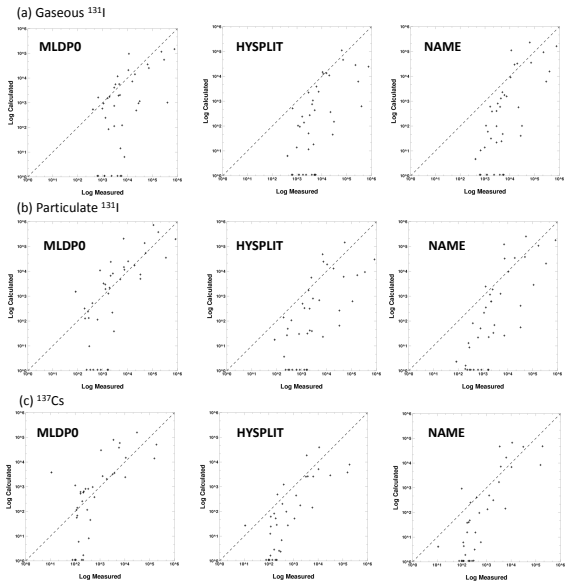

Figure 18. Scatter diagrams of air concentrations (mBq m^{-3}) comparing measurements and calculations using three WMO models (MLDP0, HYSPLIT, and NAME) with the new source term for **(a)** gaseous and **(b)** particulate ^{131}I, and **(c)** ^{137}Cs at JAEA-Tokai in Ibaraki Prefecture from 13–31 March 2011. The black dashed lines show the 1 : 1 correspondence.

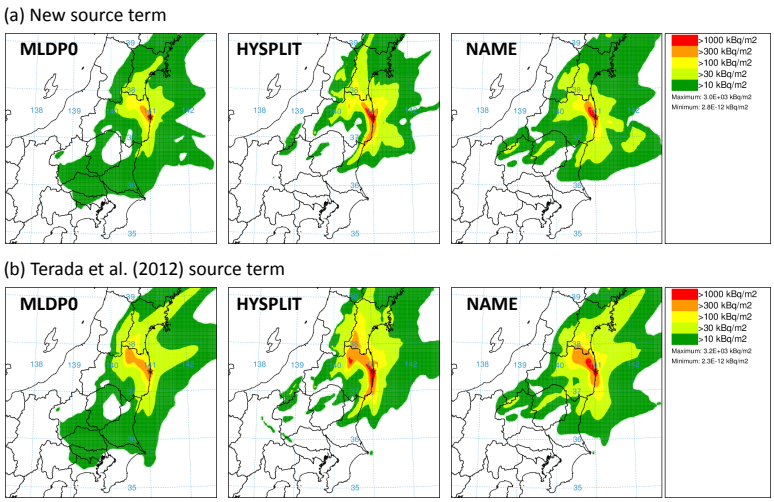

Figure 19. Spatial distributions of surface depositions of ^{137}Cs (kBq m^{-2}) on 1 April 2011 calculated by three WMO models (MLDP0, HYSPLIT, and NAME) using **(a)** the new source term and **(b)** Terada et al. (2012).

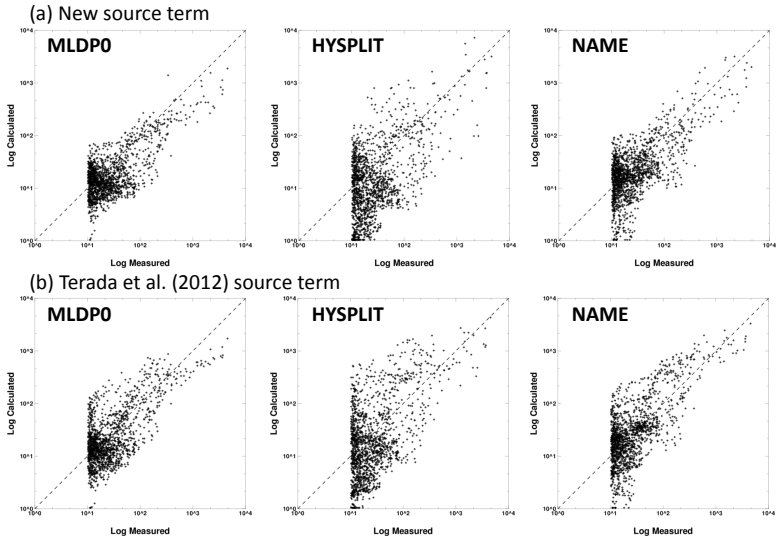

Figure 20. Scatter diagrams of surface deposition (kBq m^{-2}) comparing measurements and calculations using three WMO models (MLDP0, HYSPLIT, and NAME) with the source term of **(a)** this study and **(b)** Terada et al. (2012) on 1 April 2011. The black dashed lines show the 1 : 1 correspondence.

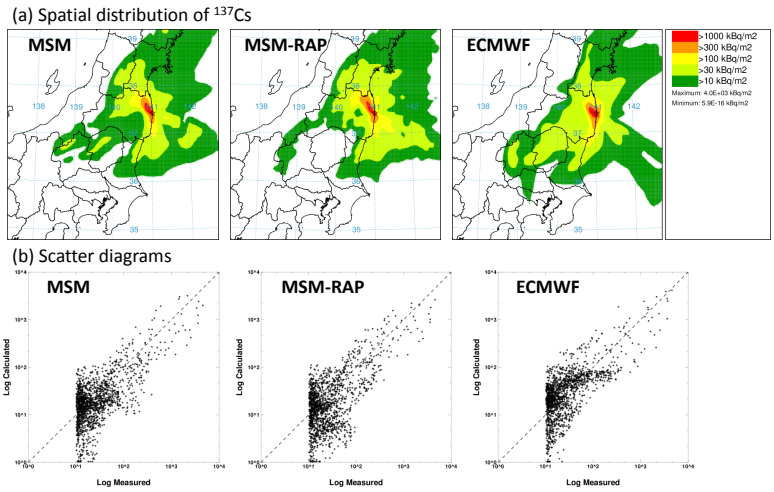

Figure 21. (a) Spatial distributions and **(b)** scatter diagrams of surface depositions of ^{137}Cs (kBq m^{-2}) on 1 April 2011 comparing measurements and calculations of NAME using the new source term using the three meteorological fields (MSM, MSM-RAP, and ECMWF).

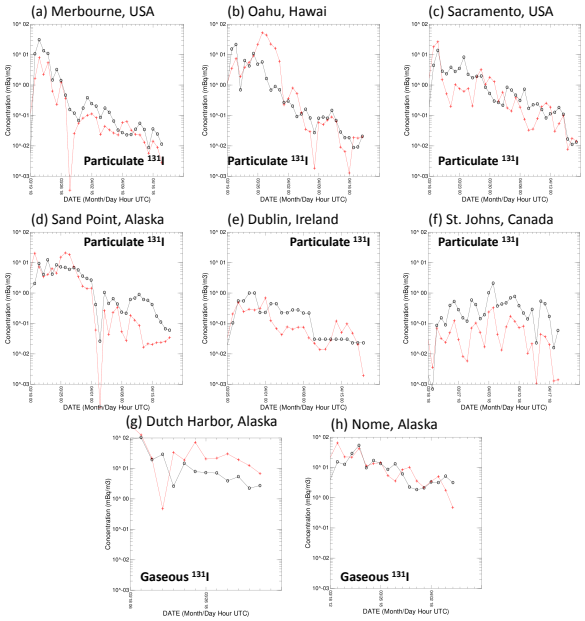

Figure 22. Temporal changes in observed (lines with open circles) and modeled (lines with crosses) air concentrations (mBq m^{-3}) using HYSPLIT with the new source term for air concentration of **(a–f)** particulate and **(g, h)** gaseous ^{131}I at selected CTBTO, US EPA, and European stations from 13–31 March 2011.

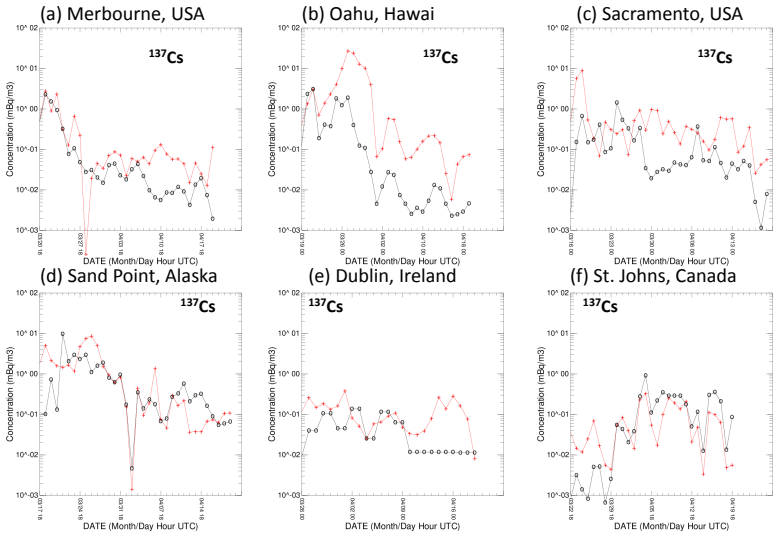

Figure 23. Temporal changes in observed (lines with open circles) and modeled (lines with crosses) air concentrations (mBq m^{-3}) using HYSPLIT with the new source term for air concentration of ^{137}Cs at selected CTBTO, US EPA, and European stations from 13–31 March 2011.

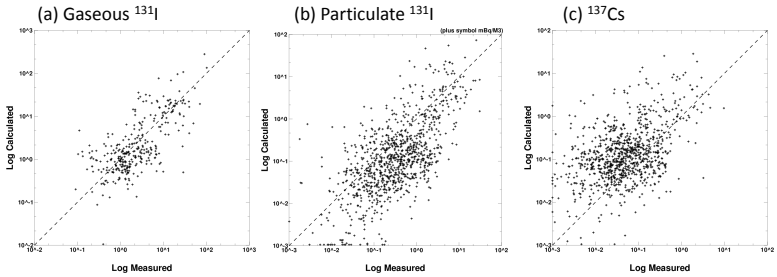

Figure 24. Scatter diagrams of air concentrations (mBq m^{-3}) comparing measurements and calculations using HYSPLIT with the new source term for **(a)** gaseous and **(b)** particulate ^{131}I, and **(c)** ^{137}Cs in the CTBTO, US-EPA, and European monitoring stations for the period of 15 March through 20 April. The black dashed lines show the 1 : 1 correspondence.

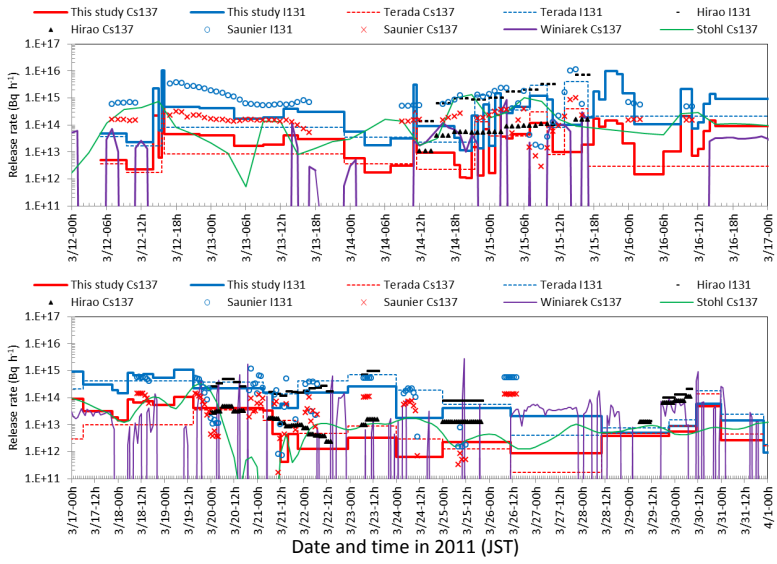

Figure 25. Comparisons of the time varying release rates for total ^{131}I and ^{137}Cs from 12 March to 1 April 2011 between this study and past studies (Terada et al., 2012; Stohl et al., 2012; Hirao et al., 2013; Saunier et al., 2013; Winiarek et al., 2014). Note that the values of Winiarek et al. (2014) and Stohl et al. (2012) are derived from hourly estimation results using the daily fallout, airborne survey data, and aggregated for all release layers from 0–1000 m, respectively. It is also noted that the release rates of Saunier et al. (2013), when the plume directly flowed to the Pacific Ocean, could not be reconstructed correctly.

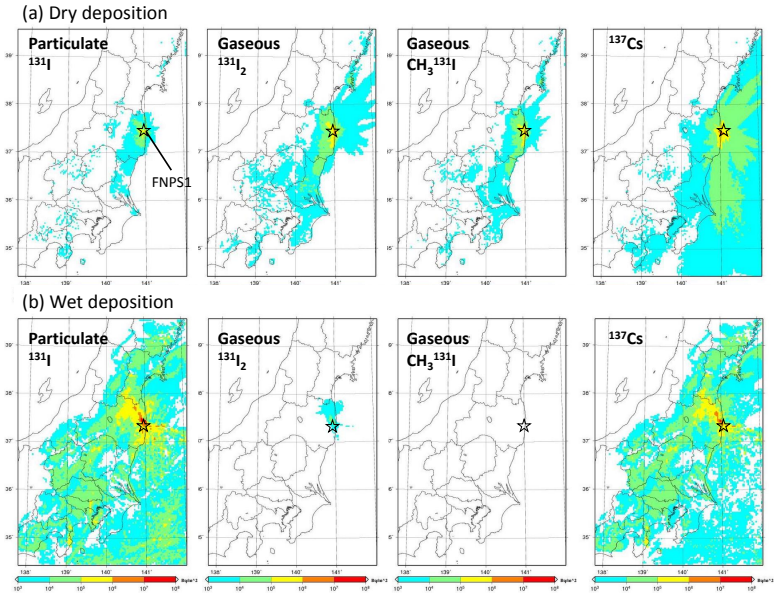

Figure 26. (a) Spatial distributions of the cumulative dry deposition and **(b)** wet deposition of each radionuclide (particulate and gaseous ^{131}I and ^{137}Cs) (Bq m^{-2}) at 00:00 on 1 April 2011 in the WSPEEDI simulation.

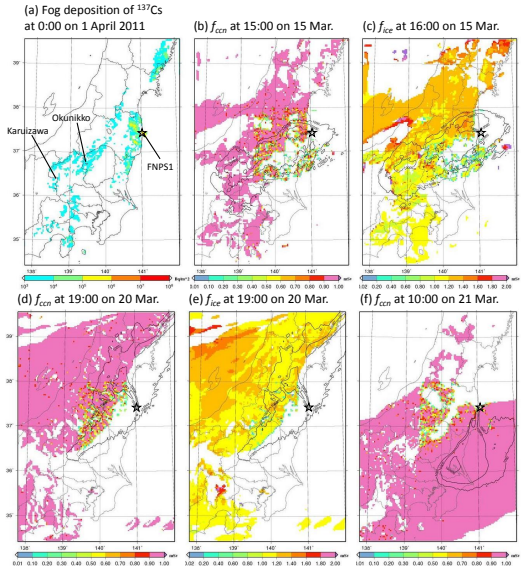

Figure 27. (a) Spatial distributions of cumulative fog deposition of ^{137}Cs (Bq m^{-2}) at 0:00 on 1 April 2011, and **(b, d, f)** the fraction of the CCN activated aerosols in cloud (f_{ccn}) **(b)** at 15:00 on 15 March, **(d)** 19:00 on 20 March, and **(f)** 10:00 on 21 March, and **(c, e)** the accretion efficiency of cloud droplets by settling ice crystals (i.e., snow and graupel) (f_{ice}) **(c)** at 16:00 on 15 March and **(e)** 19:00 on 20 March in the WSPEEDI simulation. f_{ccn} and f_{ccn} represent vertical mean values for the atmospheric layers where the calculated ^{137}Cs concentration was greater than zero. The contour lines in **(b–f)** represent vertical accumulated concentration of ^{137}Cs.

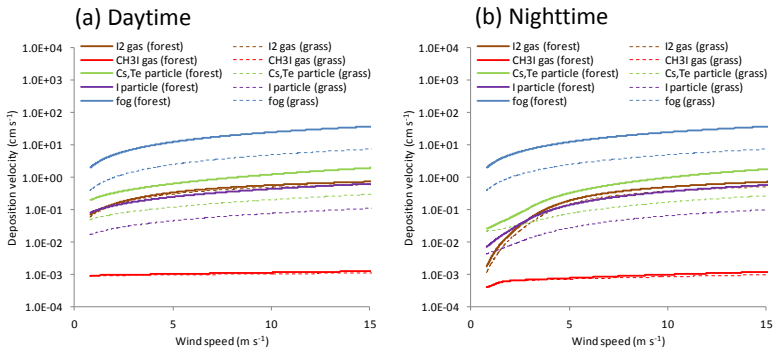

Figure A1. Changes in the modeled deposition velocity (V_d) of gaseous and particulate radioactive substances and of fogwater vs. the horizontal wind speed over forest (solid lines) and grassland (dashed lines) surfaces **(a)** during the daytime and **(b)** nighttime for typical clear condition. Input meteorological data are mainly from the surface weather stations in Fukushima Prefecture from 12–15 March 2011 and show the following: 16 and −1.5 °C for air temperature, 21 and −5 °C for ground surface temperature, 800 and 0 W m^{-1} for solar radiation, 30 and 70 % for relative humidity during the daytime and nighttime, respectively.

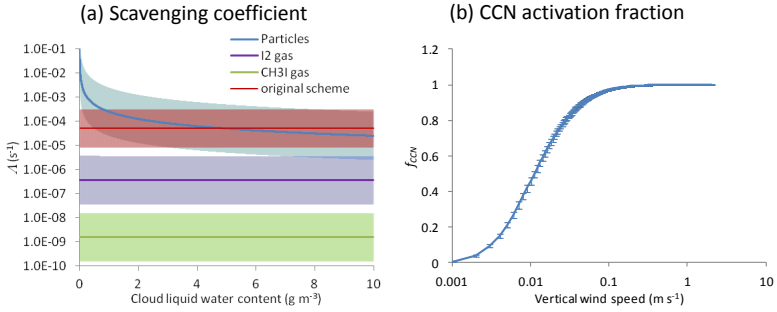

Figure A2. (a) Changes in the modeled scavenging coefficient (Λ) of gaseous and particulate radioactive substances vs. the vertical mean cloud liquid water content ($\overline{W}_{q_c}$), and in **(b)** the CCN activation fraction (f_{ccn}) vs. the vertical wind speed. Input meteorological data are mainly from the surface weather stations in Ibaraki and Fukushima Prefectures from 12–15 March 2011 and show the following: 15 °C for air temperature, 1 km for cloud thickness, 1 mm h^{-1} for precipitation rate with f_{ccn}, f_{ice}, and f_{q_c} = 1 in **(a)**, and 5 °C for air temperature and 950 hPa for air pressure in **(b)**. The shaded areas in **(a)** represent the range of Λ when precipitation rate changes from 0.1–10 mm h^{-1}. The vertical bars in **(b)** show the deviation in f_{ccn} when air temperature and pressure were changed from 0–15 °C and 900–1000 hPa, respectively.